



Università  
degli Studi  
di Catania

Dottorato di Ricerca in Scienza dei Materiali e Nanotecnologie  
XXXV ciclo

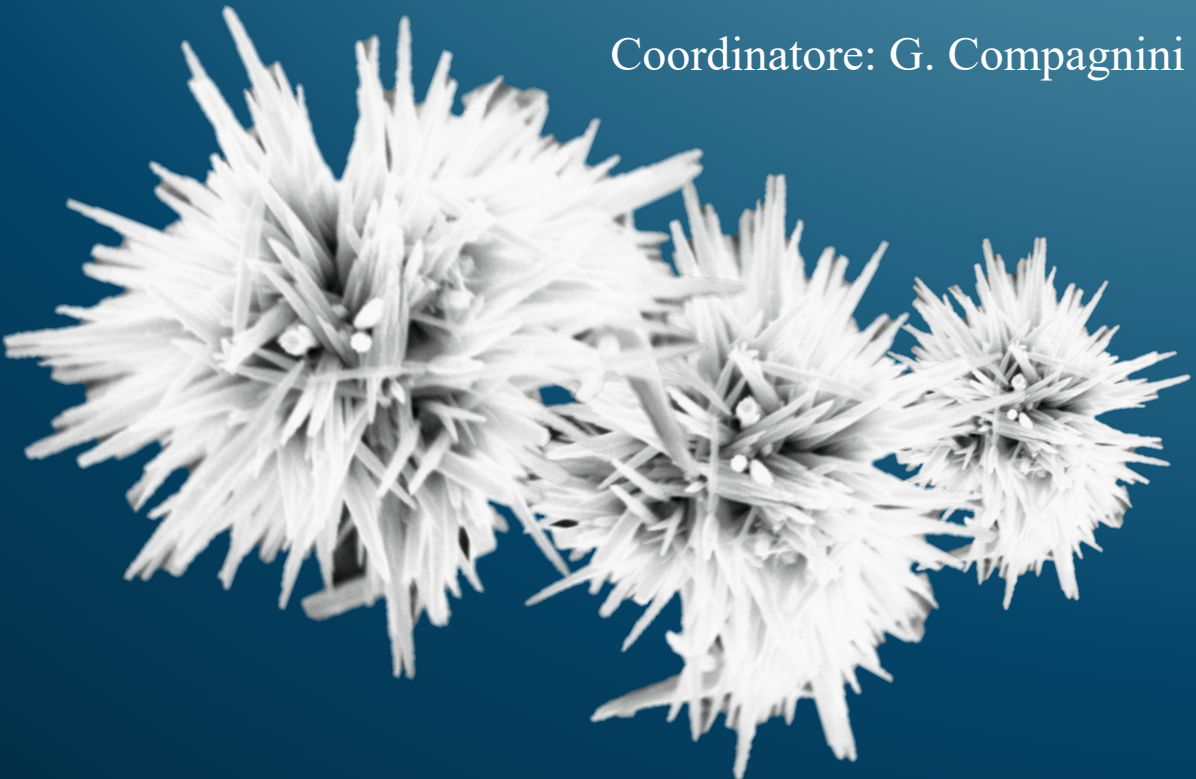
Giacometta Mineo

# Optimized hydrothermal synthesis of $\text{WO}_3$ nanorods for energy and environment

Tutor: Prof.ssa E. Bruno

Tutor: Prof. S. Mirabella

Coordinatore: G. Compagnini







UNIVERSITÀ DEGLI STUDI DI CATANIA

---

DOTTORATO DI RICERCA IN  
SCIENZA DEI MATERIALI E NANOTECNOLOGIE - XXXV CICLO

---

Giacometta Mineo

**Optimized hydrothermal synthesis of  
WO<sub>3</sub> nanorods for energy and  
environment**

TUTOR: PROF.SSA E. BRUNO

PROF. S. MIRABELLA

COORDINATORE: G. COMPAGNINI

---

TESI PER IL CONSEGUIMENTO DEL TITOLO DI DOTTORE DI RICERCA



*To my family*

## **Cover**

SEM image of  $\text{WO}_3$  urchin-like nanostructures, a novel combined nanostructures obtained by Hydrothermal synthesis. More details can be found within the Summary of this thesis.

*Optimized hydrothermal synthesis of  $\text{WO}_3$  nanorods for energy and environment*

*Giacometta Mineo*

**Ph.D. Thesis, University of Catania  
Printed in Catania, November 2022**

*“It only put me in Gryffindor,” said Harry in a defeated voice, “because I asked not to go in Slytherin”, “exactly” said Dumbledore, beaming once more. “Which makes you very different from Tom Riddle. It is our choices, Harry, that show what we truly are, far more than our abilities.”*

*From Harry Potter and the Chamber of Secrets*

*J. K. Rowling*





## Index

<b>THE FASCINATING WORLD OF WO<sub>3</sub></b> .....	<b>9</b>
1.1 HISTORICAL PERSPECTIVE .....	10
1.2 WO <sub>3</sub> PROPERTIES .....	14
1.2.1 Crystallographic properties of WO <sub>3</sub> .....	14
1.2.2 Electronic band structure of WO <sub>3</sub> .....	16
1.2.3 Optical and chromic properties of WO <sub>3</sub> .....	17
1.2.4 Photocatalytic and electrochemical properties of WO <sub>3</sub> .....	20
1.3 WO <sub>3</sub> NANOSTRUCTURES .....	21
1.4 AIM OF THE THESIS .....	25
<b>HYDROTHERMAL SYNTHESIS OF WO<sub>3</sub> NANOSTRUCTURES</b> .....	<b>27</b>
2.1 OVERVIEW ON SYNTHESIS TECHNIQUES OF WO <sub>3</sub> NANOSTRUCTURES .....	28
2.1.1 WO <sub>3</sub> 1D nanorods: key features in hydrothermal synthesis .....	33
2.2 OPTIMIZATION OF THE WO <sub>3</sub> SYNTHESIS .....	34
2.2.1 Effect of the pH and the substrate .....	36
2.2.2 Growth mechanism and kinetics .....	41
2.3 CHARACTERIZATION OF WO <sub>3</sub> NANOSTRUCTURES .....	43
2.3.1 Elemental characterization .....	43
2.3.2 Morphological and structural characterization .....	45
2.3.3 Optical characterization .....	47
2.4 CONCLUSION .....	49
<b>WO<sub>3</sub> NANORODS FOR GAS SENSING</b> .....	<b>51</b>
3.1 THE ROLE OF GAS SENSOR .....	52
3.2 ELECTRODE REALIZATION AND CHARACTERIZATION .....	53
3.3 H <sub>2</sub> SENSING BY WO <sub>3</sub> NANORODS .....	57
3.3.1 State of the art .....	57
3.3.2 H <sub>2</sub> sensing performances measurements .....	58
3.4 H <sub>2</sub> -WO <sub>3</sub> INTERACTION MECHANISM .....	59
3.4.1 Simulation of experimental curves .....	61
3.4.2 H <sub>2</sub> sensing mechanism .....	65
3.5 NO SENSING BASED ON WO <sub>3</sub> NANORODS .....	68

3.5.1 State of the art.....	68
3.5.2 NO sensing measurements .....	69
3.6 NO-WO <sub>3</sub> INTERACTION .....	71
3.6.1 Simulation of experimental curves.....	72
3.6.2 NO sensing mechanism.....	74
3.7 CONCLUSION .....	75
<b>ENGINEERING HEXAGONAL/MONOCLINIC WO<sub>3</sub> PHASE JUNCTIONS TO IMPROVE ELECTROCHEMICAL HYDROGEN EVOLUTION REACTION .....</b>	<b>78</b>
4.1 H <sub>2</sub> : A GREEN SOURCE OF ENERGY .....	79
4.1.1 Overview on WO <sub>3</sub> based HER.....	81
4.2 ENGINEERING WO <sub>3</sub> BASED CATHODE .....	82
4.3 ELECTROCHEMICAL H <sub>2</sub> PRODUCTION .....	87
4.3.1 HER catalytic performance .....	87
4.4 EFFECT OF THE HEXAGONAL/MONOCLINIC PHASE JUNCTION PRESENCE .....	96
4.5 THE HER MECHANISM .....	98
4.6 CONCLUSION .....	99
<b>WO<sub>3</sub> NANORODS FOR ELECTROCHEMICAL ENERGY STORAGE.....</b>	<b>102</b>
5.1 ELECTROCHEMICAL ENERGY STORAGE .....	103
5.1.1 Overview on WO <sub>3</sub> as pseudocapacitor.....	105
5.2 ELECTRODE REALIZATION AND CHARACTERIZATION .....	105
5.3 SPECIFIC CAPACITANCE QUANTIFICATION .....	108
5.4 INVESTIGATION OF ENERGY STORAGE MECHANISM .....	113
5.4.1 Surface and diffusion limited mechanisms .....	113
5.4.2 Kinetic mechanism of energy storage.....	116
5.5 PROTOTYPE AND COMPARISON WITH LITERATURE .....	119
5.6 CONCLUSION .....	121
<b>CONCLUSION AND PERSPECTIVE .....</b>	<b>124</b>
<b>A1: ELECTRODEPOSITION OF WO<sub>3</sub> NANOSTRUCTURED FILM .....</b>	<b>127</b>
A1.1 SYNTHESIS AND MORPHOLOGICAL CHARACTERIZATION.....	127
A1.2 NUCLEATION AND GROWTH MODEL .....	133
A1.3 CONCLUSION.....	140
<b>A2. ADDITION OF CAPPING AGENT.....</b>	<b>142</b>

<b>A3: WO<sub>3</sub> AS CATALYST FOR SOLID STATE H<sub>2</sub> GAS STORAGE .....</b>	<b>143</b>
A3.1 MIXTURE PREPARATION AND CHARACTERIZATION .....	144
A3.2 PCT ANALYSIS .....	146
A3.3 CONCLUSION.....	147
<b>A4. CYCLIC VOLTAMMETRY IN THE NON-FARADAIC REGION .....</b>	<b>149</b>
<b>A5. SUPPLEMENTARY ELECTROCHEMICAL MEASUREMENTS .....</b>	<b>150</b>
<b>REFERENCES.....</b>	<b>152</b>
<b>LIST OF PUBLICATIONS .....</b>	<b>182</b>
<b>CURRICULUM VITAE.....</b>	<b>183</b>
ORAL PRESENTATION .....	184
POSTER PRESENTATION .....	185
SCHOOL .....	185



# Preface

The possibility of synthesizing materials in the nanoscale and of modifying its chemical and physical parameters allows optimize more and more devices for emerging technologies. Nanomaterials are characterized by structure-dependent physical and chemical properties, unique shape and size, and high surface to volume ratio, that make them the most versatile materials to open new opportunities in science and technologies. Metal oxide semiconductors can be easily synthesized in nanostructured form, and they have emerged as smart materials which possess a wide range of controllable properties. Among them,  $\text{WO}_3$  is an *n*-type semiconductor with an indirect bandgap ranging between 2.6-3.2 eV, and a high chemical and physical stability, which make it the most suitable candidate for many applications, such as sensing, electrochromic smart windows, electrochemical energy storage and electrochemical and photoelectrochemical water splitting.  $\text{WO}_3$  was synthesized for the first time in 1841 by Robert Oxland and immediately aroused a great interest because of its chromogenic ability and its exceptional electric properties. In the last decades,  $\text{WO}_3$  was in depth studied and analyzed, being an almost ideal system from an experimental point of view thanks to its properties (easy to be nanostructured, suitable band gap, possibility to obtain different crystalline structures, ...).  $\text{WO}_3$  nanostructures can be synthesized by various methods, though many of these require difficult and more extensive experimental setups. Among them, the hydrothermal synthesis represents a low cost, easy, and high reproducible technique for the  $\text{WO}_3$  nanostructures synthesis. Morphology and crystal structure can be controlled by simply changing the synthesis parameters, as well as the pH of the solution, the capping agent or the thermal treatment, and the synthesis is highly reproducible. In this thesis, the attention is reserved to  $\text{WO}_3$  1D nanostructures, since they are the suitable candidates for many applications, thanks to their unique morphology and surface to volume ratio. A careful analysis of the most important hydrothermal synthesis parameters (pH,

annealing time and role of the substrate) is conducted, leading to an optimization of the synthesis procedure to obtain well defined hexagonal  $\text{WO}_3$  nanorods and urchin-like nanostructures. The growth mechanism is studied to highlight the role of the substrate during the synthesis procedure. Moreover, post synthesis annealing procedures allowed to modify the crystal structure of  $\text{WO}_3$  nanorods, thus obtaining a hexagonal-monoclinic phase junction which allows to improve the electrochemical activity. In this way, the obtained  $\text{WO}_3$  nanostructures with optimized morphology and crystal phases are investigated for sensing, electrochemical water splitting and energy storage applications.

The thesis is organized as follows:

- the first chapter is an introduction to  $\text{WO}_3$  and to nanotechnology. The fundamental properties of  $\text{WO}_3$  are presented as well as the most important field of applications. The improvement due to the nanotechnology is described, and different  $\text{WO}_3$  nanostructures with different properties are showed;
- in the second chapter, the synthesis procedure of  $\text{WO}_3$  nanostructures are presented, by focusing on advantages and disadvantages of each one. The careful investigation of the hydrothermal synthesis is described, with the purpose of defining the role of the synthesis parameters (pH, annealing time and capping agent) in the morphology and crystal structures of the obtained  $\text{WO}_3$  nanostructures. The optimization procedure for the synthesis of well-defined hexagonal  $\text{WO}_3$  nanorods and urchin-like nanostructures is reported;
- the third chapter reported the realization of a low-cost sensor device by using the hexagonal  $\text{WO}_3$  nanorods. The  $\text{H}_2$  sensing performances are presented and studied, to determine the active mechanisms which describe the  $\text{H}_2$ - $\text{WO}_3$  interaction during the response and recovery phase. The same electrode is used for the NO sensing. The sensing performance are reported and studied and a suggestion of a model

which describe the active mechanisms during the response and recovery phase is presented;

- the fourth chapter reports a post-synthesis thermal treatment leading to a crystal phase transition.  $\text{WO}_3$  nanorods with different concentration of hexagonal-monoclinic phase junctions are obtained and used for the realization of a  $\text{WO}_3$  nanorods-based electrode for the electrochemical hydrogen production. The electrochemical catalytic properties are studied as a function of the crystal phase composition. Exceptional results are obtained for the electrode which possesses an equal content of hexagonal and monoclinic crystallites;
- the fifth chapter reports the study of  $\text{WO}_3$  nanostructures for energy storage application as a function of the morphology and crystal structure. Exceptional energy storage activity is obtained for the pure hexagonal  $\text{WO}_3$  nanostructures if both urchin-like nanostructures and nanorods are present. This electrode was used for the realization of an asymmetric supercapacitor, showing promising performances over a large range of energy and power ranges.
- The Appendix reports our additional studies on  $\text{WO}_3$  carried out during these three years; the Appendix A1 reports the study of the electrodeposition for the synthesis of amorphous  $\text{WO}_3$  films. The role of the electrodeposition parameters (such as the applied potential and the deposition time) in the homogeneity of the obtained films is in depth analyzed, and a model of the nucleation process is proposed; the Appendix A3 reports the preliminary studies on the catalytic activity of hexagonal  $\text{WO}_3$  for the solid state  $\text{H}_2$  gas storage if used as biochar catalyst; the Appendix A2, A4, and A5 reports supplementary analysis conducted during the optimization of the hydrothermal synthesis, during the modeling of the gas sensing mechanism and during the study of the electrochemical energy storage process respectively.





# Chapter 1

## The fascinating world of $\text{WO}_3$

*Tungsten oxide appears very interesting thanks to its large number of applications. Indeed, it has many interesting electrical, optical, and structural properties. The first studies dated back to 1837, when for the first time an intense metallic luster was observed in  $\text{LiWO}_3$  [1]. Low dimensional  $\text{WO}_3$  structures have attracted high interest in scientific research, thanks to the possibility to improve the catalytic properties compared to the bulk counterpart. Therefore, the number of publications based on  $\text{WO}_3$  nanostructures applications has rapidly increased in recent years [2].*

*In this chapter, the  $\text{WO}_3$  applications are briefly reviewed and described, followed by a dissertation on the physical properties of  $\text{WO}_3$ . The advantages of the nanotechnology are shown, as well as the improvement of the catalytic activity of  $\text{WO}_3$  nanostructures compared with the bulk counterpart.*

### 1.1 Historical perspective

Tungsten trioxide ( $\text{WO}_3$ ) is a versatile  $d^0$ -transition metal oxide, which possesses a vast number of sub-stoichiometric and polymorphs compositions, which result in different physical and chemical properties. The structural flexibility and the cation intercalation states of the  $\text{WO}_3$  open the way to many applications, such as chromogenic, photocatalytic, and sensing application.  $\text{WO}_3$  was synthesized for the first time by Robert Oxland in 1841 from sodium tungstate [3] and has been investigated since the XIX century, because of its unusual chromic (the emission of an intense metallic luster) and electrical properties (superconductivity at very low temperature and metal–insulator phase transitions) [1]. Figure 1.1 shows the color change (from pale yellow to deep blue) of  $\text{WO}_3$  powder and of the deionized water solution-based after the



Figure 1.1 Photograph of powders and corresponding deionized water suspension after the interaction with different  $\text{H}^+$  ion concentrations in acidic electrolyte [4].

interaction with different H<sup>+</sup> ion contents in acid electrolyte [4]. The color change is due to the oxygen vacancy formation as will be discussed later. The possibility to reversibly change the optical transmittance and the color under external stimuli makes the WO<sub>3</sub> thin films the most studied chromogenic materials by the scientific community since 1969, when Deb proposed the possibility to use WO<sub>3</sub> for the development of electrochromic devices such as smart windows [5- 9].

Recently, WO<sub>3</sub> aroused great interest in photocatalytic applications. TiO<sub>2</sub> is the most used material in this field of application, thanks to its high photocatalytic activity. The main TiO<sub>2</sub> limitation is due to the limited absorbed sunlight portion. In fact, TiO<sub>2</sub> can absorb only UV light, which is a small portion of the solar spectrum. The band gap values of WO<sub>3</sub> (2.5 eV- 3.5 eV) [2] make it a suitable candidate for the development of a visible-light-driven-semiconductor photocatalyst, by overcoming the TiO<sub>2</sub> limitations [10, 11]. Figure 1.2 shows a schematic of the mechanism of electron-hole pair formation and dye degradation [11]. The photo-generated holes/electrons can oxidize/reduce many organic compounds and dyes, thanks to the catalytic degrading power of WO<sub>3</sub> and the catalytic activity towards electrochemical application such as the water splitting [10, 12].

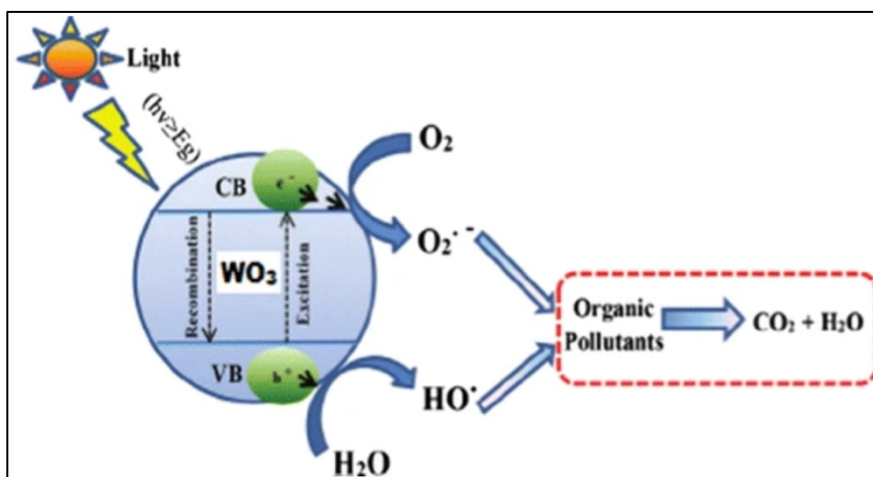


Figure 1.2 Schematic representation of the electron-hole pairs formation and of the organic pollutant degradation in WO<sub>3</sub> after sunlight irradiation [11].

WO<sub>3</sub> easily interacts with reducing gases and this affinity has been widely studied by the scientific community. Optical and the electrical properties changes after the exposure to reducing gases makes WO<sub>3</sub> a suitable candidate also for optical and electrical gas sensor development [8, 13]. The first WO<sub>3</sub> gas sensor is realized by Shaver in 1967 which tested different H<sub>2</sub> concentration at different temperatures. Shaver observed a reversible resistance variation with a certain temperature dependence after the exposure to different H<sub>2</sub> concentration. [13]. These pioneering results open the route to the development of increasingly efficient chemoresistive sensors, by testing also other gases such as NO<sub>x</sub> and H<sub>2</sub>S [14, 15].

Figure 1.3 shows the current study on the use of the metal oxide semiconductor for the development of gas sensing device, in which the paper on WO<sub>3</sub> represents the 9 % of the total studies about gas sensing [16].

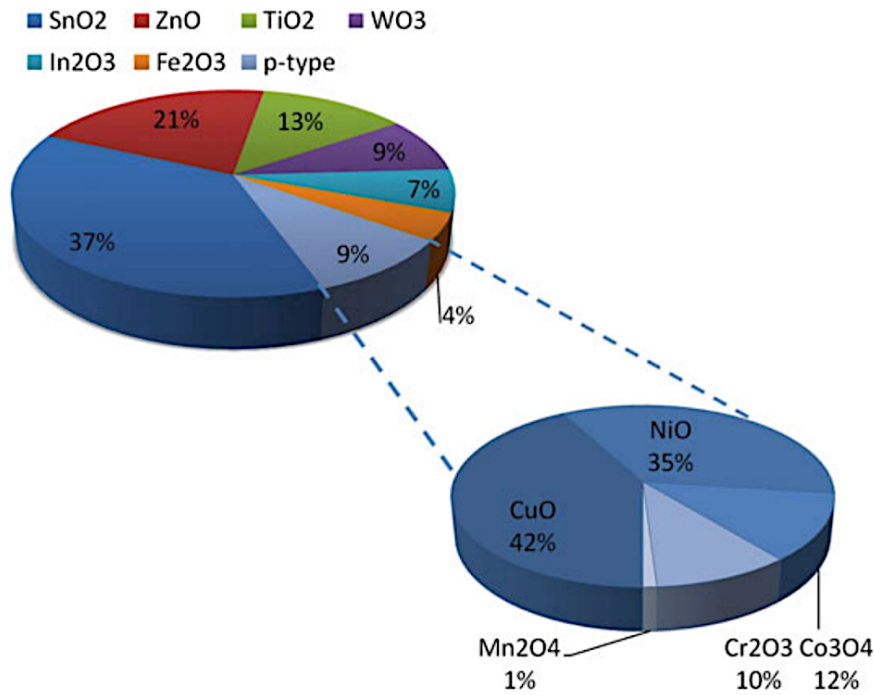


Figure 1.3 Distribution of current studies about the use of metal oxide semiconductors for gas sensing applications [16].

$\text{WO}_3$  was also tested under extreme conditions. The stability in acidic environment and the resistance to the electrochemical corrosion has aroused a large interest in the development of  $\text{WO}_3$  based electrodes for electrochemical applications in which acidic electrolyte are used [17]. The typical tunnel-like structures of the hexagonal crystal phase facilitates the electrolyte ions insertion, which can be stored in the  $\text{WO}_3$  matrix thanks to its multiple oxidation states [18]. Depending on the used electrolyte ( $\text{Li}^+$  or  $\text{H}^+$  ion-based electrolytes),  $\text{WO}_3$  possesses a battery or a pseudocapacitor behavior respectively, since diffusion, or surface, or a combination of both limiting mechanisms can occur at the electrode-electrolyte interface. Figure 1.4 shows the current typical use of  $\text{WO}_3$  and its compounds for the electrochemical energy storage devices. Moreover,  $\text{WO}_3$  can be used as cathode in the development of overall water splitting devices since it shows a catalytic effect

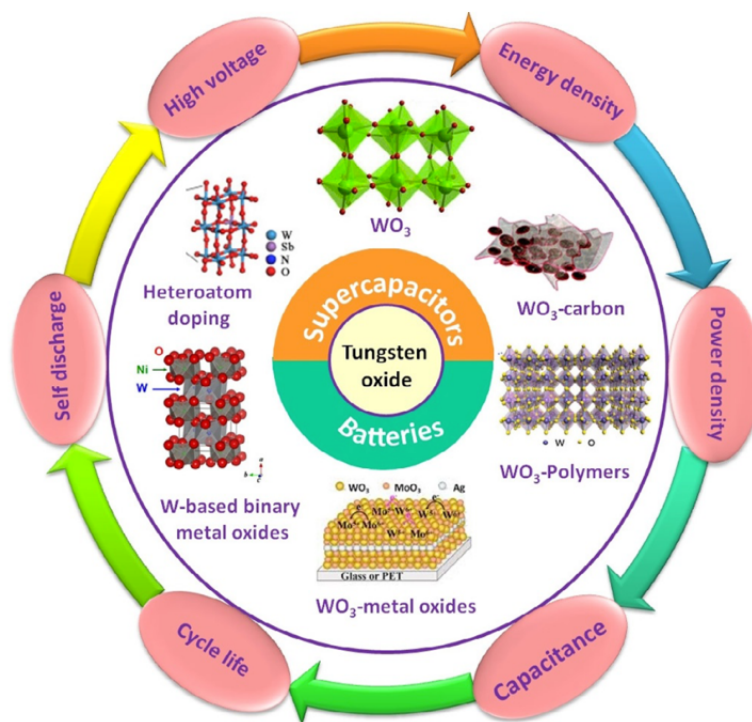


Figure 1.4 Conceptual design describing the combination of tungsten oxide with different nanomaterials for electrochemical energy-storage devices [18].

towards the electrochemical H<sub>2</sub> production in acidic conditions [19]. Also in this case, the electrochemical reaction occurs at the electrode-electrolyte interface, whereby many efforts have been done and will be done to improve the catalytic activity of WO<sub>3</sub> by opportunely engineering the exposed surface. The scientific interest on WO<sub>3</sub> is due to its wide-range of promising applications in many emerging areas, which make it one of the most versatile and studied metal-oxide semiconductors. The performances of WO<sub>3</sub> strongly depend on its physical, structural, and chemical properties which depend on the crystal and electronic band structure, on the stoichiometry and on the morphology of WO<sub>3</sub>. These characteristics can be opportunely tuned by controlling the synthesis parameters, as well as the post-synthesis thermal treatments, as will be described in the following paragraphs, to optimize the electrical, sensing, and electrochemical activity of WO<sub>3</sub>.

### 1.2 WO<sub>3</sub> properties

The present dissertation has the purpose of clarify the main properties of bulk WO<sub>3</sub>, to better understand the versatility of this intriguing metal oxide semiconductor and the reason why it has obtained the attention of the scientific community.

#### 1.2.1 Crystallographic properties of WO<sub>3</sub>

In its crystalline form, tungsten trioxide is made by corner and edge sharing of WO<sub>6</sub> octahedra, in which each W atom is linked to six O atoms as Figure 1.5 (a) shown [2]. Thanks to the high coordination number, WO<sub>3</sub> can possess many crystalline phases, which depends on the rotation direction and tilting angles of WO<sub>6</sub> octahedra (Figure 1.5 a) with respect to the ideal cubic perovskite-like structure. The stability of different polymorphs of WO<sub>3</sub> depends on temperature as follows [18]:

- monoclinic I or  $\gamma$ -WO<sub>3</sub>, which is stable when  $17^{\circ}\text{C} < T < 330^{\circ}\text{C}$  (Figure 1.5 b);

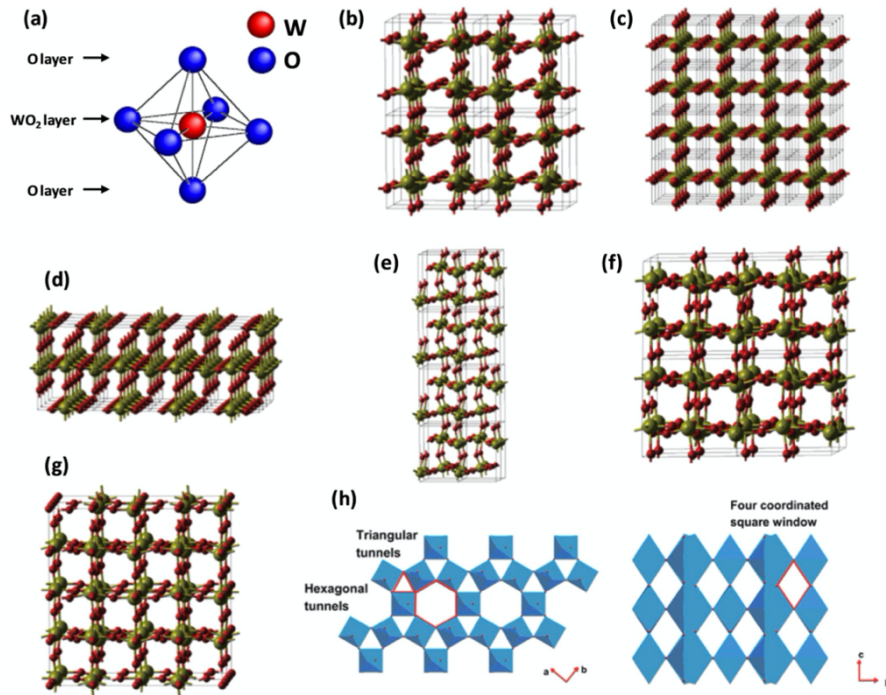


Figure 1.5 Schematic structural models of a)  $\text{WO}_6$  octahedra, b)  $\gamma\text{-WO}_3$ , c) simple cubic  $\text{WO}_3$ , d)  $\alpha\text{-WO}_3$ , e)  $\epsilon\text{-WO}_3$ , f)  $\delta\text{-WO}_3$  and g)  $\beta\text{-WO}_3$  (red and green spheres represents oxygen and Tungsten atoms respectively); h) tunnel structure of hexagonal  $\text{WO}_3$  [18]

- cubic which is not commonly observed experimentally (Figure 1.5 c) because of thermodynamic reasons;
- tetragonal or  $\alpha\text{-WO}_3$ , which is stable when  $T > 740^\circ\text{C}$  (Figure 1.5 d);
- monoclinic II or  $\epsilon\text{-WO}_3$ , which is stable when  $T < -43^\circ\text{C}$  (Figure 1.5 e);
- triclinic or  $\delta\text{-WO}_3$ , which is stable when  $-43^\circ\text{C} < T < 17^\circ\text{C}$  (Figure 1.5 f);
- orthorhombic or  $\beta\text{-WO}_3$ , which is stable when  $330^\circ\text{C} < T < 740^\circ\text{C}$  (Figure 1.5 g);
- hexagonal or h- $\text{WO}_3$  which is obtained from the slow dehydration of tungstite (Figure 1.5 h).

At room temperature the most stable crystal phase is the monoclinic I, but triclinic is also observed. At increasing temperatures, the reversible phase

transition to orthorhombic or tetragonal phase occurs. The hexagonal phase is metastable, and it is turned into a monoclinic I phase when the temperature is higher than 400 °C [2]. Unlike the other crystal structures, in the h- $\text{WO}_3$ , the  $\text{WO}_6$  octahedra share corner oxygen atoms in three- and six-membered ring arrangements along the (001) plane. This sharing forms three different types of tunnels in the W-O bulk structure, that are triangular and hexagonal cavities along the  $ab$  plane and square windows along the  $c$  axis, as shown in Figure 1.5 h. These tunnels can provide accommodation sites for many cations during electrochemical process [18].

Non-stoichiometric forms of tungsten oxide are very common since the lattice may contain a considerable amount of oxygen vacancies; in this case we talk about  $\text{WO}_x$ . Crystal structure depends on the stoichiometry since as the  $x$  value decreases pocket of shear planes are formed by the groups of edge-sharing  $\text{WO}_6$  octahedra. With further reduction of  $x$ , these shear planes interact each other until they align in parallel, by filling the space between the  $\text{WO}_6$  octahedra by resulting in a crystal shear mechanism [2].

### 1.2.2 Electronic band structure of $\text{WO}_3$

The band structure of a semiconductor influences many physical properties, whereby its precise and detailed knowledge is required to improve its catalytic activity.  $\text{WO}_3$  is a  $n$ -type semiconductor with conduction and valence bands (CB and VB, respectively) formed by empty W 5d and filled O 2p orbitals, respectively. The electrical conduction depends on the free electrons concentration in the CB [20]. Crystal structure and morphology affect the electronic band structure of  $\text{WO}_3$ , since the crystal distortion modifies the electronic occupation of the VB and CB, leading a modification of the energy gap value [2]. Figure 1.6 shows the dependence on crystal structure of the Density of States (DOS) of VB and CB and of the energy gap on crystal structure, defined by using the Density Functional Theory (DFT) [21]. The stoichiometry represents a crucial parameter for the semiconductor or metallic nature of  $\text{WO}_x$ . The electrical properties of  $\text{WO}_3$  are affected by the oxygen vacancy concentration since the removal/addition of oxygen atoms from/into the lattice affects the Fermi level position and the concentration of free charge



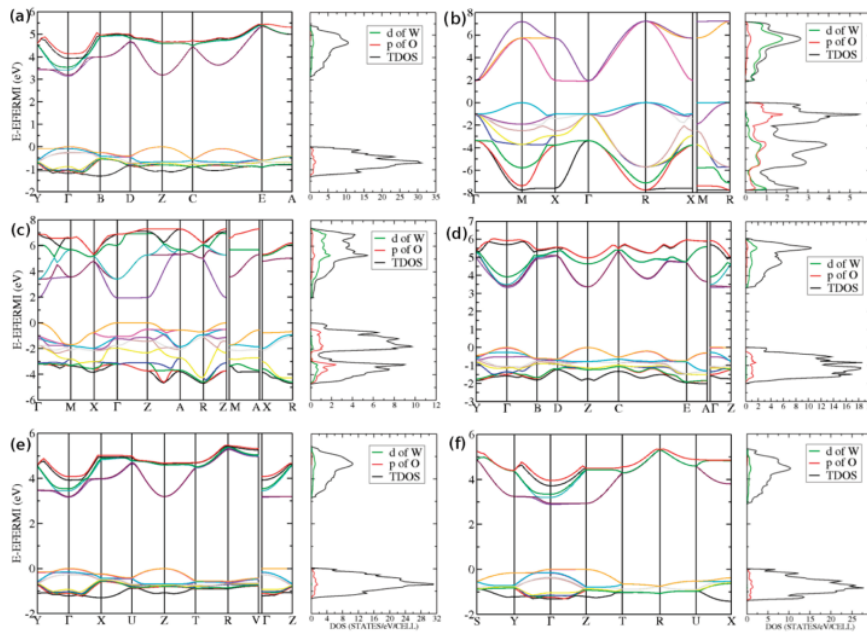


Figure 1.6 Band structure and density of states (DOS) by the standard B3LYP hybrid functional for various structures of  $\text{WO}_3$ : (a) room-temperature monoclinic; (b) simple cubic; (c) tetragonal; (d) low-temperature monoclinic; (e) triclinic; and (f) orthorhombic structures [21]

carriers. As consequence, by simply changing the stoichiometry of  $\text{WO}_3$ , its electrical properties can be improved since small amounts of oxygen vacancy can strongly increase the conductivity leading to a band gap decreasing (from 3.2 to 2.5 eV) [2, 20, 22].

### 1.2.3 Optical and chromic properties of $\text{WO}_3$

$\text{WO}_3$  possesses an optical absorption range which can cover the UV, the visible and the near-infrared region of the electromagnetic spectrum, since band-to-band transition, absorption by localized surface plasmon resonance, and polaron hopping can occur. In the visible region the optical absorption is dominated by the adsorption threshold, defined by the band gap energy of the material and so on the stoichiometry [20]. Stoichiometric  $\text{WO}_3$  appears yellow, since band-to-band transitions occur with an absorption edge near 420 nm which corresponds to the violet emission. The sub-stoichiometric  $\text{WO}_x$

possesses different coloring, ranging from blue to brown, depending on the amount of oxygen vacancy [20]. This behavior is due to the introduction of defect levels by the oxygen vacancies, which result in a polaron formation and related absorption mechanisms. Severe oxygen lacks leads to a high charge carrier density, which results in a strong near-infrared region (NIR) absorption due to the absorption by localized surface plasmon resonance [20]. Figure 1.7 shows the transmittance spectra variation after the ozone exposure of  $\text{WO}_x$  thin films at different temperatures. The ozonation leads to a stoichiometric variation which results in a different optical behavior, especially in the NIR [23].

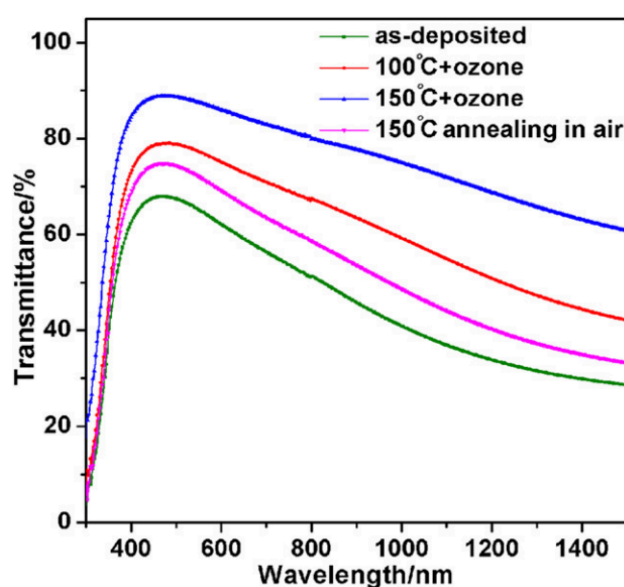


Figure 1.7 Transmittance spectra of different  $\text{WO}_x$  thin films after different ozone exposure [23].

The optical transmittance of  $\text{WO}_3$  can be modulated by external stimuli, resulting in a reversible color change from yellow to dark blue. Electrochromism and gaschromism are the most studied color change processes which occur after the application of a voltage bias or after the exposure to a reducing gas respectively [2]. According to Deb [1], the chromogenic mechanism can be explained with the formation of a defect state

(oxygen vacancy  $V_O^0$ ) inside or near the VB, which occurs after the interaction with positive ions ( $\text{H}^+$ ,  $\text{Li}^+$ ,  $\text{Na}^+$ ) found in the electrolyte solution or in the atmosphere (in electrochromic and gaschromic cases respectively). These defect states hold two electrons and produce  $\text{W}^{4+}$  or  $2\text{W}^{5+}$  states, as shown in Figure 1.8. The removal of one electron from the  $V_O^0$  state leads a  $V_O^0$  conversion to  $V_O^+$  and these positively charged defect states produce a coulombic repulsion to the nearest W-ions, which results in an upward shift

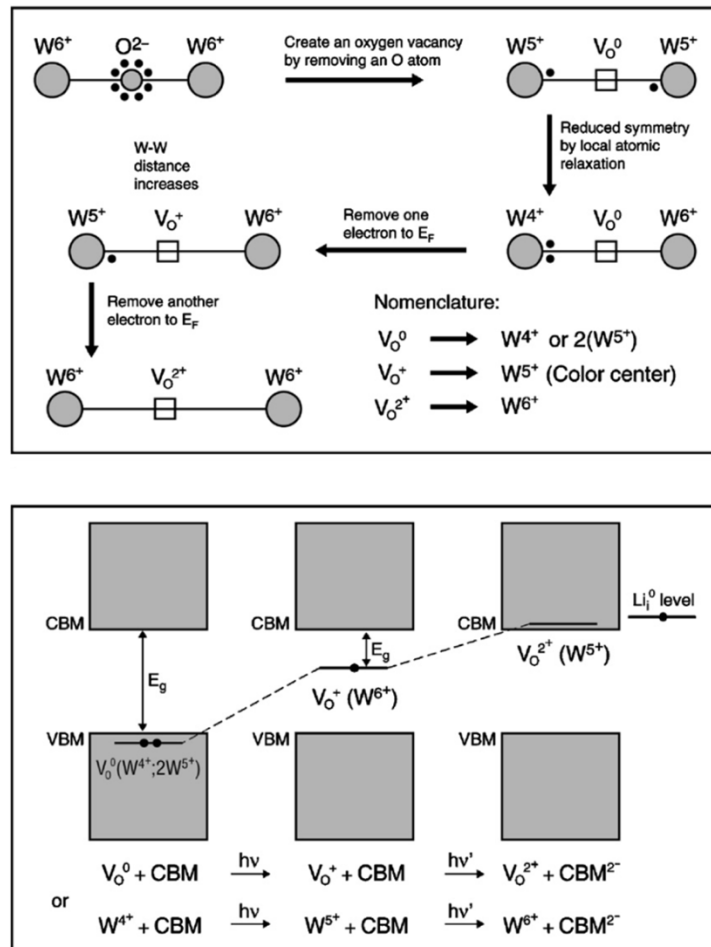


Figure 1.8 Model of the chromic mechanism based on the formation of oxygen vacancy defect states [1].

of the defect level into the bandgap, by creating a color center. Amorphous WO<sub>3</sub> possesses higher degree of color change compared to their crystalline counterparts, thanks to the spatial separation between the localized inserted electrons and the inserted cations. Instead, in the crystalline structure, the inserted electrons are not localized since they possess a Drude-model-like free electrons behavior [2].

### 1.2.4 Photocatalytic and electrochemical properties of WO<sub>3</sub>

WO<sub>3</sub> aroused a large interest in scientific community thanks to its catalytic role, which can be ascribed to the energy position of its CB and VB. Figure 1.9 shows the energy edges position (in Volts versus Normal Hydrogen Electrode NHE) of CB and VB (red and green respectively) of several semiconductors in contact with a pH 1 electrolyte. The VB edge position makes the WO<sub>3</sub> a suitable candidate for the electrochemical photo-oxidation

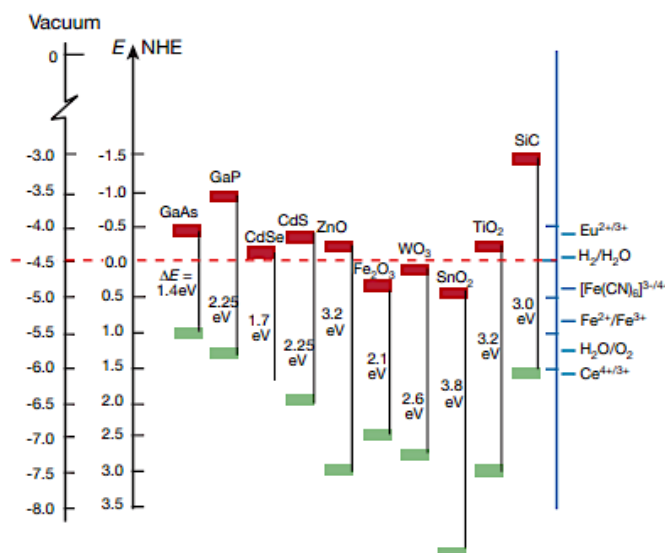


Figure 1.9 Band positions of several semiconductors in contact with aqueous electrolyte at pH 1. The lower/upper edge of the conduction/valence band (red and green bars, respectively) are presented with the band gap in electron volts [24].

of a wide range of organic compounds thanks to the strong oxidative OH<sup>-</sup> species which can be generated [2, 17].

Moreover, the narrow band gap (2.5 eV-3.5 eV), results in a high absorption of the visible light, which is the biggest portion of the Sun radiation, thus opening the route to TiO<sub>2</sub> replacement. WO<sub>3</sub> is stable under acidic condition and its CB edge is near the H<sub>2</sub>/H<sub>2</sub>O production level. These properties suggest a certain affinity of WO<sub>3</sub> for the electrochemical Hydrogen Evolution Reaction (HER), which represents one of the most studied fields of application of the last years. WO<sub>3</sub> possesses a high theoretical capacitance, natural abundance, and low-cost production. These properties suggested a tendency to electrochemical energy storage application, even because WO<sub>3</sub> can interact with small positive ions from electrolyte, such as H<sup>+</sup>, Na<sup>+</sup>, Li<sup>+</sup> and K<sup>+</sup>, by producing reversible electrochemical reactions. The specific capacitance, as well as the charge and discharge rate, depend on the kinetics of the electrochemical reactions described in terms of transportation of electrons and ions from the electrolyte to the electrode and vice versa [18]. First studies on the electrochemical energy storage mechanism of WO<sub>3</sub> date back to 1993, by using sputtered WO<sub>3</sub> thin films as electrodes and Li<sup>+</sup> ions-based electrolytes. The kinetics of Li<sup>+</sup> intercalation is studied by performing Cyclic Voltammetry (CV) and Galvanostatic Charge and Discharge (GCD) analysis, thus obtaining the promising results on which all the literature has been then based [25, 26].

### 1.3 WO<sub>3</sub> nanostructures

The properties described above are related to the bulk structures and can be modified and improved with the help of the nanotechnology, which is introduced firstly in 1959, during the famous lecture “*There is Plenty of Room at the Bottom*” at Caltech by Feynman. The nanotechnology is the manipulation and manufacture of materials on the nanometric scale ( $\sim 10^{-9}$  m) and allowed to open new opportunities in most of research areas, since nanoscale materials shown unique physical and chemical properties compared with their bulk state, depending on their unique shape and size [27]. In fact, for the nanostructured form it is possible to obtain [28]:

- a greater surface-to-volume ratio compared to bulk form, that provides more surface area for physical and chemical interactions;
- quantum confinement effects due to the small size of nanostructured forms that influences optical properties, electronic band structure and electrical charge transport;
- significantly altered surface energy, which can be used to modify the bond structures of atomic species close to the surfaces.

These unique conditions makes nanostructures suitable for many applications, such as microelectronics (memories, transistors, etc.), optics (laser waveguides, LEDs, etc.), solar cells. energy harvesting and storage (photovoltaic, supercapacitors etc.), water splitting, sensing (gases, pH, (bio)molecules, heavy metals, etc.) and so on.

The nanotechnology advent leads to an increased interest in the synthesis of WO<sub>3</sub> nanostructures, as well as the synthesis of many nanostructured metal oxide (MO), thanks to the possibility to improve their catalytic properties simply by changing their morphology, dimension, and crystal structures. Moreover, most of the MO nanostructures are characterized by the presence of always fully filled s-shells and partially filled d-shells, which contributes to determine a typical semiconductive behavior, required for a wide range of application [29]. Different synthesis techniques can be used to produce MO nanostructures, such as high temperature vapor phase deposition (sputtering, evaporation, pulsed laser deposition PLD and molecular beam epitaxy MBE) and low temperature solution routes (electrodeposition, sol-gel, solvothermal and hydrothermal synthesis). In the latter cases, the morphology, dimension, and crystal structure of the obtained nanostructures can be easily piloted by changing parameters such as the pH of the precursor solution, the capping agent, the concentration of the reagents, and the reaction time and temperature. Moreover, the low temperature liquid routes allow to obtain large synthesis yields with high efficiency, by making these procedures the most used in case of massive production of nanostructures. Figure 1.10 shows typical examples of WO<sub>2.72</sub> nanostructures synthesized by using the hydrothermal and solvothermal methods with different reaction times [17]. Nanoparticles, nanorods, and nanobundles can be considered as 0, 1 and 2-D nanostructures respectively and possesses different physical and chemical properties because of the different surface to volume ratio and charge confinement, which occurs

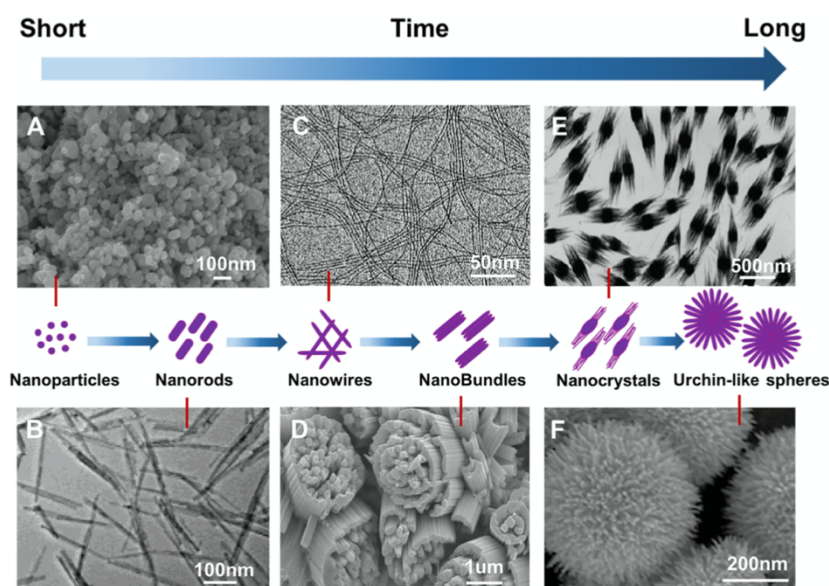


Figure 1.10 Morphologies of  $\text{WO}_{2.72}$  prepared by using the hydrothermal and solvothermal method with different reaction time: (a) nanoparticles, (b) nanorods, (c) nanowires, (d) nanobundles, (e) nanocrystals, and (f) urchin-like spheres [17].

along the nanometric dimension, contrariwise to what happens in the bulk form, where the charge carriers are free to move in all directions [2, 29]. The use of nanostructures instead of the bulk form contributed to the brilliant scientific results on  $\text{WO}_3$  for energy storage, electrochromism, photocatalytic and sensing application [1, 11, 18, 19, 30]. Table 1.1 lists some physical and chemical properties of  $\text{WO}_3$ . Some of them (such as the band gap and the mobility), strongly depend on the crystalline phase and on the nanostructured morphology, by pointing out the possibility to control the chemical and physical properties, thanks to variation in the quantum confinement effect, in the morphology and in the crystalline phase by using the nanotechnology. The high surface to volume ratio of the nanostructured form allows to reduce the mass of the used active material. This aspect is crucial with a view of recycling and decreasing waste, or in case in which noble metal or critical raw materials (CRMs) are used. Figure 1.11 shows a periodic table in which the CRMs are identified according to the CRMs lists drawn up by the European Commission

Properties	Value
Density	7.16 g/cm <sup>32</sup>
Melting Point	2043 K <sup>31</sup>
Optical Reflectivity	0.2 <sup>32</sup>
Band Gap Energy	2.4 eV -3.2 eV
Effective Mass	2.4 m <sub>e</sub> (hole and electron) <sup>32</sup>
Mobility	10-40 cm <sup>2</sup> /Vs (electrons) <sup>31</sup> , 3-10 cm <sup>2</sup> /Vs (holes) <sup>31</sup>
Exciton Binding Energy	15 meV <sup>33</sup>

Table 1.1 Physical and structural properties of WO<sub>3</sub>.

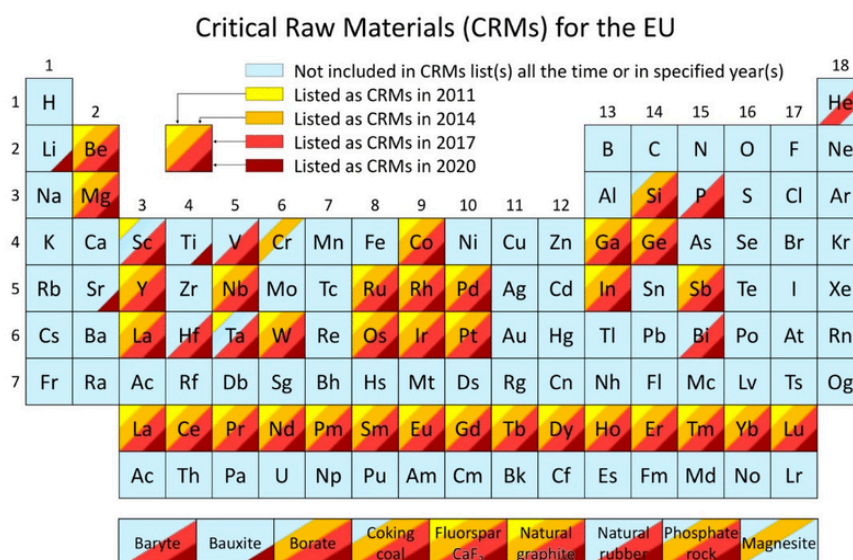


Figure 1.11 Periodic table of elements detailed for the CRMs list since 2011 [35].



Tungsten belong to the CRMs lists since 2011, as well as platinum and palladium, whereby the reduced consumption of these elements is preferable for the development of new generation devices [34].

In the nanostructured form the interaction with the external environment occurs mainly at the interface with the surface of the nanostructures. The effects of quantum confinement, morphology, stoichiometry, and crystal structure modify the CB and VB position, enhancing the catalytic effect towards most of the WO<sub>3</sub> applications. The link between the change of CB and VB position and the catalytic effect is not fully understood, and a complete knowledge is lacking in literature.

### 1.4 Aim of the thesis

The focus of this thesis is the study of the interactions which occur at the surface of WO<sub>3</sub> with the external environment, responsible for the catalytic activity of WO<sub>3</sub> nanostructures for sensing and electrochemical applications as a function of the morphology and crystal structure. By hydrothermal synthesis and subsequent treatment, we obtained hexagonal (or a hexagonal-monoclinic) WO<sub>3</sub> nanorods both in single and in bundle configuration, and in 3D agglomeration form called urchin-like. These nanostructures are tested for H<sub>2</sub> and NO sensors, for the electrochemical H<sub>2</sub> production, and for the electrochemical energy storage. The catalytic activity of WO<sub>3</sub> is in depth analyzed, to define the mechanisms which describe the WO<sub>3</sub>-external environment interactions.



# Chapter 2

## Hydrothermal synthesis of WO<sub>3</sub> nanostructures

*Hydrothermal synthesis is a low cost, simple and safe technique for the growth of nanostructures, characterized by high reproducibility and versatility.*

*WO<sub>3</sub> semiconducting nanostructures grown by hydrothermal synthesis are currently investigated for a wide range of applications. Indeed, this technique allows to obtain different morphologies and crystal structures by simply changing the precursor solution conditions, the solution pH, the concentration of tungsten salt or of capping agent.*

*This chapter presents an investigation of the role of solution pH, of annealing time and of substrate in the growth kinetics of WO<sub>3</sub> nanostructures and their morphology. An optimized procedure for a reproducible synthesis of a specific morphology (nanorods or urchin-like nanostructures) WO<sub>3</sub> is identified and well described. Elemental, morphological, structural, and optical characterizations were carried out to better describe the potentialities of as obtained WO<sub>3</sub> nanostructures.*

## 2.1 Overview on synthesis techniques of $\text{WO}_3$ nanostructures

The nanotechnology advantages in a multitude of applications made the large-scale synthesis of nanostructures a crucial point for the development of promising technologies. Nanostructured  $\text{WO}_3$  can be synthesized by different approaches, such as Vapor-Phase and Liquid-Phase Synthesis. The Vapor-Phase Synthesis involves the condensation of a vaporized source material onto the substrate [2] and two types of deposition can be distinguished: the Physical Vapor Deposition (or PVD) and the Chemical Vapor Deposition (or CVD). PVDs of  $\text{WO}_3$  nanostructures start with a solid source or a powder of  $\text{WO}_x$  that is energetically evaporated through many possible techniques (sputtering, heating, electronic beam...). The deposition parameters can be controlled in such a way that the evaporated species can condense into nanostructured forms with desired nanoscale morphology, size, and crystallinity [2]. Figure 2.1 shows  $\text{WO}_3$  nanostructures synthesized by using PVD methods such as (a) sputtering and (b) thermal evaporation.

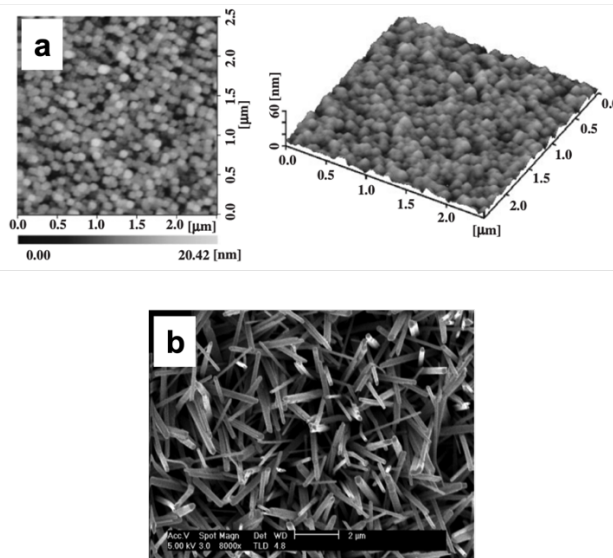


Figure 2.1: (a) AFM (Atomic Force Microscopy) images of (001) oriented  $\text{WO}_3$  film. Reproduced by [36]; (b) SEM (scanning Electron Microscopy) images of  $\text{WO}_3$  nanowire synthesized by thermal evaporation. Reproduced by [37].

CVDs of  $\text{WO}_3$  nanostructures imply the exposure of the substrate to volatile W precursors obtained by heating a W wire, which decompose or react on the substrate surface to produce tungsten compounds. Different pressure and temperature conditions can be used to select the morphology, stoichiometry, and crystal structure [38]. Figure 2.2 shows  $\text{WO}_3$  nanorods grown on carbon nanotubes (CNTs) by using a hot wire CVD [39].

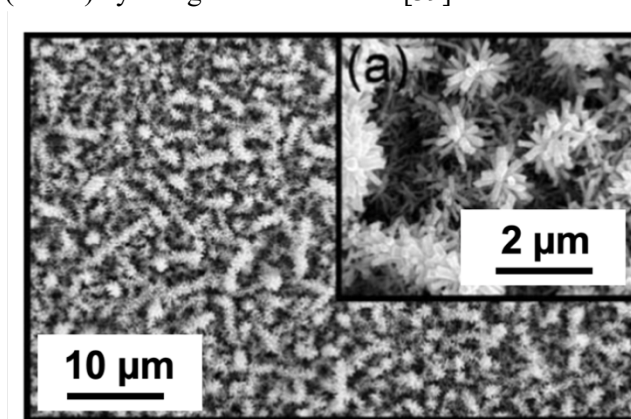


Figure 2.2: (main panel) image of  $\text{WO}_3$  nanorods grown on CNTs by hot wire CVD; (a) magnification view of  $\text{WO}_3$  nanorods. Reproduced by [39].

Vapor phase methods are commonly used for the large-scale synthesis, but the experimental set-up is expensive, as well as the synthesis procedure.

Liquid Phase Syntheses are characterized by simple equipment and low cost. Room temperatures are compatible with these processes, and a good control of morphology can be achieved. Sol-gel, electrochemical anodization, electrodeposition, and hydrothermal are the most used Liquid Phase Syntheses for the grown of  $\text{WO}_3$  in bulk, microstructured and nanostructured form.

The sol-gel process involves the use of a precursor solution, called sol, to form discrete particles or a networked gel structured during the aging process. The peroxotungstic acid solution is generally used as precursor for the  $\text{WO}_3$  synthesis, thanks to its high stability at room temperature and in acidic environment [2]. An example of the typical surface morphology of the sol-gel synthesized  $\text{WO}_3$  films, is shown in Figure 2.3 [40]. The most relevant problem of the sol-gel method is the use of many precursors and gelling agent,

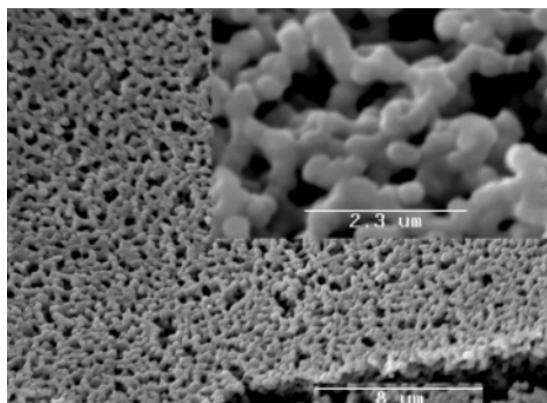


Figure 2.3: SEM image of  $\text{WO}_3$  film obtained by sol-gel method. Reproduced by [40]

and the difficulty to control the final product microstructure since the mechanism of the sol-gel synthesis is not well completely understood [40]. Electrochemical anodization is widely used for industrial synthesis of metal oxide film, thanks to its simplicity. In a typical anodization route, potential is applied between two samples both immersed in a properly liquid electrolyte and electrochemical reactions occur at the surface by leading to an oxide film on the electrodes surface [2]. The anodization current, the temperature of the electrolyte and its composition can be controlled thus influencing the growth of the film. For the synthesis of  $\text{WO}_3$ , a W foil is commonly used as anode by obtaining films whose typical morphology is shown in Figure 2.4 [41]. Unfortunately, the high voltages required for the synthesis and the difficulty to achieve a nanostructured morphology make the anodization technique difficult to perform for the  $\text{WO}_3$  nanostructures synthesis.

Electrodeposition was commonly used for the synthesis of amorphous  $\text{WO}_3$  (see more details on our results in Appendix A1). During electrodeposition a metal oxide film is formed by accumulating metal ions present in the electrolyte. Typically, the most used electrolyte for the synthesis of  $\text{WO}_3$  is a peroxotungstic acid with a certain amount of alcohol with the role of solution stabilizer. The voltage necessary for this synthesis is very low: e.g., -0.5 V versus the reference electrode Ag/AgCl and time ranging between 1 to 30 minutes [42]. Moreover, by controlling the pH of the solution, it is possible to obtain different nanostructures morphologies, as shown in Figure 2.5 [43].

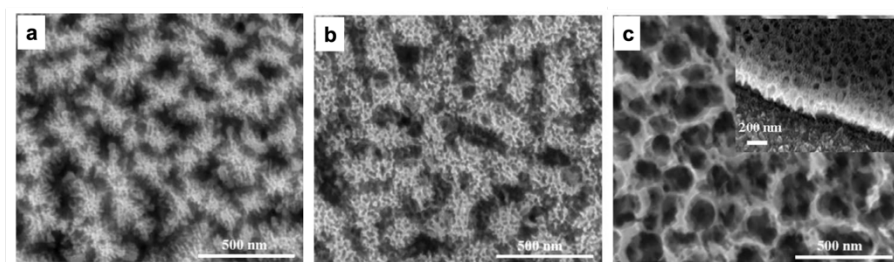


Figure 2.4: WO<sub>3</sub> films obtained by electrochemical anodization by applying (a) 20 V, (b) 40 V and (c) 60 V. Reproduced by [41].

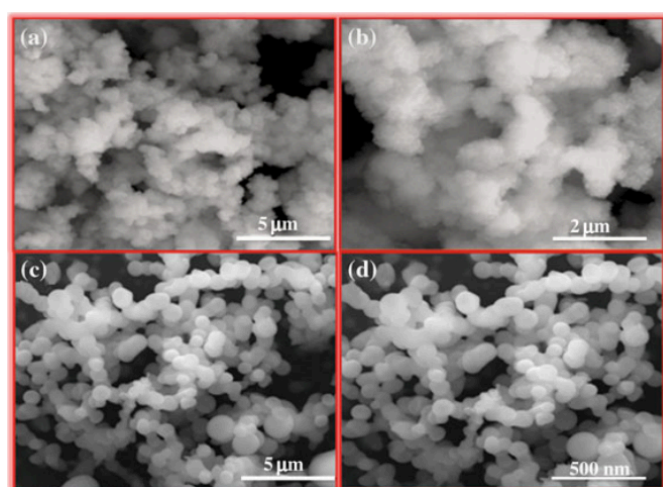


Figure 2.5: WO<sub>3</sub> nanostructures obtained by electrochemical synthesis by using: (a-b) pH 4 and (c-d) pH 3.51 precursor solution. Reproduced by [43].

The biggest problem of electrodeposition is related to the precursor solution, since the peroxotungstic acid solution is difficult to prepare and it is stable only for one week [42], whereby the use of the electrodeposition technique is not suitable for a massive WO<sub>3</sub> nanostructures synthesis.

The hydrothermal procedure represents the greenest, simplest, and most versatile procedure among all the Liquid Phase Synthesis methods commonly used for the synthesis of WO<sub>3</sub> nanostructures. It does not require any external potential and the preparation of the precursor solution occurs in a few steps. The nanostructures formation can occur both in high and low temperature and

pressure conditions and the nanostructures morphology and crystallinity strongly depend on precursor solution components, and on reaction time and temperature [44]. Figure 2.6 shows different WO<sub>3</sub> nanostructures synthesized by the hydrothermal technique by simply varying the reaction time [45]. These characteristics make it our suitable candidate for the synthesis of well-defined WO<sub>3</sub> nanostructures with high morphology and crystal structure control.

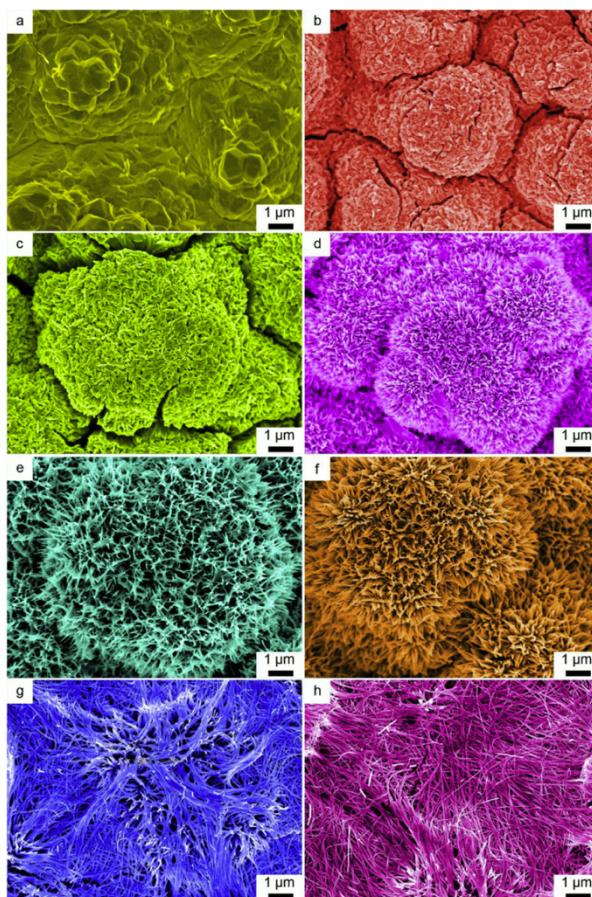


Figure 2.6: SEM images of WO<sub>3</sub> nanofibers grown on Cu substrates at different hydrothermal reaction times. (a) 0 h, (b) 0.5 h, (c) 1.0 h, (d) 2.0 h, (e) 4.0 h, (f) 8.0 h, (g) 12 h, (h) 24 h. Reproduced by [45].



### 2.1.1 WO<sub>3</sub> 1D nanorods: key features in hydrothermal synthesis

Hexagonal WO<sub>3</sub> nanorods are of great interest for electric and electrochemical applications, thanks to their quasi 1D structure and their high exposed surface. In these conditions, the interaction between WO<sub>3</sub> and small ions can occur more easily thanks to the presence of empty hexagonal and trigonal channel which promote the ions intercalation in the WO<sub>3</sub> matrix [46]. The hydrothermal synthesis represents the simplest way to obtain hexagonal WO<sub>3</sub> nanorods, since besides being a very simple and low-cost technique, the morphology and crystal structure can be controlled by simply changing the synthesis parameters. The precursor solution is prepared by using a certain amount of tungsten salt dissolved in water [47-56]. Molar concentration of the solute and solution pH affect the morphology and the growth rate [57], as well as the thermal treatment parameters affect the dimension and the structural quality of the nanostructures [44, 45, 58]. Capping agent is used to define the morphology of the nanostructures, thanks to the interaction which occurs during the thermal treatment, which promotes precise crystalline directions [58, 59]. The hydrothermal synthesis occurs by using a stainless-steel autoclave, whose photograph is shown in Figure 2.7; an inert Teflon liner can be placed inside the stainless-steel shell to contain the precursor solution (typically of aqueous type). Through the screw in the threaded cover, tightened with the booster stick, the available precursor solution volume is maintained constant regardless of the external temperature and internal pressure conditions. Typically, the reaction temperature is higher than 100 °C, in such a way that a high-pressure condition occurs inside the Teflon liner by leading in the nucleation process of nanostructures.

Yao et al. synthesized hexagonal WO<sub>3</sub> nanorods by using the sodium tungstate dihydrate as precursor salt, sodium sulfate (Na<sub>2</sub>SO<sub>4</sub>) and oxalic acid (H<sub>2</sub>C<sub>2</sub>O<sub>4</sub>) as capping agents at 180°C for 6 hours [56]; Wei et al. synthesized hexagonal cauliflower-like nanostructures by using the sodium tungstate dihydrate for the precursor solution (pH 1), and the ammonium tartrate as capping agent at 180°C for 18 hours [54]; Wang et al. controlled the morphologies and the growth direction of hydrothermally synthesized WO<sub>3</sub> nanostructures by varying the added citric acid amount in the precursor solution [52]; Kondalkar

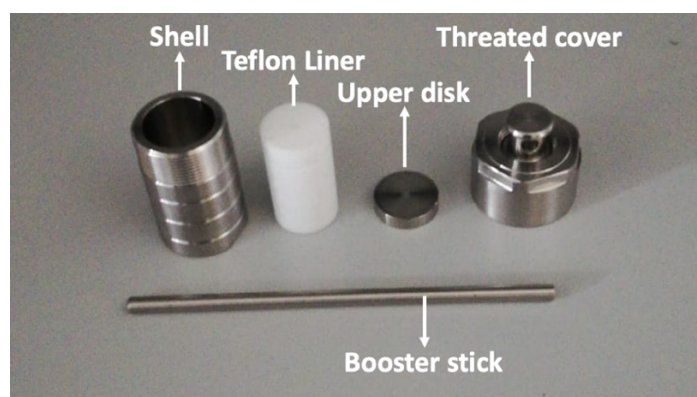


Figure 2.7 A photograph of the stainless-steel autoclave reactor for hydrothermal synthesis.

et al. [60] insert a fluorine doped tin oxide (FTO) coated glass with a thin  $\text{WO}_3$  seed layer in the liner during the thermal treatment, by observing that the nucleation occurs directly on the substrate surface homogeneously rather than in solution. Other many examples confirm the versatility of the hydrothermal synthesis for the synthesis of  $\text{WO}_3$  nanostructures [47-51, 53, 55, 57, 61-63]. Because of the role of the growth conditions in the final morphology, crystal structure and stoichiometry of the nanostructures, the hydrothermal synthesis of hexagonal  $\text{WO}_3$  nanorods requires some optimizations, to obtain well-defined nanostructures, with the desired size, stoichiometry, and a high synthesis yield. In the next paragraph the hydrothermal synthesis of hexagonal  $\text{WO}_3$  nanostructures is described in detail, by pointing out the effect of the growth conditions.

### 2.2 Optimization of the $\text{WO}_3$ synthesis

Precursor solution is prepared by using commercial sodium tungstate ( $\text{Na}_2\text{WO}_4$ ) as tungsten salt, hydrochloric acid 3 M (HCl) for acidify until the desired pH, and sodium chloride (NaCl) as capping agent. The latter is commonly used in cases in which a 1D morphology (nanorods or nanowires) is preferred, thanks to the interactions which occurs with the  $\text{WO}_3$  crystal

nucleus. Figure 2.8 shows a schematic representation of the interaction between the  $\text{Na}^+$  ions (yellow balls) and the  $\text{WO}_3$  nuclei (violet blocks).  $\text{Na}^+$  is preferentially adsorbed on the (200) crystal plane ( $a$ -axis) of  $\text{WO}_3$  crystal nucleus, in which the oxygen concentration is higher than that of the (001) plane ( $c$ -axis), thus leading to a  $c$ -axis growth, which results in 1D nanostructures with high length-diameter ratio formation [59].

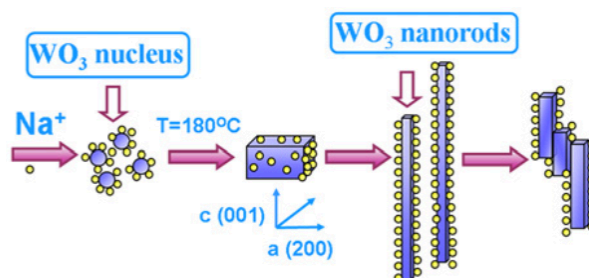


Figure 2.8 Schematic representation of the interaction between the  $\text{Na}^+$  cation (yellow balls) and the  $\text{WO}_3$  crystal nuclei (violet blocks), which results in nanorods formation. Adapted from reference [59].

In our experimental procedure, 0.825 g of  $\text{Na}_2\text{WO}_4$  is added to 19 ml of deionized water and stirred until to obtain a clear solution (about 10 minutes) with a 9.8 pH, whereby a certain amount of HCl is added to reach the desired pH (between 3 and 1.5) [64]. The capping agent (NaCl) can be added before or after the acidification process, thus influencing the yield and quality of the synthesis (see Appendix A2 for details). The latter procedure leads to a massive  $\text{WO}_3$  nanostructures synthesis, whereby 0.5 mg of NaCl is added without mixing further and the as prepared precursor solution is put in a stainless-steel autoclave (25 ml). The closed autoclave is put in a muffle and annealed at  $180^\circ\text{C}$  for different times (from 0.5 to 24 hours), then the autoclave is cooled naturally. The obtained powder is collected and washed several times with deionized water and ethanol by using a centrifuge (6000 rpm for 10 minutes), and then finally dried in a hot plate at  $50^\circ\text{C}$  in air. Different pH values and annealing times were tested, as well as the presence of a substrate inside the liner during the thermal treatment, to highlight the synthesis mechanism and the role of the substrate, with the aim of optimize

the WO<sub>3</sub> nanostructures synthesis for the desired electrical and electrochemical applications.

### 2.2.1 Effect of the pH and the substrate

According to literature, the hydrothermal synthesis of WO<sub>3</sub> nanostructure is typically conducted in acidic environment with pH which are typically lower than 3 [52, 54, 57, 59, 61]. The pH of the precursor solution can be controlled by simply modify the added amount of HCl 3 M. Precursor solution with different pH (from 1.5 to 3) are tested by maintaining constant the reaction time, to better understand the pH role in the nanostructures morphology. The latter was studied by using a field emission Zeiss Supra 25 Scanning Electron Microscope (SEM) system. The used acceleration voltages are typically of 2-5 kV, the aperture is 30 μm and a working distance is 2-3 mm. Both In Lens and SE2 detectors were used to enhance the signal from the secondary electrons generated after the electron beam-sample interaction. Powders obtained from hydrothermal synthesis were dissolved in water with a 4 mg/ml concentration, and some drops of these solutions were drop coated on corning glass for the morphological analysis. Figure 2.9 shows SEM images of WO<sub>3</sub> nanostructures powders on corning glass obtained after 24 h of thermal treatment of (a) 2, (b) 2.4 and (c) 3 pH precursor solution. The lowest pH values produced well-arranged large cylindrical bundles of 1.5-2 μm nanorods lying on top of each other (Figure 2.9 a). By increasing the pH, a disordered dispersion of WO<sub>3</sub> nanostructures appears, and a lot of 1.5-2 μm nanorods and 5-6 μm nanowires are generated at 2.4 and 3 pH, respectively (Figure 2.9 b and c). Such results probably indicate a certain nucleation rate dependence on the pH of the precursor solution. At lower pH a plenty of large WO<sub>3</sub> nuclei rapidly appears, thus leading to a formation of well-ordered stuck nanorods, agglomerated to form larger than long cylinders (Figure 2.9 a). By increasing the pH, the nucleation occurs more slowly and single nanorods appears, which grow independently of each other (Figure 2.9 b). Further increase of pH leads to longer nanorods (nanowires) formation (Figure 2.9 c). This is probably due to the formation of fewer nuclei which can grow a lot along the c-axis, thus resulting in nanowires morphology.

To confirm the pH role in the nucleation process, the morphology of the nanostructures is studied also in the case of lower reaction times. Figure 2.10 shows the SEM images of nanostructures synthesized by using (a) 1.5, (b) 2.2,

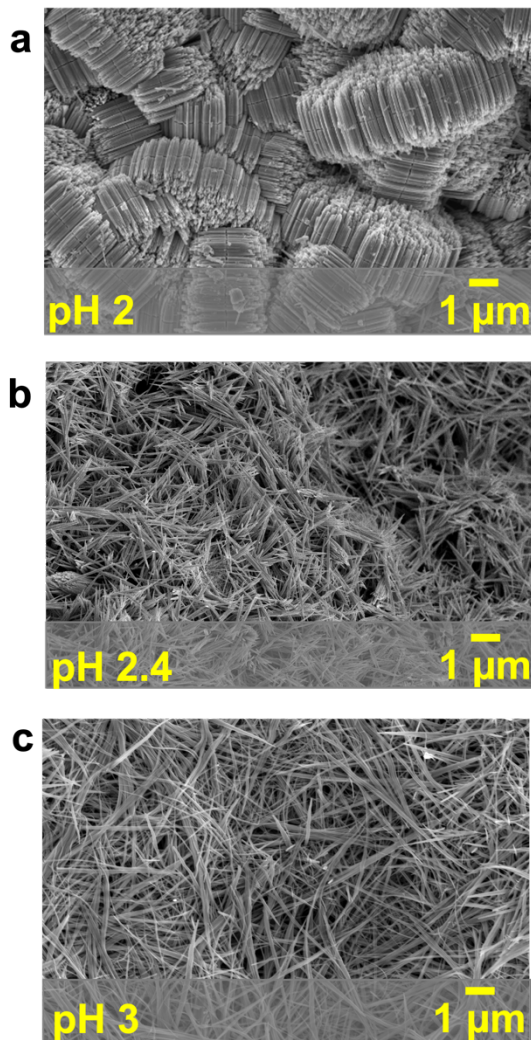


Figure 2.9 SEM images of hydrothermally synthesized  $\text{WO}_3$  nanostructures powders obtained by using precursor solution with different pH: (a) 2, (b) 2.4 and (c) 3, after a 24 hours thermal treatment at  $180^\circ\text{C}$ .

and (c) 2.4 pH precursor solutions after 2 hours thermal treatment. Lower pH (1.5) leads to a desert-rose-like morphology (Figure 2.10 a), with large nanoplates intertwined each other. Each nanoplate shows a granular morphology, thus suggesting a rapid formation of many WO<sub>3</sub> nucleus grouped each others, which can become bundles of nanorods if the reaction time increases. Higher pH values (Figure 2.10 b-c) lead to the formation of single nanorods (as already observed for longer reaction times), pompon-like and urchin-like nanostructures (2.2 and 2.4 pH respectively). Probably the relatively high pH induces a slow nucleation, and most of WO<sub>3</sub> nucleus can grow independently of each other. The presence of pompon-like and urchin-like nanostructures could be due to the presence of few nuclei agglomerations which are more (pompon-like) or less (urchin-like) dense depending on the pH (2.2 or 2.4 respectively). If the reaction time increases, these nanostructures continue to grow until they become long nanowires as those showed in SEM images in Figure 2.9.

According to literature, the hydrothermal synthesis can be carried out by placing in the Teflon liner some substrates to induce the WO<sub>3</sub> nanostructures growth or deposition directly on their surface [57, 60-62, 65]. The role of these substrate is not well clear: Kondalkar et al. [60] suggest that the nucleation occurs directly on the substrate surface, while Shinde et al. [61] described the substrate as a collector of nuclei formed in solution. To clarify the role of the substrate, the synthesis was carried out by placing conductive and insulator substrates, such as Indium Tin Oxide (ITO) coated glass and silicon dioxide (SiO<sub>2</sub>), in the Teflon liner. The synthesis is conducted by using a 2.2 pH precursor solution, thermally treated for 3 hours. After the synthesis each substrate taken from the liner was dried in air and the solution was washed with deionized water and ethanol and centrifugated, to collected WO<sub>3</sub> nanostructures powder. Figure 2.11 shows SEM images of (a) WO<sub>3</sub> nanostructures produced in solution and of nanostructures grown on (b) ITO and (c) SiO<sub>2</sub> substrates when they are inserted in the autoclave (nanostructures in Figure 2.11 a, b and c are obtained during the same hydrothermal synthesis). WO<sub>3</sub> powder is made of nanorods, and urchin-like nanostructures embedded each other, like those obtained with a 2.4 pH precursor solution thermally treated for 2 hours (Figure 2.10 c). The same WO<sub>3</sub> nanostructures can be

observed on the ITO surface (Figure 2.11 b), interspersed with some empty zones (dark grey regions). The similarity between nanostructures inside the collected powders and on ITO surface suggests a deposition of nanostructures formed in solution onto the substrate rather than a growth mechanism

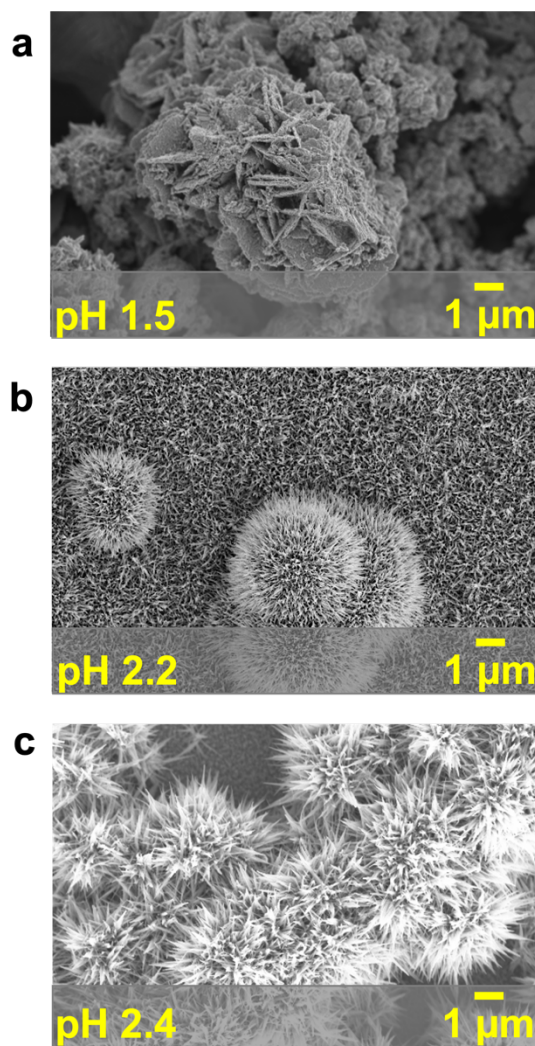


Figure 2.10 SEM images of hydrothermally synthesized  $\text{WO}_3$  nanostructures powders obtained by using precursor solutions with different pH: (a) 1.5, (b) 2.2 and (c) 2.4, after a 2 hours synthesis procedure at  $180^\circ\text{C}$ .

nucleating on the substrates during the synthesis.  $\text{WO}_3$  nuclei formed and grew in solution, and thanks to convective and gravitational motion they rest on the substrate surface without affecting the growth in solution. On the contrary, no  $\text{WO}_3$  nanostructures are deposited on  $\text{SiO}_2$  surface, as shown by Figure 2.11 c. This can be due to the insulator behavior of  $\text{SiO}_2$ , which make very weak bonds between the  $\text{WO}_3$  nanostructures and the substrate. In the case of the ITO substrate, the conductive nature of the latter makes the interactions stronger, by resulting in the nanostructures deposition.

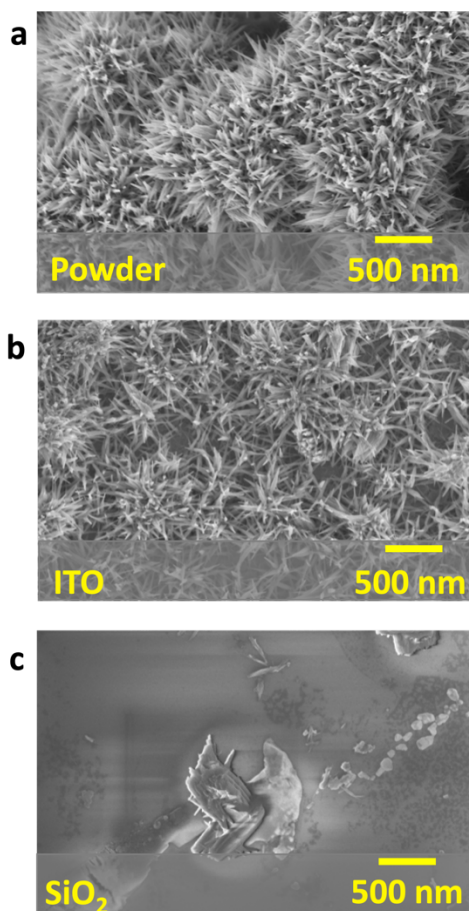
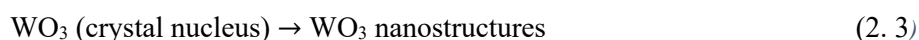
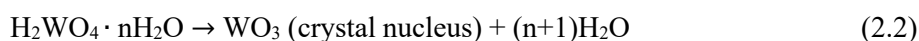
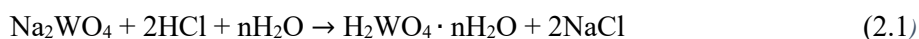


Figure 2.11: SEM images of (a) hydrothermally synthesized  $\text{WO}_3$  nanostructures obtained from a 2.2 pH precursor solution after 3 hours synthesis procedure at 180 °Cent; (b) ITO and (c)  $\text{SiO}_2$  substrates inserted in the autoclave during the same synthesis.



### 2.2.2 Growth mechanism and kinetics

The formation and growth of WO<sub>3</sub> nanostructures during the hydrothermal procedure occur in solution, as the experimental evidence shows, and they can be explained as follows [59]:



According to the chemical reaction (Eq. 2.1), Na<sub>2</sub>WO<sub>4</sub> reacts with the HCl to form the H<sub>2</sub>WO<sub>4</sub> · nH<sub>2</sub>O, which decomposes during the thermal treatment, to produce the WO<sub>3</sub> crystal nucleus (Eq. 2.2), since the solubility of the latter is much lower than the solubility of H<sub>2</sub>WO<sub>4</sub> · nH<sub>2</sub>O [59]. The pH, as well as the HCl content, influences the available amount of H<sub>2</sub>WO<sub>4</sub> · nH<sub>2</sub>O for the WO<sub>3</sub> formation, as demonstrated above, since lower pH leads to a rapid and massive nucleation process (Figure 2.9 a and Figure 2.10 a). The nanostructures growth (Eq. 2.3) depends on the capping agent which interacts in a selective way with the crystal nucleus and leads to a morphology selection (as expected in case of NaCl for the 1D morphology). To track the formation and the growth kinetic mechanism as a function of the annealing time, syntheses starting from the same precursor solution (2.2 pH), but thermally treated with increasing times are performed. Figure 2.12 shows the SEM images of WO<sub>3</sub> powder obtained after 0.5, 1, 2 and 3 hours of thermal treatment (orange, yellow, green, and blue parts respectively) correlated to a timeline. After 0.5 hours (orange part) precipitates were obtained in the form of many irregular nanoparticles, among well not defined agglomerates. These nanoparticles probably will serve as seeds for the nucleation and growth of the WO<sub>3</sub> nanorods, which appear already after 1 hour synthesis (yellow part) though they are well not defined and possess an average dimension of about 200-300 nm. The irregular agglomerates completely disappears after 2 hours (green part), probably because they can be associated to the presence of the H<sub>2</sub>WO<sub>4</sub>

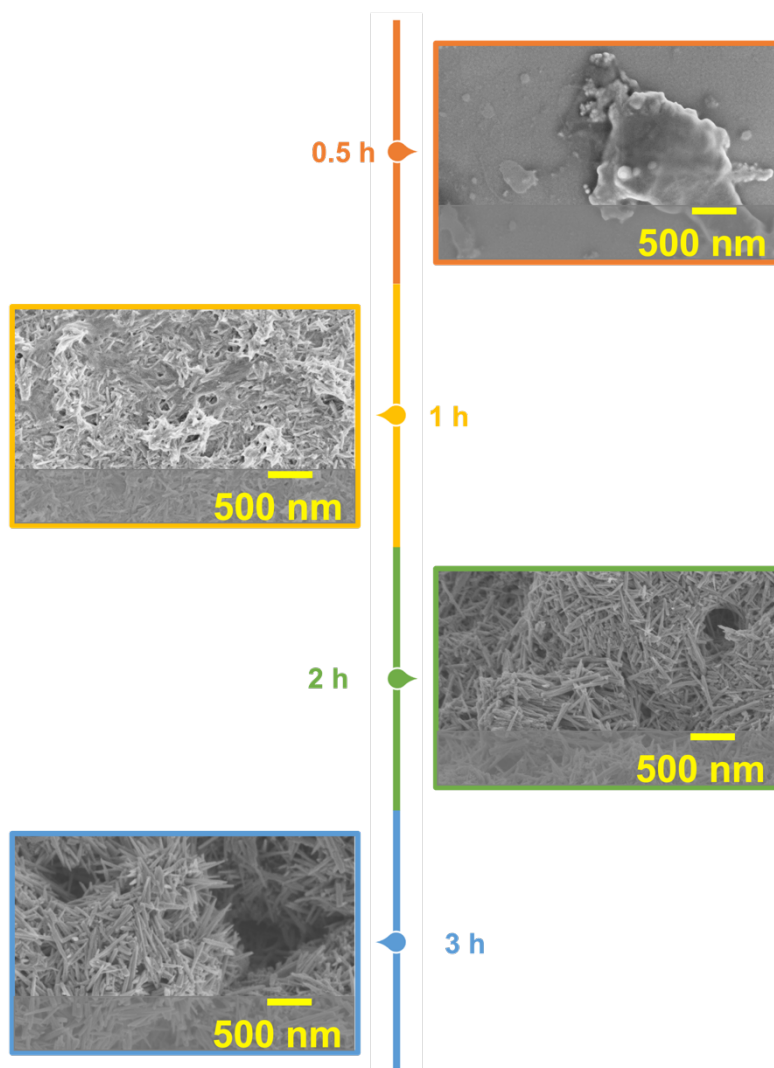


Figure 2.12: Growth kinetic of  $\text{WO}_3$  nanostructures powders, collected after the hydrothermal synthesis with a 2.2 pH precursor solution for different reaction times: after: 0.5 h (orange part), 1 h (yellow part), 2 h (green part) and 3 h (blue part). The progressive formation of well-defined  $\text{WO}_3$  nanorods and urchin-like nanostructures can be appreciated.

which totally decomposes in  $\text{WO}_3$  (Eq. 2.2) and well defined nanorods (400-500 nm) appear [45]. If the annealing growth time is increased up to 3 h (blue part), the anisotropic growth is enhanced thanks to the NaCl as capping agent

and nanorods continue to grow along the *c*-axis, until to reach an average length of 500-600 nm. Urchin-like nanostructures appears only after 3 hours of synthesis, probably due to the agglomeration of different nuclei from which they originated, which slow their growth.

The synthesis of long and well defined nanorods and urchin like nanostructures is a suitable starting point for many applications. To maximize the efficiency of the synthesis and to avoid further energetical consumption in terms of prolonged reaction time and amount of reagents is crucial within a view of green and low cost synthesis. By considering the above experimental results, the optimized synthesis of WO<sub>3</sub> nanostructures was performed by using a 2.2 pH precursor solution thermally treated for 3 hours. To individuate the yield (Y %) of the synthesis, the obtained WO<sub>3</sub> powders were collected, washed, and dried as explained above, and the mass was measured by using a Mettler Toledo MX5 Microbalance (sensitivity: 0.01 mg). The yield (%) of the synthesis is defined by considering the whole process limited by the WO<sub>4</sub><sup>2-</sup> reactant in a 1:1 molar relation between the Na<sub>2</sub>WO<sub>4</sub> and the WO<sub>3</sub>. The ratio between the initial Na<sub>2</sub>WO<sub>4</sub> moles and the final WO<sub>3</sub> moles gives a yield of 10 %.

### 2.3 Characterization of WO<sub>3</sub> nanostructures

The experimental results shown so far allow to identify the better conditions for the synthesis of WO<sub>3</sub> nanostructures. Their characterization will be described in the next paragraphs.

#### 2.3.1 Elemental characterization

Elemental analysis was carried out by performing Rutherford backscattering spectrometry (RBS, 2.0 MeV He<sup>+</sup> beam at normal incidence) with a 165° backscattering angle, and a 3.5 MV HVEE Singletron accelerator (High Voltage Engineering Europa, The Netherlands). A very thin film of WO<sub>3</sub> nanostructures from the optimized synthesis was deposited on a Si substrate by drop casting some drops of a water solution where WO<sub>3</sub> nanostructures were dispersed (1 mg/ml). Figure 2.13 shows the RBS spectrum of the as

prepared sample. The arrows indicate energy of He ions backscattered by W(1836 MeV), Si (1138 MeV), or O (731.8 keV) atoms on the surface of the analyzed film. The height of the peaks is strongly related to the cross-section of the interaction between the He<sup>+</sup> ions and the nucleus of the present atoms, which is directly proportional to the atomic number. W atom possesses a higher atomic number than O atom, whereby the height of the W peak is higher than the height of O peak [66]. The area of W peak gives information about the W dose, as well as the area under the O peak (after proper background subtraction). The obtained doses are about  $24 \cdot 10^{16}$  at/cm<sup>2</sup>, and  $8 \cdot 10^{16}$  at/cm<sup>2</sup> for O and W respectively, by confirming a W:O stoichiometry of 1:3. No signals from contaminations appear, by suggesting that the concentrations of the latter are below the detection limit and can be considered negligible.

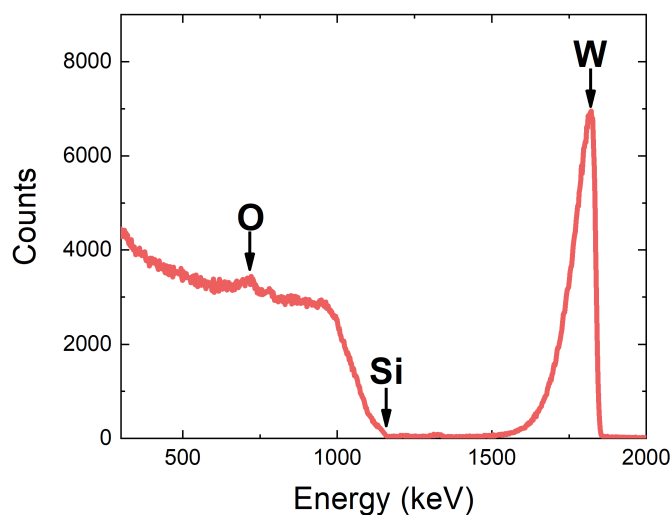


Figure 2.13: RBS spectrum of the WO<sub>3</sub> nanorods and urchin-like nanostructures deposited on a Si substrate, in which the signals of O, Si, and W are present as expected.

### 2.3.2 Morphological and structural characterization

An in-depth morphological analysis was carried out to better describe the nanostructures. Figure 2.14 shows (a) low and (b-c) high magnification SEM images of WO<sub>3</sub> powder from the optimized synthesis. Urchin-like agglomerates are stacked on top of a thick oddly aligned WO<sub>3</sub> nanorods film (Figure 2.14 a), by suggesting a contemporary growth of these nanostructures, as mentioned before.

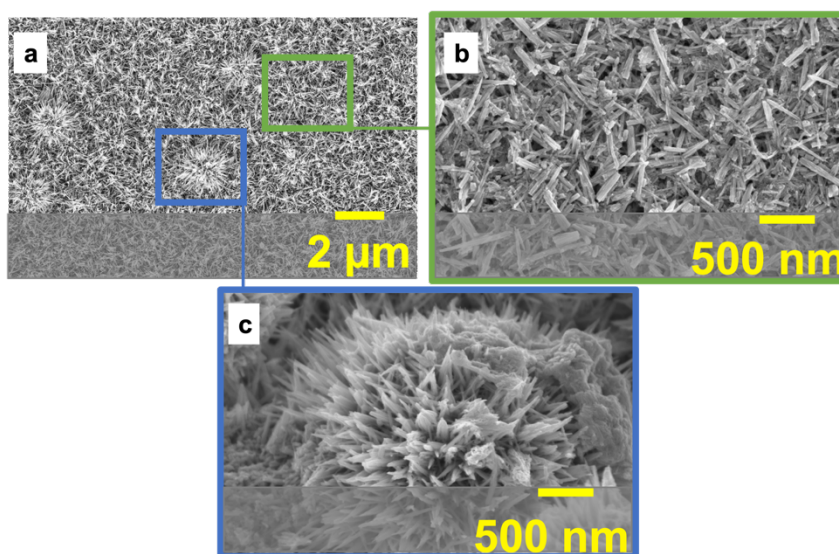


Figure 2.14: (a) Low and (b-c) high SEM images of WO<sub>3</sub> nanostructures (nanorods and urchin-like morphology respectively) obtained by following the optimized process, starting from a 2.2 pH precursor solution, thermally treated for 3 h. Reproduced by [67].

The crystalline nature of these WO<sub>3</sub> nanostructures was analyzed by X-ray Diffraction (XRD) measurements with a Smartlab Rigaku diffractometer, in grazing incidence 0.5°, equipped with a rotating anode of Cu K $\alpha$  radiation operating at 45 kV and 200 mA. The scans were acquired from 10° to 70° with the hexagonal phase (Figure 2.15 c, black lines, PDF #89-4476) can be observed, but they are not well defined thus suggesting a poor crystallinity nature of WO<sub>3</sub>\_AsPrep [67]. Moreover, the bump at around  $2\theta = 20.00^\circ$  can

be associated with an unknown nonstoichiometric phase [68]. To improve the crystalline quality, a post growth thermal treatment at 70 °C for 40 min in air was carried out (the obtained powder was denoted as WO<sub>3</sub>\_A70). Figure 2.15 (b) shows XRD pattern of WO<sub>3</sub>\_A70 (blue line) and well-defined typical hexagonal peaks appear at  $2\theta = 14.00^\circ$ ,  $24.36^\circ$ ,  $26.84^\circ$ ,  $28.22^\circ$ ,  $33.62^\circ$ ,  $36.58^\circ$ , and  $49.95^\circ$ , thus confirming the good crystal quality of the latter [64].

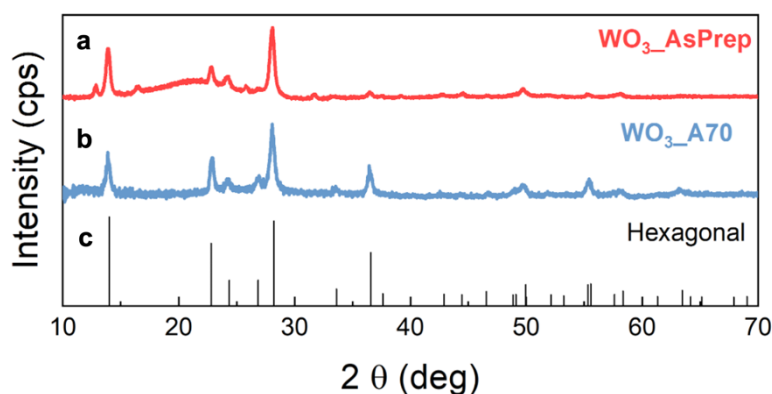


Figure 2.15: XRD pattern of (a) WO<sub>3</sub> nanostructures (WO<sub>3</sub>\_AsPrep), (b) WO<sub>3</sub> nanostructures annealed at 70°C for 40 min (WO<sub>3</sub>\_A70), and (c) hexagonal WO<sub>3</sub> (PDF #89-4476). Reproduced by [67].

Scanning TEM analyses (STEM) were performed by using a transmission electron microscope (TEM) JEOL, JEM-ARM200F operated in TEM mode, to investigate morphology and crystal structure of single urchin-like nanostructure (Figure 2.16 a-c) and nanorod (Figure 2.16 d) from WO<sub>3</sub>\_A70 powder<sup>1</sup>. Figure 2.16 (a-c) show a single urchin-like agglomerate and a portion thereof at increasing magnifications, by confirming that it is composed of a bundle of nanorods. Figure 2.16 (d) shows a STEM image which reveals that each nanorod is composed of a bundle of very thin nanoneedles with a section around 10 nm, that are well aligned with each other along the c-axis, as shown by the Fast Fourier Transform (FFT) on the inset of Figure 2.16 (d). Figure 2.16 (e) shows the high-resolution STEM image of an enlarged view of a WO<sub>3</sub> nanoneedle, thus confirming the hexagonal structure of the crystal

<sup>1</sup> These analyses were carried out in collaboration with Dr. Mario Scuderi at CNR-IMM Institute of Catania (Italy).

lattice. In this figure, the brighter and darker spots corresponds to atomic columns with a bigger and lower effective atomic mass respectively, which can be associated to the presence of two tungsten and one oxygen atoms per unit cell in the first case and to atomic column with one tungsten atom for unit cell in the latter case, as shown by the dark-field (DF) intensity line scan and by the 3D atomic model of WO<sub>3</sub> hexagonal unit cell in Figure 2.16 (f).

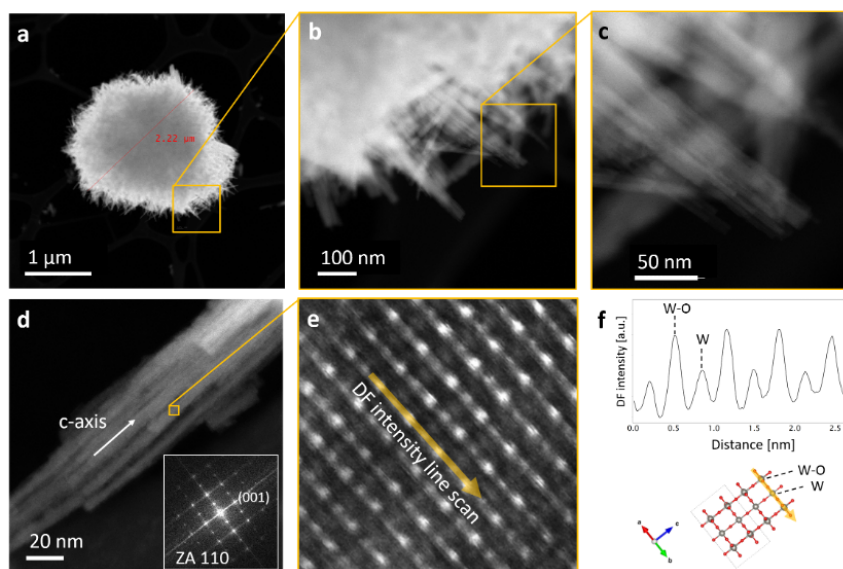


Figure 2.16: STEM Z-contrast micrographs of (a-c) a single urchin-like nanostructures at increasing magnification and (d) a single nanorod, which appears composed of aligned nanoneedles; (e) enlarged view of the atomic lattice of a WO<sub>3</sub> nanoneedle (f) DF intensity line scan of (e) and 3-D atomic model of the WO<sub>3</sub> hexagonal unit cell. Inset of (d): FFT of (f) [67].

These results show that the optimized hydrothermal synthesis (2.2 pH and 3 h thermal treatment) coupled with a post-synthesis annealing at 70°C for 40 min provides hexagonal WO<sub>3</sub> needles stuck together to build nanorods and, hierarchically, urchin-like structures.

### 2.3.3 Optical characterization

Optical behavior of WO<sub>3</sub> nanorods and urchin-like nanostructures was analyzed by using an UV-VIS-NIR spectrophotometer Varian Cary 500.

Some drops of water solutions containing WO<sub>3</sub>\_AsPrep and WO<sub>3</sub>\_A70 powders (4 mg/ml) were drop casted on corning glass to perform transmittance (%T) and reflectance (%R) analyses for the determination of the absorbance (%A) as follows [69]:

$$\%A = 1 - \%T - \%R$$

Figure 2.17 shows (a) the absorbance spectra of WO<sub>3</sub>\_AsPrep and WO<sub>3</sub>\_A70 (red and blue line respectively) and (b) the related Tauc plot (solid line) which allows to define the optical energy band gap ( $E_{\text{gap}}$ ), by considering an indirect allowed transition [69]. The energy band gap is defined from the x-intercept of the fit of the linear region of the Tauc Plot (dotted line in Figure 2.17 b). The results of such exercise give  $E_{\text{gap}}$  of 1.5 and 2.6 eV for WO<sub>3</sub>\_AsPrep and WO<sub>3</sub>\_A70 respectively. The relatively low  $E_{\text{gap}}$  value for the WO<sub>3</sub>\_AsPrep powder can be ascribed to the presence of a nonstoichiometric phase, as well as the presence of oxygen vacancy suggested by XRD pattern of Figure 2.15 (a). This leads to the formation of a defect level inside the band gap, which can act as trapping level for the electrons, thus lowering the optical  $E_{\text{gap}}$  [1]. Indeed, the  $E_{\text{gap}}$  of the WO<sub>3</sub>\_A70 powder is typical of a hexagonal structure, by further confirming the good crystallinity nature of these nanostructures [2].

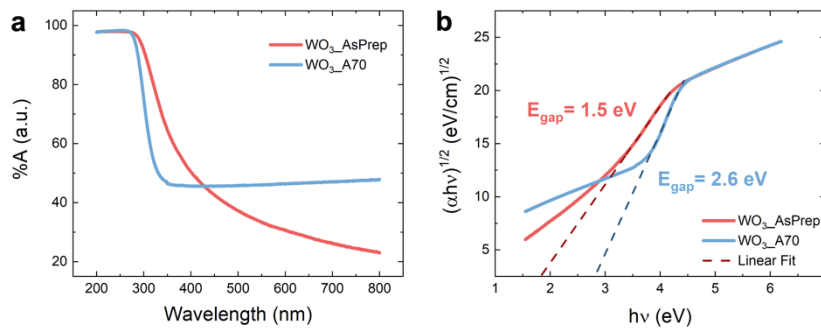


Figure 2.17: (a) Absorbance spectra and (b) Tauc plots and their relative linear fits (dotted lines) of the WO<sub>3</sub>\_AsPrep and WO<sub>3</sub>\_A70 powders (red and blue line respectively). The energy gaps are defined as the x-intercept of the linear fit.



### 2.4 Conclusion

In this chapter the hydrothermal synthesis of WO<sub>3</sub> nanostructures is described in detail. The experimental results show the possibility to control the morphology, the dimension, the crystal structure, and the stoichiometry by simply changing the synthesis parameters, e.g., the capping agent, the pH, and the annealing time. Among the nanostructured morphologies, nanorods seems to be the best for catalytic activity in which the interaction with small ions (such as H<sup>+</sup>) is expected, thanks to their 1D structure, their high exposed surface, and the presence of empty channel in the matrix which promote the intercalation. The growth kinetic of WO<sub>3</sub> nanorods is studied as a function of the annealing time, as well as the crystal structure dependence on the post-synthesis thermal treatment. The optimized synthesis (2.2 pH, growth at 180 °C for 3 hours, followed by an annealing at 70 °C for 40 min in air) allows to produce hexagonal WO<sub>3</sub> needles stuck together to build nanorods and, hierarchically, urchin-like structures, suitable for many applications, such as H<sub>2</sub> sensing, production, and storage.



# Chapter 3

## WO<sub>3</sub> nanorods for gas sensing

*WO<sub>3</sub> nanostructures are promising materials for the realization of fast and reliable gas sensors for environmental monitoring, through the chemoresistive effect, thanks to the high-stability and low cost of WO<sub>3</sub> based targets. Among all gases, a particular attention is devoted to H<sub>2</sub> and NO. H<sub>2</sub> is explosive if the concentration is higher than 4%, while NO is a common air pollutant. A comprehensive description of the interaction between H<sub>2</sub> and WO<sub>3</sub> is still missing in literature, as well as the interaction with the NO. In this chapter, the realization of WO<sub>3</sub> nanorods-based sensors is described. Both H<sub>2</sub> and NO sensing tests were performed at different temperatures (250-400 °C) and under different gas concentrations (2000-50000 ppm and 250-2500 ppm, respectively)*

*The H<sub>2</sub> sensing mechanism is successfully modeled in terms of surface and bulk processes by using the Langmuir adsorption theory. The comprehensive description of the H<sub>2</sub> sensing mechanism will allow to optimize the sensor fabrication to maximize the sensitivity and selectivity towards H<sub>2</sub>, thus opening the route to the development of fast, sensitive, and low-temperature operating H<sub>2</sub> sensors based on WO<sub>3</sub>.*

*NO response and recovery curves are also modeled by using the Langmuir adsorption theory. The results of this exercise show a preliminary analysis of the NO sensing mechanism by WO<sub>3</sub> nanorods. The interaction occurs between NO and the adsorbed oxygen ions on the surface of the WO<sub>3</sub> nanorods, the high responses at low temperatures and the low response and recovery times open the route for the development of low-temperature and fast NO sensors based on WO<sub>3</sub>.*

### 3.1 The role of gas sensor

The development of always emerging technologies resulted in the increasing of emission of harmful and toxic gases in atmosphere. Figure 3.1 shows the most common pollutants released in atmosphere, which are volatile organic compounds (VOCs), carbon monoxide (CO), nitrogen oxide (NO<sub>x</sub>), ammonia (NH<sub>3</sub>) and many others produced by factories and vehicles as an example. The presence of these pollutants can cause serious health problems if presents above a certain concentration, such as lung cancer or cystic fibrosis. It is hence necessary to constantly monitor the concentration of these gases, so the development of fast and ultra-sensitive gas sensor is highly demanded [70].

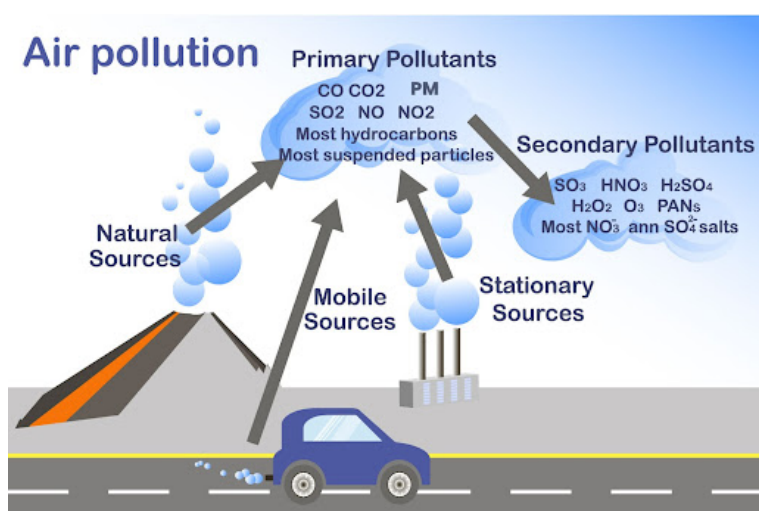


Figure 3.1: Schematic illustration of air pollutants and their sources [71]

There are a variety of gas sensors, depending on the physical parameters used to monitor the presence of target gases. In chemoresistive gas sensors (Figure 3.2) the chemical interaction between the target gas and the active element produces an electrical resistance variation whose intensity is strictly correlated to the amount of the target gas itself. Metal oxide semiconductors represent suitable candidates for the development of fast and reliable chemoresistive gas sensor, thanks to their low cost and high affinity to reducing and oxidizing gases. One of the most promising materials for the gas sensing is WO<sub>3</sub> which

is a *n*-type semiconductor with an indirect bandgap ranging between 2.6-3.2 eV [2]. The high chemical and thermal stability make it a suitable candidate for the sensing of many pollutant gases such as H<sub>2</sub>S, NH<sub>3</sub>, NO<sub>2</sub>, and H<sub>2</sub> [72-75]. Chemical interaction between WO<sub>3</sub> and target gases leads to a chemical resistance variation measurable directly during the sensing process. The possibility of tuning the catalytic gas sensing activity with the aim of the nanotechnology is the key parameter for the development of fast and reliable gas sensors, since Nanostructured metal oxide semiconductors show better performances thanks to a larger surface-to-volume ratio, higher specific surface area, and crystal faceting with marked surface reactivity [76-77].

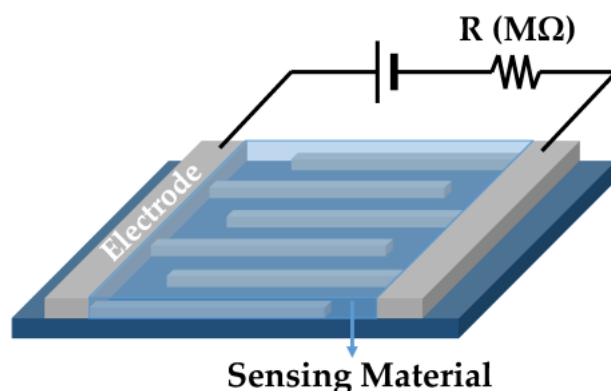


Figure 3.2: : Schematic of a chemoresistive gas sensor, in which the gas response depends on the resistance variation [78].

Nowadays, the research on WO<sub>3</sub> nanostructures as gas sensor is focused on the development of highly selective, stable, and sensitive devices, but a comprehensive understanding of the microscopic sensing mechanism of the various gases is still missing. Univocal experimental evidence of chemical reactions or precise determination of energy barriers do not result from literature and a detailed description of temperature-activated kinetics is however required.

### 3.2 Electrode realization and characterization

WO<sub>3</sub> nanostructures were synthesized by following the optimized procedure described in Chapter 2. For the electrode realization, WO<sub>3</sub> nanorods powder is

dissolved in 5 ml (4 mg/ml) of deionized water and sonicated for 20 minutes. Several drops are then dipped on a conductometric gas sensor (Inset Figure 3.3) consisting in an alumina substrate (6x3 mm<sup>2</sup>) with a Pt heater on backside and Pt interdigitated electrodes on the front-side.

The morphological analyses were carried out by a scanning electron microscope (SEM) Gemini Field Emission SEM Carl Zeiss SUPRATM 25 (FEG-SEM, Carl Zeiss Microscopy GmbH, Jena, Germany). X-ray diffraction (XRD) patterns were acquired through a Bruker-AXSD5005θ-θ diffractometer, using a Göbel mirror to parallel the Cu K $\alpha$  radiation operating at 40 kV and 30 mA. The transmittance spectra were obtained by using a UV-VIS-NIR spectrophotometer Varian Cary 500.

Gas sensing measurements were performed in a stainless-steel test chamber which allowed measurements in a controlled atmosphere<sup>2</sup>. Gases coming from certified bottles were used and diluted in synthetic dry air at a given concentration by using mass flow controllers. The sensor was heated from room temperature (~20 °C) up to 400 °C under a dry air (RH < 3 %) total stream of 100 sccm by using a dual-channel power supplier instrument Agilent E3632A to bias the built-in heater. The response to different gases was evaluated by recording the resistance at an applied voltage of 1.0 V through a Keithley 6487 picometer with a time step of about 2.5 s. Figure 3.3 shows the measurement workbench employed for the sensing characterization.

Low and high (inset) magnification SEM images of obtained powder on interdigitated electrode are shown in Figure 3.4 (a), confirming the nanorods morphology with an average length and diameter of 400 and 50 nm, respectively. All interdigitated fingers were covered to maximize the response during gas sensing measurements. The XRD pattern is shown in Figure 3.4 (b), where all hexagonal WO<sub>3</sub> diffraction peaks are present, which appear at  $2\Theta = 14.00^\circ, 24.36^\circ, 26.84^\circ, 28.22^\circ, 33.62^\circ, 36.58^\circ, \text{ and } 49.95^\circ$ , thus confirming the hexagonal structure of WO<sub>3</sub> nanorods, as expected. The electrical resistance  $R$  in dry air at different temperatures  $T$  was investigated (Figure 3.4 c). By increasing the temperature from 250 to 400 °C, the electrical

---

<sup>2</sup> The analysis were carried out in collaboration with the Professor Giovanni Neri of the University of Messina, Italy

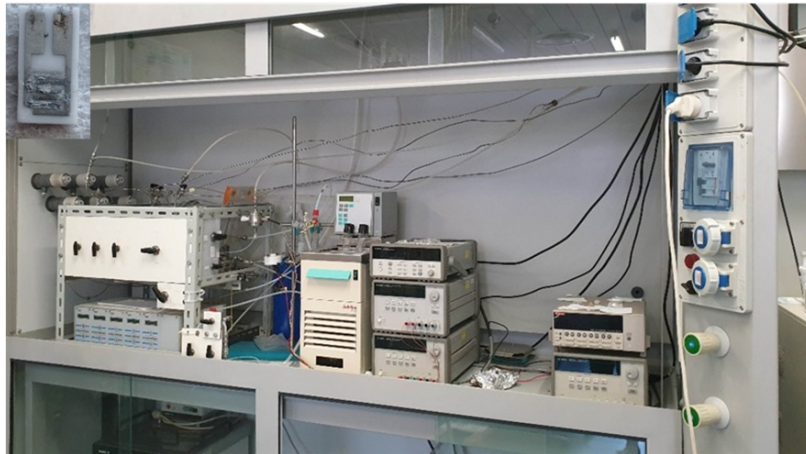


Figure 3.3: Measurement apparatus used during the gas sensing characterization of sample. Inset: photograph of the conductometric sensor.

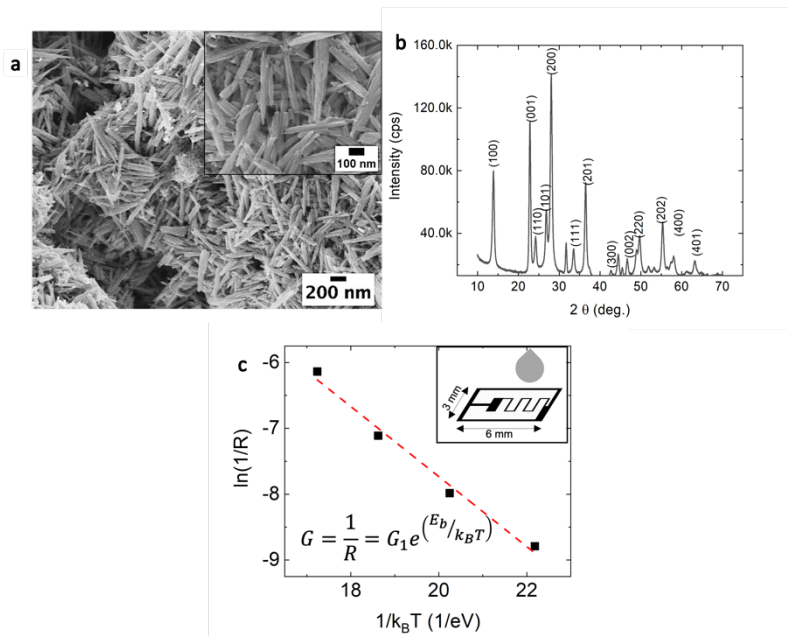


Figure 3.4: (a) low and (inset) high magnification SEM image of WO<sub>3</sub> nanorods deposited on the interdigitated substrate, (b) XRD pattern, and (c) Arrhenius plot of inverse of measured resistance ( $R$ ); inset in (c): schematic of interdigitated substrate drop coated [64].

conductance  $G (=I/R)$  of WO<sub>3</sub> nanorods increases by almost three orders of magnitude, following an exponential behavior with an activation energy  $E_b$  of 0.53 eV. In an  $n$ -type semiconductor, as the WO<sub>3</sub>, the conductivity depends on electron concentration in conduction band and on electron mobility. Disregarding the thermal dependence of electron mobility, the measured activation energy for conductance could account for the energy position (0.53 eV) below the conduction band of the intrinsic donor-like defects of undoped WO<sub>3</sub>, in agreement with Kalanu et al. [79].

To preliminarily test the WO<sub>3</sub> sensor selectivity, it was exposed to pulses of different gases (10000 ppm of H<sub>2</sub>, 500 ppm of NO and 50 ppm of CO) at temperatures ranging between 250 and 400 °C, as Figure 3.5 (a) shows. The H<sub>2</sub> response is higher than the NO response, especially at higher temperatures, while no response is obtained for CO whatever the temperature is, confirming a certain selectivity of the WO<sub>3</sub> sensor towards H<sub>2</sub> and NO. Figure 3.5 (b) shows the measured resistance variation at 300 °C after the H<sub>2</sub>, NO, and CO flux in the test chamber. In the next paragraph the sensing toward H<sub>2</sub> and NO will be detailed separately.

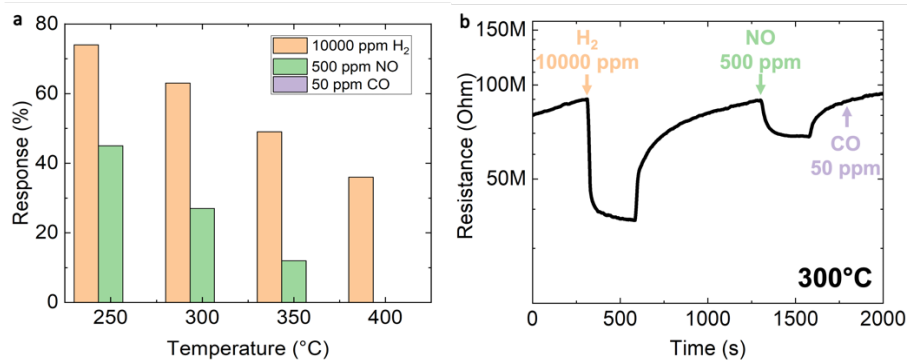


Figure 3.5: (a) Selectivity as a function of tested temperature of WO<sub>3</sub> sensor towards different gases: 10000 ppm of H<sub>2</sub> (orange column), 500 ppm of NO (green column) and 50 ppm of CO (violet column); (b) measured resistance variation as a function of time at 300°C under a mixture of dry synthetic air and 10000 ppm of H<sub>2</sub> (orange label), 500 ppm of NO (green label) and 50 ppm of CO (violet label) of WO<sub>3</sub> based sensor [64].



### 3.3 H<sub>2</sub> sensing by WO<sub>3</sub> nanorods

#### 3.3.1 State of the art

In recent years the scientific community has devoted a large interest to hydrogen as a source of energy, since it is an excellent candidate to replace fossil fuels for many applications, such as chemical industry, power generation, medical treatment, and many others [80-82]. Soon, hydrogen production, transportation, and storage will become key issues for sustainable development. However, H<sub>2</sub> is a colorless, tasteless, and odorless gas which becomes inflammable and explosive when its concentration exceeds 4%. Therefore, fast, and very sensitive sensors are necessary where H<sub>2</sub> is produced, stored, and transported to promptly detect any leakage. Typically, fast H<sub>2</sub> sensors work at high temperatures (250-400 °C), increasing the explosion risk [83,84]. The progress in H<sub>2</sub> application cannot proceed without a parallel development of safe, fast, and reliable H<sub>2</sub> sensors. To this aim, a proper investigation is needed to unveil the interaction between H<sub>2</sub> and the sensing material leading to reliable detection.

The affinity of WO<sub>3</sub> versus reducing gases makes it an excellent candidate for optical and chemoresistive H<sub>2</sub> sensor realization since low concentrations can be detected, also below 250°C. Zhang et al. [75] synthesized urchin-like hexagonal WO<sub>3</sub> and tested them at 250 °C for H<sub>2</sub> sensing at concentrations ranging between 10 and 80 ppm. Wu et al. [85] synthesized Pd loaded mesoporous WO<sub>3</sub> for H<sub>2</sub> sensing test. They compared bare WO<sub>3</sub>, mesoporous WO<sub>3</sub>, and Pd-loaded mesoporous WO<sub>3</sub>, showing that the latter is the best one in terms of response efficiency at room temperature at 5000 ppm of H<sub>2</sub>. Chang et al. [86] studied the gas sensing performances of Pt-loaded WO<sub>3</sub> thin-film at 200 °C under different concentrations of H<sub>2</sub> (between 1 and 10000 ppm). Mattoni et al. [87] synthesized a single-crystal Pt-decorated WO<sub>3</sub> thin film and tested it at room temperature under sub-ppm concentration of hydrogen.

Using a density functional theory approach, Tian et al. [88] proposed a model for the interaction between H<sub>2</sub> and hexagonal WO<sub>3</sub>, according to which the H<sub>2</sub> sensing mechanism proceeds through H<sub>2</sub>O molecules formation after

interaction of H<sub>2</sub> with oxygen ions adsorbed onto noble metal nanoparticles. Experimental works by Wu and Chang claimed Tian's model. On the other hand, Mattoni et al. proposed a different model based on adsorption of H<sub>2</sub> on Pt nanoparticles, H<sub>2</sub> dissociation and intercalation of H<sup>+</sup> ions inside the lattice of WO<sub>3</sub>. A comprehensive understanding of WO<sub>3</sub>-H<sub>2</sub> interaction is still missing, univocal experimental evidence of chemical reactions or energy barriers evaluation do not result from literature and a detailed description of temperature-activated kinetics is however required. A basic comprehension of actual processes underlying the WO<sub>3</sub>-H<sub>2</sub> interaction could promote a step forward in H<sub>2</sub> sensing by WO<sub>3</sub>.

### 3.3.2 H<sub>2</sub> sensing performances measurements

WO<sub>3</sub> nanorods deposited on the interdigitated electrode were applied for H<sub>2</sub> sensing. Experimental H<sub>2</sub> sensing curves were obtained by measuring resistance variations as a function of time while a mixture of H<sub>2</sub> and dry air (response phase) or dry air only (recovery phase) are fluxed in the chamber. To investigate the WO<sub>3</sub>-H<sub>2</sub> interaction, we tested different concentrations (2000-50000 ppm) and different temperatures (250-400 °C). Figure 3.6 shows resistance variations (black curve) at 350 °C under different H<sub>2</sub> concentrations (red curve), confirming a strong dependence of resistance on H<sub>2</sub> concentration. Resistance decreases when H<sub>2</sub> is fluxed in the test chamber (gas in arrow), while increases when H<sub>2</sub> flux is stopped (gas out arrow).

From experimental curves of resistance variation, a sensor response  $S$  (%) can be defined. Since WO<sub>3</sub> is an *n-type* semiconductor and H<sub>2</sub> is a reducing gas,  $S$  (%) is determined as follows:

$$S(\%) = (R_a - R_g)/R_a * 100 \quad (3.1)$$

in which  $R_g$  and  $R_a$  are the measured resistances in presence and absence of H<sub>2</sub> gas, respectively. To understand WO<sub>3</sub>-H<sub>2</sub> interaction,  $S$  (%) is defined for each tested temperature and concentration. Figure 3.7 shows sensor response curves obtained at each temperature (250-400 °C) as a function of elapsed time during the “response” (pink background in panel b) and “recovery”

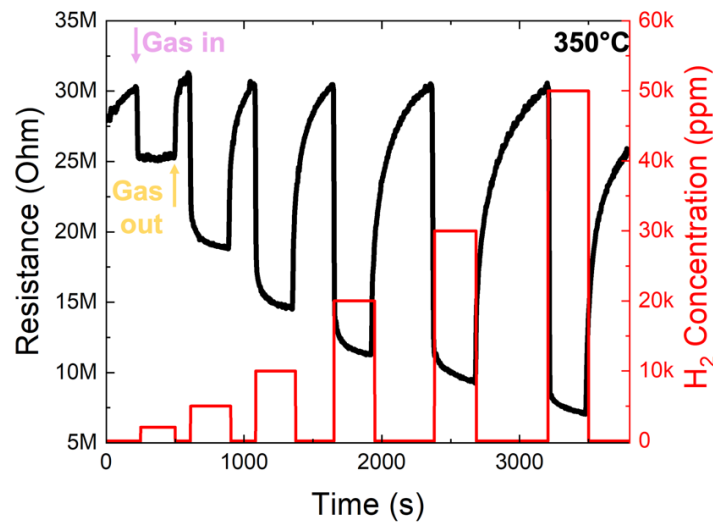


Figure 3.6: Dynamic resistance variation of WO<sub>3</sub>-based sensor (black curve) at 350°C under different H<sub>2</sub> concentrations (red curve). Arrows indicate when H<sub>2</sub> is fluxed in the chamber (named “gas in”) or it is stopped (named “gas out”) [64].

(yellow background in the panel b) phase, respectively. In each case of Figure 3.7, the response curve increases rapidly when H<sub>2</sub> is fluxed into the chamber, while tends to saturate after about 20 s. When H<sub>2</sub> flux is stopped, the recovery mechanism starts, and the curves decrease in a temperature dependent way. H<sub>2</sub> concentration tests were carried out at 350 °C and Figure 3.8 shows response and recovery curves obtained under (a) 2000 ppm, (b) 5000 ppm, (c) 10000 ppm, (d) 20000 ppm, (e) 30000 ppm, and (f) 50000 ppm fluxes of H<sub>2</sub>. Response curves increase rapidly when H<sub>2</sub> gas is fluxed in chamber. After about 20 s the curves tend to saturation and when H<sub>2</sub> flux is stopped the recovery mechanism starts, with the curves decreasing rapidly at first but then slowly tending to the initial value.

### 3.4 H<sub>2</sub>-WO<sub>3</sub> interaction mechanism

The analysis of the experimental curves is crucial to understand the mechanisms which describe the H<sub>2</sub>-WO<sub>3</sub> interaction. In the next paragraph,

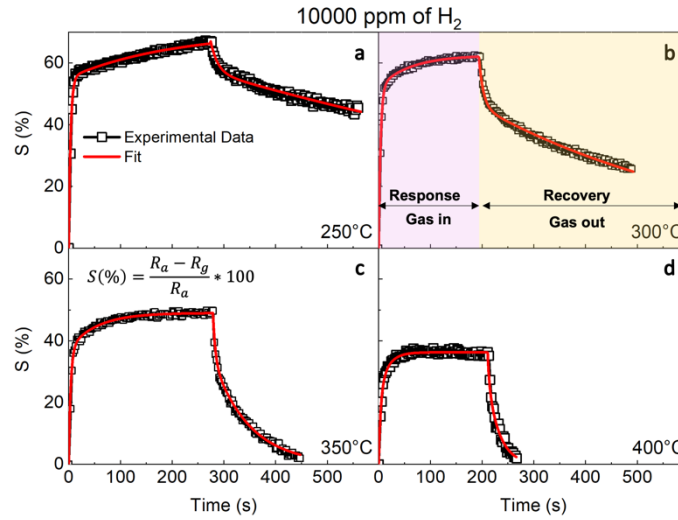


Figure 3.7: Dynamic responses of WO<sub>3</sub>-based sensor (squared symbols) and fit (red lines) obtained at (a) 250 °C, (b) 300 °C, (c) 350 °C, and (d) 400 °C under 10000 ppm of H<sub>2</sub> as a function of elapsed time starting when H<sub>2</sub> is fluxed in chamber [64].

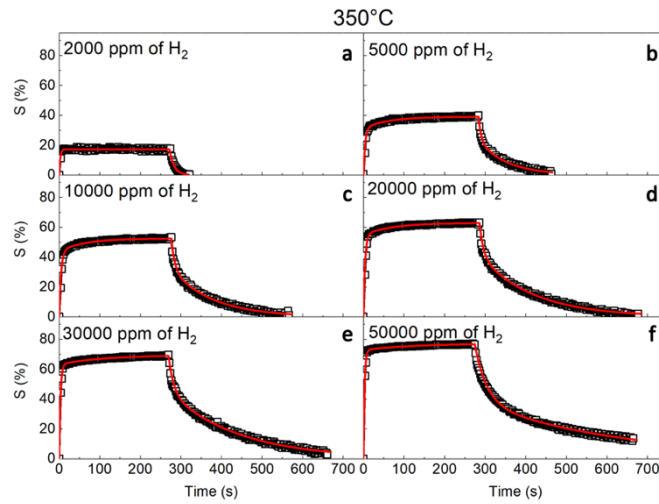


Figure 3.8: Dynamic responses of WO<sub>3</sub>-based sensor (squared symbols) and fit (red lines) obtained at 350 °C under (a) 2000 ppm, (b) 5000 ppm, (c) 10000 ppm, (d) 20000 ppm, (e) 30000 ppm and (f) 50000 ppm fluxes of H<sub>2</sub> as a function of elapsed time [64].

the response and recovery curves were modeled, to define the active processes during the response and the recovery phase.

### 3.4.1 Simulation of experimental curves

To determine the kinetics of the H<sub>2</sub> sensing, all experimental response curves were fitted by considering the Langmuir absorption theory with two isotherms (two processes are assumed to play independent roles). According to Langmuir, sensor response during the “gas in” phase,  $S$ , and during the “gas out” phase,  $S^*$ , can be fitted as follows [89]:

$$S = S_0\{w[1 - \exp(-t/\tau_1)] + (1 - w)[1 - \exp(-t/\tau_2)]\} \quad (3.2)$$

$$S^* = S_0[w^* * \exp(-t/\tau_1^*) + (1 - w^*) * \exp(-t/\tau_2^*)] \quad (3.3)$$

in which  $S_0$  is the maximum value of resistance change (the same value was fixed for response and recovery phases),  $\tau_n$  and  $\tau_n^*$  (n stands for 1 or 2) are lifetimes associated to the two isotherms during response and recovery phases, respectively;  $w$  and  $w^*$  are weights attributed to process 1 during response and recovery phases, respectively.

The fitting curves (red lines) shown in Figure 3.7 are in excellent agreement with experimental data (black squares), supporting the hypothesis of a fast (P1) and a slow (P2) process, independent and concomitant.

The fitting parameters are listed in Table 3.1 as a function of tested temperature. The maximum response value ( $S_0$ ) changes with temperature: it is maximum (70%) at 250 °C, as expected given the very high resistance at this temperature. Lifetimes and weights are reported in Figure 3.9 (a-b) as a function of temperature. P1 is characterized by times of few seconds (roughly the time resolution of experimental set-up), both in response and in recovery phases and regardless of temperature, while P2 is characterized by long times (10-200 s) in response and (20-1100 s) in recovery phases. In both cases,  $\tau_2$  and  $\tau_2^*$  are clearly dependent on temperature since they decrease when temperature increases. Concerning the weight,  $w$ , P1 is predominant ( $w$  around 60-84%) during the response phase while it is minority during the recovery

Temperature (°C)	S <sub>0</sub> (%)	τ <sub>1</sub> (s)	τ <sub>2</sub> (s)	w (%)	τ* <sub>1</sub> (s)	τ* <sub>2</sub> (s)	w*
250	70.1±0.8	3.6±0.2	200±21	79±1	14±1	1137±030	15±1
300	62.5±0.3	3.8±0.2	61±6	83±1	8.5±0.5	483±3	29±1
350	49.0±0.1	3.8±0.2	54±3	76±1	5±1	71±1	32±4
400	36.3±0.1	3.9±0.9	16±2	60±10	3±1	23±2	25±10

Table 3.1: Results of the fitting procedure to response and recovery transients at various temperatures and at fixed concentration of H<sub>2</sub> (10000 ppm) [64]

phase. Such a result could suggest different mechanisms occurring during response and recovery phases.

An analogous analysis was performed when tests were carried out at fixed temperature by varying H<sub>2</sub> concentration. For all these cases shown in Figure 3.8, except at 2000 ppm, Eqs. (3.2) and (3.3) can be used to fit experimental curves by obtaining good agreement. In the case of the lowest concentration (Figure 3.8 a) only one process (P1) is identified both during the response and the recovery phase, and so,  $w$  is maximum.

Table 3.2 reports all parameters obtained from fitted curves of Figure 3.8. The maximum response values depend on concentration since the highest value (77%) is obtained at a higher concentration (50000 ppm). Moreover, lifetimes and weights are reported in Figure 3.9 (c-d) as a function of H<sub>2</sub> concentration. Both in response and recovery phases, P1 is characterized by short lifetimes, regardless of concentration, while P2 has increasing lifetimes with increasing concentration. P1 is predominant in the response phase since  $w$  is around 80-95%, but not during the recovery phase. Also, in this case, this can be due to different mechanisms occurring during response and recovery phases.

Figure 3.9 (c) shows the  $w$  trend as a function of H<sub>2</sub> concentration in cases where two processes are identified, revealing an exponentially increasing trend up to saturation. It should be noted that, within the Langmuir theory, the surface coverage  $\theta_m$  by the adsorbed gas molecules [90] is expected to increase similarly. This evidence suggests that process P1 is related to a surface coverage by H<sub>2</sub>. The Langmuir adsorption model with two isotherms

Concentration ( $\cdot 10^3$ ppm)	$S_0$ (%)	$\tau_1$ (s)	$\tau_2$ (s)	w (%)	$\tau_1^*$ (s)	$\tau_2^*$ (s)	w <sup>*</sup> (%)
2	17.2 $\pm$ 0.1	2.6 $\pm$ 0.4	--	100	11.3 $\pm$ 0.7	--	100
5	39.1 $\pm$ 0.1	4.2 $\pm$ 0.2	63 $\pm$ 5	80 $\pm$ 1	6.3 $\pm$ 0.7	71 $\pm$ 2	42 $\pm$ 1
10	52.5 $\pm$ 0.1	4.6 $\pm$ 0.2	65 $\pm$ 4	84 $\pm$ 1	8.2 $\pm$ 0.6	102 $\pm$ 2	40 $\pm$ 1
20	62.9 $\pm$ 0.1	3.9 $\pm$ 0.1	70 $\pm$ 4	87 $\pm$ 1	9.5 $\pm$ 0.7	132 $\pm$ 2	34 $\pm$ 1
30	69.4 $\pm$ 0.2	3.1 $\pm$ 0.1	111 $\pm$ 9	91 $\pm$ 1	12.4 $\pm$ 0.6	174 $\pm$ 2	36 $\pm$ 1
50	77.2 $\pm$ 0.2	2.7 $\pm$ 0.1	126 $\pm$ 14	94 $\pm$ 1	28.9 $\pm$ 0.7	359 $\pm$ 7	50 $\pm$ 1

Table 3.2: Results of the fitting procedure to response and recovery transients at various concentration of H<sub>2</sub> at temperature of 350°C [64].

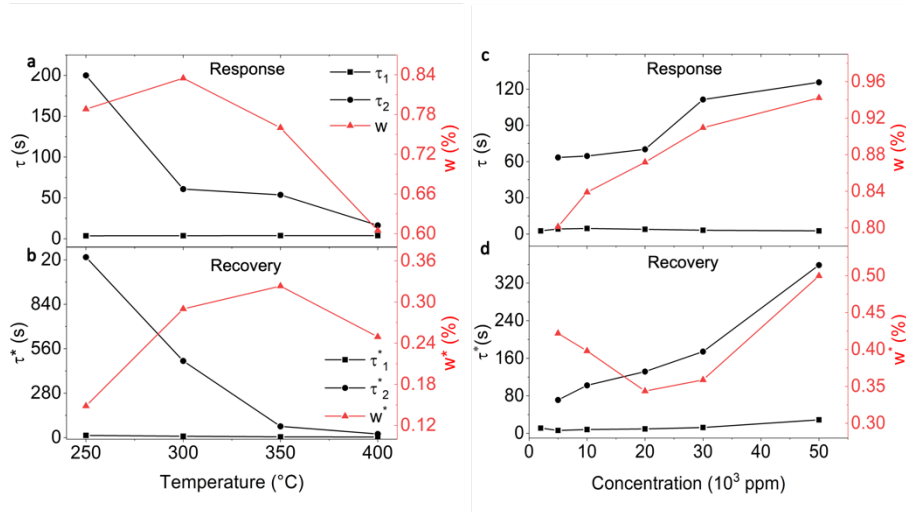


Figure 3.9: Dependence of the fit parameters by tested (a-b) temperature and (c-d) concentration obtained during (a, c) response and (b, d) recovery mechanism. The legend is the same for (a) and (c), and for (b) and (d) [64].

describes our experimental data very well, pointing out that the WO<sub>3</sub>-H<sub>2</sub> interaction proceeds through at least two ways. Indeed, the thermal dependence of  $\tau$  is highly significant as it will unveil the energy barrier for concurring processes. Figure 3.10 reports the inverse of lifetimes for the two

processes, both in response (a) and in recovery (b) phases in an Arrhenius plot, by clearly showing linear behaviors for the four cases. It should be noted that in the response phase the fast process is too close the time resolution, hindering us to resolve high frequency data (orange box in Figure 3.10). The inverse of a lifetime gives the probability rate, which is thermally activated, as follows:

$$1/\tau = \exp(-E_a/k_B T) \quad (3.4)$$

where  $k_B$  is Boltzmann constant,  $T$  is temperature and  $E_a$  is activation energy ( $E'_a$  for response phase and  $E''_a$  for recovery phase). The physical meaning of these activation energies is depicted in Figure 3.10 (c), as kinetic energy

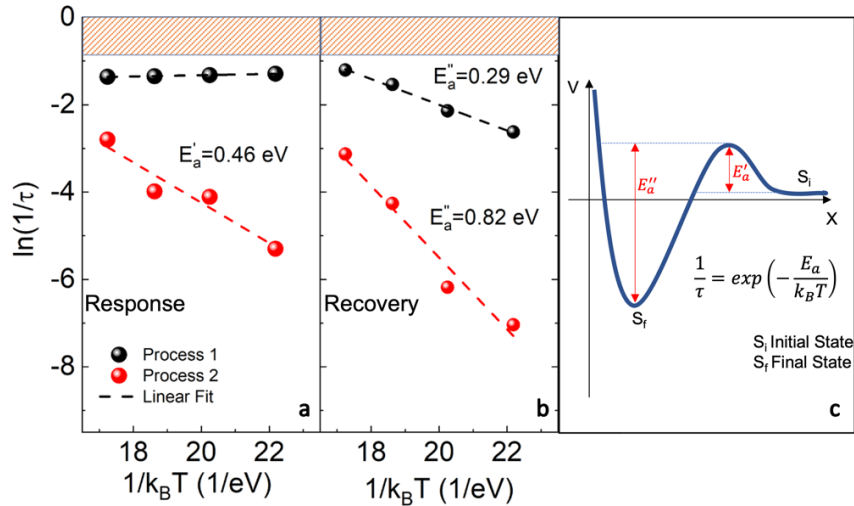


Figure 3.10: Arrhenius plot of inverse of lifetime  $\tau$  of P1 (black sphere) and P2 (red sphere) during (a) response and (b) recovery phase. Dotted lines are linear fit to each set of data. The evidenced region indicates the time resolution of experimental set-up; (c) schematic representation of energy barriers for the sensing processes [64].

barriers in the interaction potential  $V$  between the WO<sub>3</sub> surface and the approaching H<sub>2</sub> molecule. By analyzing the meaningful Arrhenius plots reported in Figure 3.10 for P1 (black spheres) and P2 (red spheres) involved during (a) response phase and (b) recovery phase, we can extract  $E_a$  values for each involved process (dotted lines). The result of such an exercise gives  $E_a$



of 461 meV in the response phase for P2; 295 meV and 821 meV in the recovery phase for P1 and P2, respectively. The experimental determination of these activation energies is a key point to reach a solid description of the WO<sub>3</sub>-H<sub>2</sub> interaction leading to H<sub>2</sub> sensing.

### 3.4.2 H<sub>2</sub> sensing mechanism

It is well assessed that H intercalation occurs in hexagonal WO<sub>3</sub>, especially during the electrochromic processes [91]. H<sub>2</sub> intercalation causes internal changes of WO<sub>3</sub> structure also reflected by a significant change of optical transmittance. Mattoni et al., proposed that WO<sub>3</sub>-H<sub>2</sub> interaction leads to H<sub>2</sub> intercalation in WO<sub>3</sub> crystals [87], while for other models such a process is not required. It is essential now to prove if H<sub>2</sub> intercalation occurs or not in our samples. To this aim, several drops of WO<sub>3</sub> nanorods solution were dropped on corning glass substrates, realizing a very thin film. Two WO<sub>3</sub> coated glasses were annealed at 350 °C for 30 min in forming gas (*FG*, gas mixture of N<sub>2</sub>:H<sub>2</sub>=95:5) or in N<sub>2</sub>. Annealing in *FG* simulates the exposure of WO<sub>3</sub> nanorods to H<sub>2</sub> gas during the sensing test at 350 °C. Transmittance spectra acquired just after annealing of WO<sub>3</sub> coated glasses are shown in Figure 3.11. The annealing in inert ambient does not significantly modify the transmittance curve of the sample. *FG* annealing induces a barely appreciable reduction of transmittance, far away from the expected chromism induced by intercalating H<sub>2</sub>. Moreover, the H<sub>2</sub> intercalation typically produces an enhancement in measured resistance according to Mirazei et al. [92] as following reaction consequence:



On the contrary, after H<sub>2</sub> exposure, our samples reveal a decreased resistance. Such evidence, together with transmittance spectra, rules out H intercalation in WO<sub>3</sub> nanorods during the H<sub>2</sub> sensing test.

To model the WO<sub>3</sub>-H<sub>2</sub> interaction, we now need to discuss the P1 and P2 occurring in response and recovery phase. Firstly, it must be specified that

during the response phase the interaction will involve H<sub>2</sub>, while during the recovery phase only residual H<sub>2</sub>, if any, can be considered. Experimental

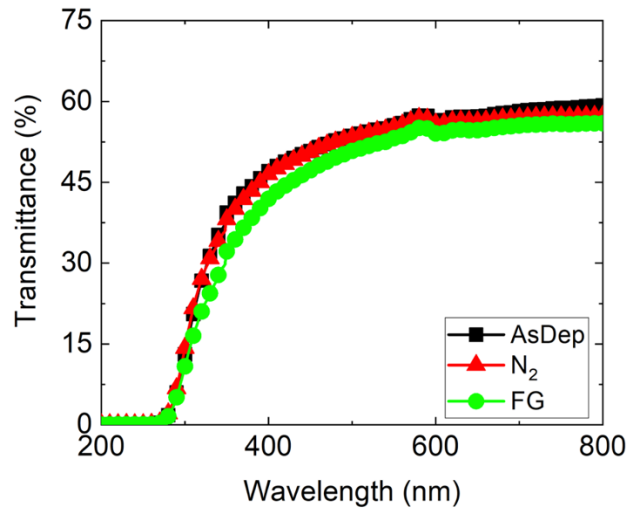
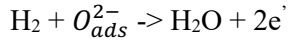


Figure 3.11: Transmittance spectra of AsDep (black line + squares), N<sub>2</sub> (red line + triangles), and FG (green line + circles) samples [64].

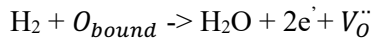
results give us much information about the active processes. The evidence can be summarized as follows:

- P1 is faster than P2, both in response and in recovery phases.  $\tau_1$  is around 4 s, regardless of temperature and concentration, while  $\tau_1^*$  slightly depends on temperature and concentration;
- P1 is more probable than P2, both in response and recovery phases, and at any temperature and any concentration;
- the H<sub>2</sub> concentration dependence of  $w$  suggests a surface process for P1;
- Arrhenius plots hint that P1 is a very fast process in response phase, while it is thermally activated ( $E''_a=295$  meV) at recovery phase when the temperature is ranging between 250 °C and 400 °C. P2 needs high activation energy both in response (461 meV) and recovery phases (821 meV) in the same temperature range; (v) at very low H<sub>2</sub> concentration (below 5000 ppm), only one process is active.

Taking into account these considerations, in response phase, P1 can be described as a *surface process* where a spontaneous interaction occurs between H<sub>2</sub> molecules and oxygen ions adsorbed on the WO<sub>3</sub> surface leading to a water molecule as follows:

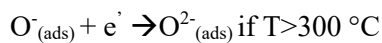
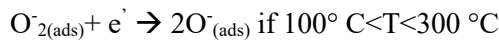
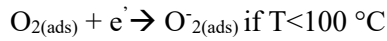
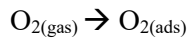


In addition, once water evaporated and oxygen adsorbed on the surface has been reduced, H<sub>2</sub> interacts with the bare WO<sub>3</sub> surface through a *bulk process* involving oxygen atoms bound to surface W atoms [8]. This interaction can lead to P2 in response phase when a water molecule is produced leaving an oxygen vacancy V<sub>O</sub><sup>••</sup>, as follows:

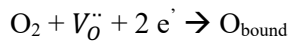


During response phase, both P2 and P1 produce a decrease in measured resistance, according to experimental data.

A different scenario occurs in the recovery phase, where the most probable interaction occurs between O<sub>2</sub> present in dry synthetic air and WO<sub>3</sub> surface. P1 can arise from O<sub>2</sub> molecules rapidly adsorbing on WO<sub>3</sub> surfaces as follows [86]:



P2 can be described as the interaction among O<sub>2</sub> and oxygen vacancies, leading to defect recombination as follows:



Processes occurring in the recovery phase let WO<sub>3</sub> resistance increase, according to experimental data. At very low H<sub>2</sub> concentration, only surface processes occur, both in response and recovery phases.

Figure 3.12 shows a schematic representation of the above-proposed model during response and recovery phases (pink and yellow evidenced area, respectively), where the distinction between *surface* and *bulk process* (P1 and P2 respectively) is clear.

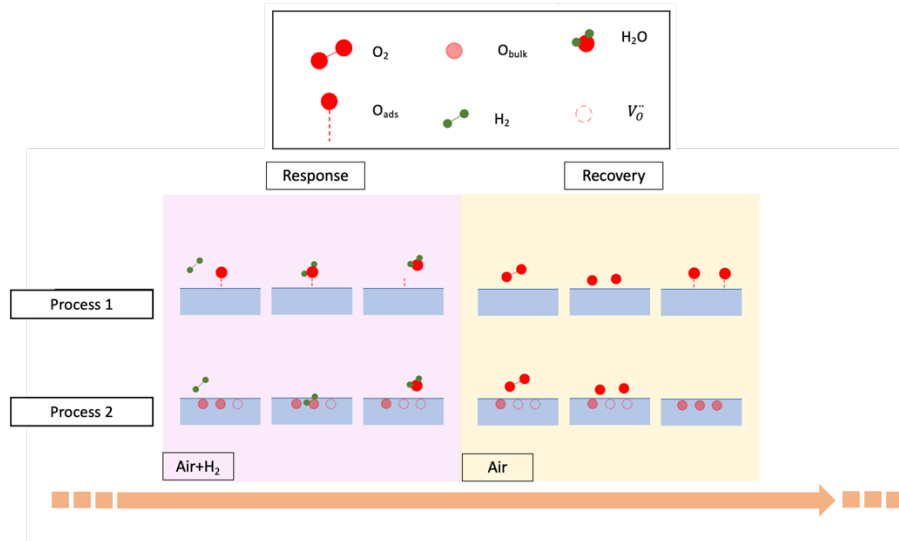


Figure 3.12: Schematic model of surface processes (P1) and bulk processes (P2) involved during the response (pink evidenced area) and the recovery (yellow evidenced area) phase. H<sub>2</sub> interacts with adsorbed oxygen and oxygen directly bound to W to produce a water molecule in response phase, while O<sub>2</sub> can be adsorbed on the WO<sub>3</sub> surface or can occupy an oxygen vacancy to restore the initial condition [64].

### 3.5 NO sensing based on WO<sub>3</sub> nanorods

#### 3.5.1 State of the art

Nitric oxide (NO) is an odorless and colorless gas, largely produced in urban area as exhaust gas of gas stoves and motor vehicles, and in high temperature combustion and industrial processes. Serious health problems can be caused by the exposure to low concentration of NO, such as respiratory diseases and skin

and eyes irritations. Moreover, high concentrations of NO can cause acidic rains, production of ozone and photochemical smog [93, 94]. Therefore, fast, and very sensitive sensors are necessary for the detection of NO, to take under control and even reduce the harmful effects to humans and environmental beings.

Nanostructured metal oxide semiconductors such as CuO [93], TiO<sub>2</sub> [95], MoS<sub>2</sub> [96] and WO<sub>3</sub> [97] are extensively used for the development of NO gas sensors, and the 1D morphology (nanorods, nanowires and nanotubes) seems to be the best way to achieve high sensitivity and low limit of detection (LOD), thanks to the high surface to volume ratio [98]. Among them, WO<sub>3</sub> represents the most suitable candidate for the NO gas sensing, thanks to its high versatility, and stability and the possibility to easily synthesized 1D nanostructures, such as nanorods. Cai et al. [97] synthesized hierarchical flowerlike WO<sub>3</sub> nanostructures by using the solvothermal method, which were tested for NO sensing, by achieving high response under 20 ppm of NO at 200 °C; Chen et al. [99] synthesized WO<sub>3</sub> nanoplates decorated with silver nanoparticles, which showed an operating temperature of 170 °C towards 0.5-100 ppm of NO; Moon et al. [98] synthesized villi-like WO<sub>3</sub> nanostructures by using a glancing angle deposition, which showed a LoD of 88 ppm at 200 °C. Despite the optimal performances of WO<sub>3</sub> for NO sensing, a comprehensive understanding of the interaction between WO<sub>3</sub> and NO based on the experimental results is still missing. A step forward in NO sensing by WO<sub>3</sub> understanding can be achieved through a basic comprehension of actual processing underlying the WO<sub>3</sub>-NO interaction.

### 3.5.2 NO sensing measurements

Preliminary analysis on NO sensing were carried out by using the WO<sub>3</sub> electrode described above. Experimental NO sensing curves are obtained by considering the resistance variations as a function of time while a mixture of NO and dry air or dry air only are fluxed in the test chamber (response and recovery phase respectively). Different temperatures were tested (250-400 °C), though at higher temperatures (400 °C) no response for NO is obtained, as Figure 3.5 (a) shows, while at 350 °C different NO concentrations (250-

2500 ppm) were tested. Figure 3.13 shows the resistance variations (black curve) under different NO concentrations (red curve) at 350°C: the resistance decreases when the NO gas is fluxed into the test chamber (purple arrow) and increases when the NO flux is stopped (yellow arrow). Such a behavior is observed after the interaction between oxidizing gas (such as NO) and *p*-type semiconductor, still WO<sub>3</sub> maintain an *n*-type conductivity, whereby some chemical reduction reactions occurs when NO is fluxed in the test chamber. Such a response of sensor under an NO rich atmosphere allows to define the sensor response *S* (%) according to Eqs 3.1.

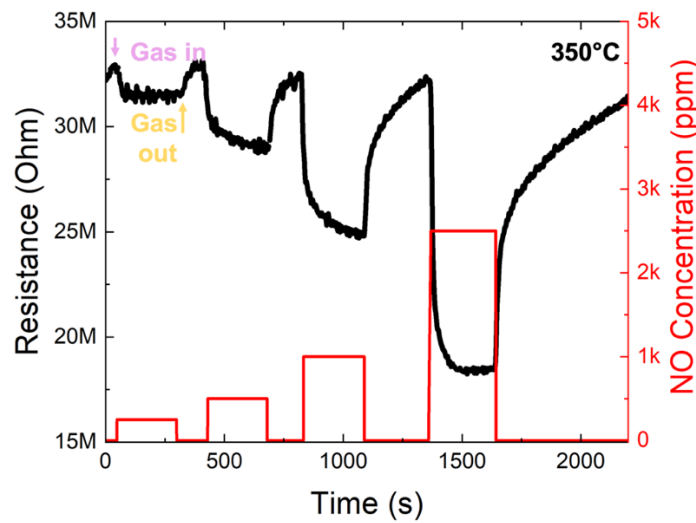


Figure 3.13: Dynamic resistance variation of WO<sub>3</sub>-based sensor (black curve) at 350°C under different NO concentrations (red curve). Arrows indicate when NO is fluxed in the chamber (named “gas in”) or it is stopped (named “gas out”).

To understand the WO<sub>3</sub>-NO interaction, *S*(%) is defined as a function of temperature and concentration. Figure 3.14 shows *S* (%) obtained at different temperatures, (a) 250, (b) 300, (c) 350 °C under 500 ppm flux of NO, as a function of elapsed time, during the response and the recovery phases (defined according to Figure 3.7 b). The response curves rapidly increase when NO is fluxed into the test chamber and tend to saturate within 30 s. After the NO flux is stopped the recovery curves decrease with a temperature dependent trend. *S* (%) is higher the lower the temperature is, but the recovery mechanism is

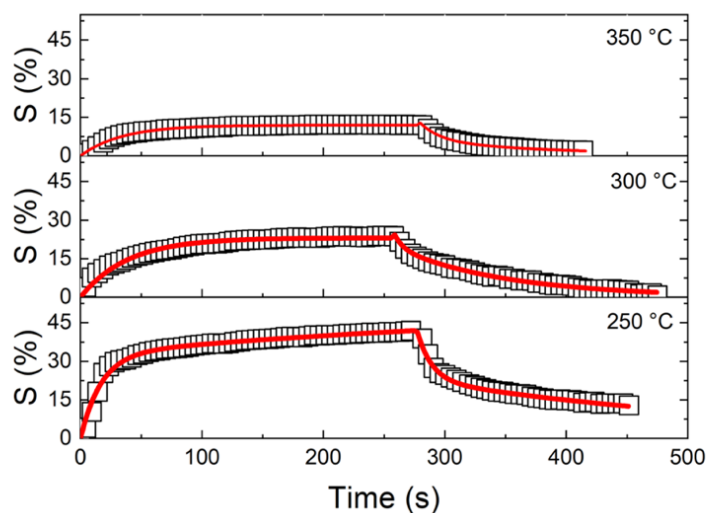


Figure 3.14: Dynamic responses of WO<sub>3</sub>-based sensor (squared symbols) and relative fits (red lines) obtained at (a) 350 °C, (b) 300 °C, (d) 250 °C under 500 ppm of NO as a function of elapsed time starting when NO is fluxed in chamber.

not well efficient. The NO concentration tests were carried out at 350 °C, to maximize the recovery mechanism. Figure 3.15 shows the S (%) obtained under different NO concentrations, (a) 250, (b) 500, (c) 1000, (d) 2500 ppm. The response curves increases when NO is fluxed into the test chamber and tend to saturation after 30 s. After the NO flux stop, the recovery curves decrease and tend to the initial value, as expected. The response is higher the higher the concentration, as well as the recovery phase which requires long time for high concentrations.

### 3.6 NO-WO<sub>3</sub> interaction

Experimental curves describe the mechanism which leads to the NO-WO<sub>3</sub> interaction. In the next paragraph, the response and recovery curves were modeled, to define the chemical reactions which describe the NO sensing mechanism.

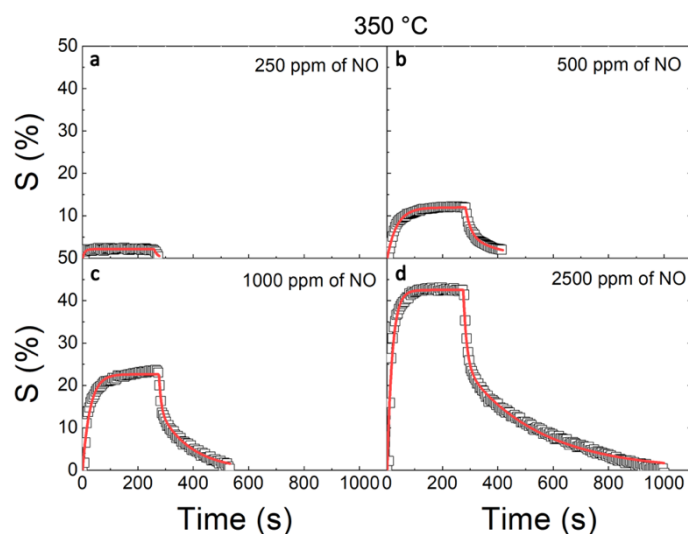


Figure 3.15: Dynamic responses of WO<sub>3</sub>-based sensor (squared symbols) and relative fits (red lines) obtained at 350 °C under (a) 250 ppm, (b) 500 ppm, (c) 1000 ppm, (d) 2500 ppm fluxes of NO as a function of elapsed time.

### 3.6.1 Simulation of experimental curves

The kinetic of the NO sensing can be determined from the analysis of the experimental curves by considering the Langmuir adsorption theory [89], according with Eqs. 3.2 (by fixing  $w=1$  in most cases) and 3.3, for the response and recovery phases, respectively. The fitting curves (red lines) are shown in Figure 3.13 and Figure 3.14 and are in excellent agreement with experimental data (black squares), by confirming that only one process is active during most of the response phases, while during the recovery phase a fast (P1) and a slow (P2) process, independent and concomitant are active. The fitting parameters as a function of temperature are listed in Table 3.3. The maximum response  $S_0$  strongly depends on temperature, it is maximum (53 %) at 250 °C and decreases until 12 % at 350 °C, as expected from the experimental curves. At 250 °C during the response phase both P1 and P2 are active, unlike what happens at 300 and 350 °C, for which only P1 is active. During the recovery phase, both P1 and P2 are active regardless of the temperature, by suggesting the same recovery mechanisms. P1 is characterized by a time of few seconds



Temperature (°C)	S <sub>0</sub> (%)	τ <sub>1</sub> (s)	τ <sub>2</sub> (s)	w (%)	τ* <sub>1</sub> (s)	τ* <sub>2</sub> (s)	w*
250	53±10	16.8±0.8	461±30	60±10	11.8±0.6	288±1	55±1
300	23.1±0.1	39±1	-	-	7±1	93±1	79±1
350	11.9±0.1	34.9±0.5	-	-	17±1	121	65±2

Table 3.3: Results of the fitting procedure to response and recovery transients at various temperatures and at fixed concentration of NO (500 ppm).

(5-40 s) while P2 is characterized by long times both in response (~460 s) and recovery phase (100-300 s). Concerning the weight  $w^*$ , it increases up to 0.8 at 300 °C and then decreases at 350 °C.

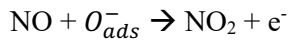
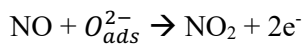
An analogous analysis was carried out at fixed temperature by varying the NO concentration. Experimental curves were fitted in accordance with Eqs. 3.2 and 3.3 (red curves in Figure 3.15), by obtaining an excellent agreement, as mentioned above, and the obtained fitting parameters are reported in Table 3.4. During the response phase only one process is active ( $w=1$ ) with characteristic times of the order of 10-40 s, as well as for the recovery phase of the lowest concentration. In the other cases, the recovery phases are characterized by the activation of two mechanisms, P1 and P2, with short (10-20 s) and long (110-280 s) times, respectively.  $S_0$  increases with the increase of NO concentration, as expected, with the maximum value (42 %) at 2500 ppm.

Concentration (ppm)	S <sub>0</sub> (%)	τ <sub>1</sub> (s)	τ <sub>2</sub> (s)	w (%)	τ* <sub>1</sub> (s)	τ* <sub>2</sub> (s)	w*
250	2.1±0.1	7.9±0.7	-	-	13.7±1	-	-
500	11.9±0.3	35.2±0.5	-	-	18±1	127±10	56±2
1000	25.7±0.7	20±1	254±20	86±4	7.8±0.7	117±2	36±1
2500	42±1	18±2	108±3	97±6	12.6±0.6	272±3	45±1

Table 3.4: Results of the fitting procedure to response and recovery transients at various concentrations of NO at a temperature of 350°C.

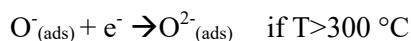
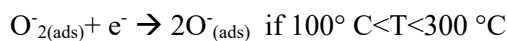
### 3.6.2 NO sensing mechanism

These results allow to identify the chemical reaction which occurs during the NO sensing mechanism, which is dominated by reducing processes, in accordance with the experimental data. Our experimental data suggest an interaction between the NO molecules and the adsorbed oxygen on the WO<sub>3</sub> surface, like the one proposed for the interaction between H<sub>2</sub> and WO<sub>3</sub> described in Paragraph 3.3, rather than a direct interaction with the WO<sub>3</sub>. According to literature [93], interaction between NO and adsorbed oxygen occurs as follow:



which results in a decrease of the electrical resistance, according to the experimental data. At 250 °C both chemical reactions occur, thus leading to the activation of both P1 and P2, while in the other cases only the first occurs, since the  $\text{O}_{\text{ads}}^{2-}$  is the most stable ion at temperatures higher than 300 °C. Figure 3.5 (a) shows that at 400 °C no response towards 500 ppm of NO is obtained. This experimental evidence and the decrease of  $S_0$  with the increase of the temperature suggest a quenching of the interaction between NO and adsorbed oxygen with increasing temperature.

The recovery phase occurs through the interaction between the O<sub>2</sub> present in dry synthetic air and WO<sub>3</sub> surface by restoring of the initial conditions. P1 and P2 can arise from O<sub>2</sub> molecules adsorbed on WO<sub>3</sub> surfaces in the form of  $\text{O}_{\text{ads}}^-$  and  $\text{O}_{\text{ads}}^{2-}$  respectively as follows [86]:



At 250 °C the recovery phase occurs through the activation of only P1, since  $\text{O}_{\text{ads}}^{2-}$  does not exist at this temperature.

### 3.7 Conclusion

A powder of WO<sub>3</sub> nanorods (400 nm long, 50 nm large) is produced by hydrothermal technique and then drop-casted on a Pt interdigitated electrode. The WO<sub>3</sub>-H<sub>2</sub> interaction is studied by testing WO<sub>3</sub> nanorods-based electrodes exposed to H<sub>2</sub> (2000-50000 ppm) fluxes at different temperatures (250-400 °C). The Langmuir adsorption theory was successfully used to model the experimental data of sensing kinetics, evidencing that two processes occur both in response and in recovery phases, regardless of the temperature, for concentrations higher than 5000 ppm. The fast process (lifetimes of few seconds) is attributed to the H<sub>2</sub> interaction with the adsorbed O at the WO<sub>3</sub> surface, in the response phase, and to the O adsorption (barrier of 0.29 eV), in the recovery phase. Since a high concentration of H<sub>2</sub> consumes all the adsorbed oxygen leaving WO<sub>3</sub> uncovered, the slow process (lifetimes of hundreds of seconds) is attributed to the generation (barrier of 0.46 eV) and recombination (barrier of 0.82 eV) of oxygen vacancies in the WO<sub>3</sub> nanorods. No H intercalation in WO<sub>3</sub> bulk is observed. At low H<sub>2</sub> concentration, only fast processes are evidenced, which allows for the promising development of fast H<sub>2</sub> sensing devices.

The same electrode was used to analyze the WO<sub>3</sub>-NO interaction, after the exposure to different concentrations (250-2500 ppm) at different temperature (250-400 °C). The experimental data show an unexpected trend which suggests that the interaction occurs through reducing processes, contrary to what was expected from an oxidizing gas-*n*-type semiconductor interaction.

The Langmuir adsorption theory was successfully used to model the experimental data, by individuating two interaction channels between NO and the adsorbed oxygen species on the WO<sub>3</sub> surface, whose activation depends on the temperature. The fast and the slow channels are attributed to the interaction between NO and  $O_{ads}^{2-}$  and  $O_{ads}^-$ , respectively, with lifetimes of the order of few seconds in the first case and of  $\approx 450$  s in the latter case. The recovery phase is dominated by the O adsorption on the WO<sub>3</sub> surface in the form of  $O_{ads}^-$  and  $O_{ads}^{2-}$  with lifetimes of few seconds in the first case and of 100-300 s in the second case. The higher response at low temperature can open

the route for the development of WO<sub>3</sub>-based NO sensors with low operating temperature.



## Chapter 4

### Engineering Hexagonal/Monoclinic WO<sub>3</sub> Phase Junctions to improve Electrochemical Hydrogen Evolution Reaction

*Electrochemical Hydrogen Evolution Reaction (HER) is one of the most promising green methods to produce renewable and sustainable energy. The development of highly efficient Pt-free electrocatalyst for HER is a crucial point for the eco-sustainability and cost reduction of this procedure. Metal oxide semiconductors seem to be among the most suitable candidates for the development of Pt-free HER catalysts, thanks to their properties. Among them, WO<sub>3</sub> has emerged as favorable material thanks to its advantages properties and its large availability. This chapter presents WO<sub>3</sub> nanorods synthesized by hydrothermal method and calcinated in air at 400 °C for different times (30, 60 and 90 min). Experimental investigation involved scanning and transmission electron microscopy (SEM and TEM), X-ray diffraction (XRD) and electrochemical analysis such as linear sweep voltammetry (LSV), cyclic voltammetry (CV), electrochemical impedance spectroscopy (EIS) and Mott Schottky analysis. Calcination at 400 °C induces a peculiar crystal phase transition characterized by hexagonal/monoclinic WO<sub>3</sub> phase junctions. The best HER performance (170 mV overpotential for 10 mA/cm<sup>2</sup>) is obtained when WO<sub>3</sub> nanorods show comparable volumes of hexagonal and monoclinic phases (after 60 min annealing). The effect of phase junction on the HER catalysis sustained by WO<sub>3</sub> nanorods is investigated in detail, opening the route to the realization of efficient catalysts for HER application.*

## 4.1 H<sub>2</sub>: a green source of energy

The finite supply of fossil fuels, the climate change, and the growing world energy demand inspire a great interest in scientific community to develop renewable and sustainable energy sources, among which H<sub>2</sub> attracts a lot of awareness. H<sub>2</sub> can be produced from natural gas reservoir, or after the fermentation of biomass, or after the water splitting process, and, after the storage and distribution, can be used as source of energy both in transportation and industrial application (Figure 4.1), thanks to the possibility to store H<sub>2</sub> in different ways, such as electrochemical (batteries and supercapacitors) and physisorption systems (see Appendix A3 for more details). The most promising green methods to produce highly pure H<sub>2</sub> on a large scale, with zero carbon emission, sustainability, recyclability, and eco-friendliness is water electrolysis through Hydrogen and Oxygen Evolution Reactions (HER and OER respectively) at cathode and anode, respectively [19, 100, 101]. Figure 4.2 shows a typical electrochemical cell in which H<sub>2</sub> and O<sub>2</sub> are produced at the same time under an external applied potential [102].

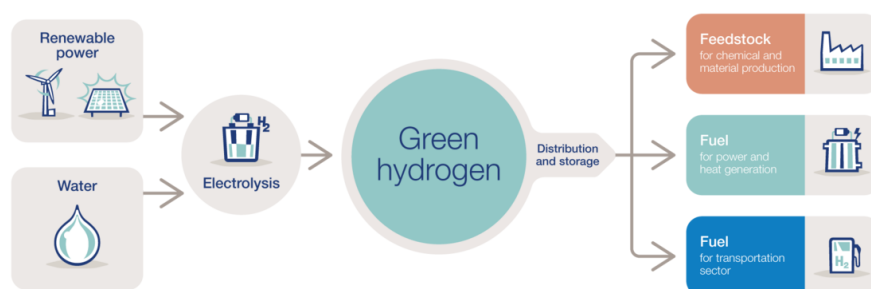


Figure 4.1: The hydrogen chain [103].

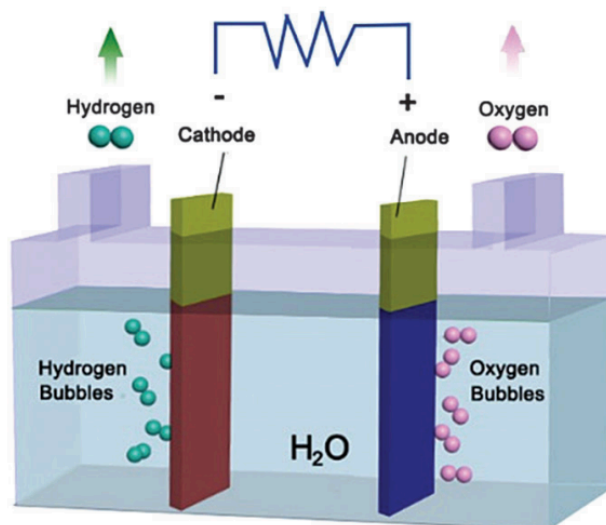
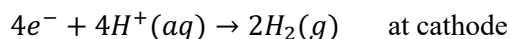
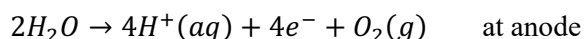


Figure 4.2: Schematic of an electrochemical cell for water splitting reaction [102].

Electrochemical water splitting reactions occurs at cathode and anode (negative and positive electrode respectively) as follows (in acidic environment) [100]:



Consequently, H<sub>2</sub> and O<sub>2</sub> gases are produced at the same time at the cathode and anode respectively and can be collected and stored.

The most active catalysts for (HER) are Pt-based materials, but the large-scale application of this way is limited by the low availability and the high supply cost of Pt [104, 105]. Many efforts have been made by the scientific community to develop valid Pt substitutes with the purpose of lower H<sub>2</sub> production costs. The use of Pt nanoparticle significantly reduce the Pt amount and the costs, whereby to decorate active substrate with Pt nanoparticles seems to be an effective alternative [106]. Nevertheless, transition metal oxides aroused a great interest as these, if opportunely engineered, can be used to replace Pt and to realize Pt-free catalyst [107-110].



### 4.1.1 Overview on WO<sub>3</sub> based HER

As mentioned before, WO<sub>3</sub> has emerged as favorable material thanks to its large availability and advantageous properties [111-116]. WO<sub>3</sub> shows high electrochemical stability in acidic environments, tunable bandgap, and good proton conduction and conduction band position near the H<sup>+</sup>/H<sub>2</sub>O production level (Figure 1.9); unfortunately, as a semiconductor, it has poor electron transport ability and few active sites hindering high HER performances [104, 117,118]. These negative aspects can be strongly reduced by an effective strategy using nanostructures with high surface to volume ratio and low resistance to further improve electrochemical properties of WO<sub>3</sub> as cathode for HER. WO<sub>3</sub> nanostructures can be effectively synthesized by hydrothermal [119], sputtering [120], thermal evaporation [121], sol-gel [122] and electrodeposition [42] methods. Nevertheless, in its pristine form, nanostructured WO<sub>3</sub> does not give excellent HER performances, since the atomic hydrogen adsorption free energy ( $\Delta G_H$ ) on the W-site is high, this leads to a poor HER activity, as explained by the Sabatier's principle for which  $\Delta G_H$  close to zero gives better catalytic performances [104, 123, 124]. Many efforts have been done with the aim of modulating WO<sub>3</sub> electronic structure, such as decoration with Pt clusters [125, 126], the embedation of W-based compounds on conductive supports such as reduced graphene oxide (RGO) [118] and carbon nanotubes (CNTs) [112], and the realization of heterostructures by coupling WO<sub>3</sub> with other transition metal oxides [127-129]. Although these solutions are effective to enhance HER activity, their exploitation on a large scale is limited by complex synthesis and assembly processes.

The crystal phase of WO<sub>3</sub> can also play a pivotal role. The hexagonal structure of WO<sub>3</sub> seems to be the most performing for electrochemical applications due to the favorable H<sup>+</sup> intercalation-release pathways [130], while the monoclinic phase results the more stable at room temperature [2]. The combination of a mixed hexagonal-monoclinic WO<sub>3</sub> based heterostructure has been recently shown to enhance the photo-electrochemical ability, by means of a Z-scheme in energy bands, promoting electron-hole pairs separation [131-132]. Such a heterostructure can be extremely interesting for HER since the hexagonal-

monoclinic interface can act as active site for H<sup>+</sup> adsorption, thanks to the formation of an electrons' reservoir promoting the catalytic and electrical properties.

In the next paragraphs, the synthesis WO<sub>3</sub> nanorods with hexagonal-monoclinic phase junction will be presented, as well as the morphological and the electrochemical characterization. The HER mechanism is hence modeled, considering the role of the crystal structure.

### 4.2 Engineering WO<sub>3</sub> based cathode

Hexagonal WO<sub>3</sub> nanorods are synthesized by using the optimized hydrothermal synthesis as reported Chapter 2 (denoted as WO<sub>3</sub>\_NA). Some samples underwent a calcination process in air on a hot plate at 400°C for 30, 60 and 90 minutes (denoted as WO<sub>3</sub>\_A30, WO<sub>3</sub>\_A60, and WO<sub>3</sub>\_A90, respectively). A schematic of this process is shown in Figure 4.3 a. The obtained WO<sub>3</sub> based nanostructures were used for the realization of different pastes (20 mg of nanostructures powder, 0.1 ml of Nafion and 2 ml of deionized water, with subsequent filtration by a 1.2 μm filter to select only the nanorods morphology) as shown in Figure 4.3 a. Electrodes are produced by drop casting the obtained WO<sub>3</sub>-based pastes on graphene paper substrates (GP, 2x1 cm<sup>2</sup>, Sigma Aldrich, 240 μm thick). The mass of the electrode (substrate + WO<sub>3</sub> nanostructures) and of bare substrate were measured by a Mettler Toledo MX5 Microbalance (sensitivity: 0.01 mg). The morphological analyses were carried out by a scanning electron microscope (SEM) Gemini Field Emission SEM Carl Zeiss SUPRATM 25 (FEG-SEM, Carl Zeiss Microscopy GmbH, Jena, Germany) in IN-LENS mode. Figure 4.3 b-e show low (main figure) and high (inset) magnification SEM images of WO<sub>3</sub>\_NA, WO<sub>3</sub>\_A30, WO<sub>3</sub>\_A60 and WO<sub>3</sub>\_A90 based electrodes, which appear composed of oddly aligned nanorods (0.5-1 μm long and 50 nm large, see insets in Figure 4.3) stacked on top of each other until they form a homogeneous and very porous film, that does not change by the thermal

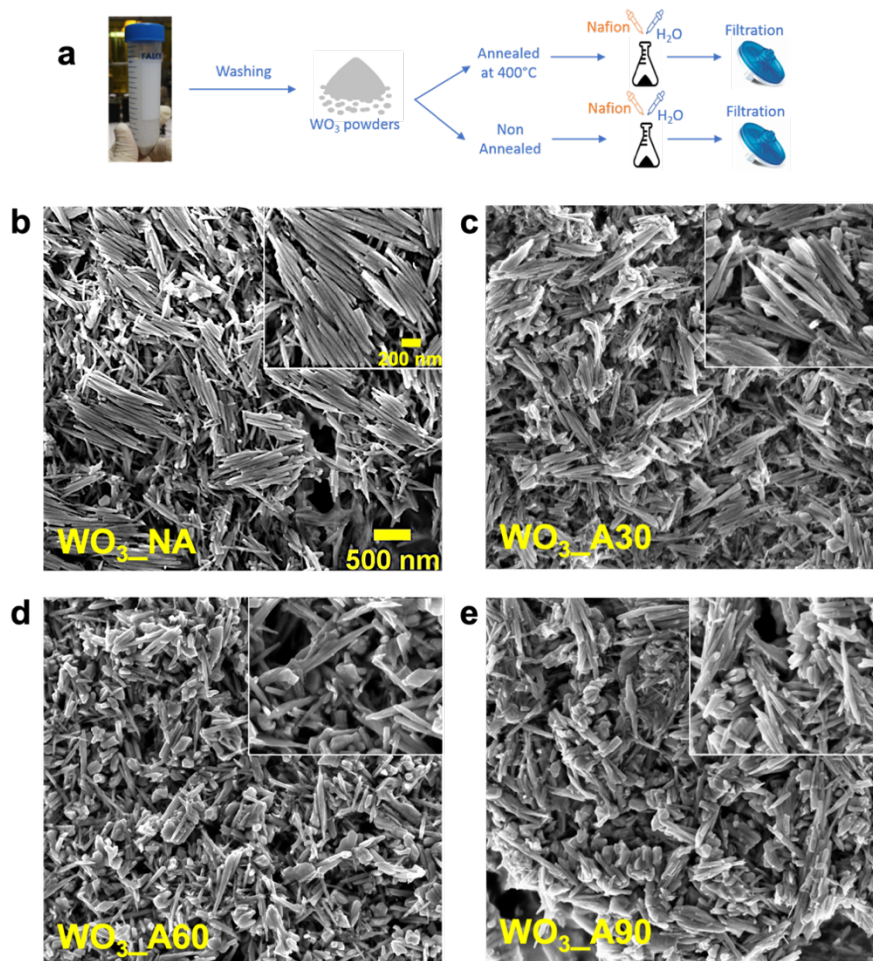


Figure 4.3: a)  $\text{WO}_3$  powder extraction, annealing, and filtering; low and high (inset) magnification SEM images of (b)  $\text{WO}_3\_NA$ , (c)  $\text{WO}_3\_A30$ , (d)  $\text{WO}_3\_A60$  and (e)  $\text{WO}_3\_A90$  based electrodes. Markers in (b) are valid for all relative images [133].

treatment, as also reported in literature [131].

A change in the phase structure of  $\text{WO}_3$ -based nanostructures during annealing processes was analyzed as a function of annealing time. Film structure was analyzed through XRD using a Smartlab Rigaku diffractometer, in grazing incidence  $0.5^\circ$ , equipped with a rotating anode of  $\text{Cu K}\alpha$  radiation operating at 45 kV and 200 mA. The scans were acquired from  $10^\circ$  to  $70^\circ$  with

a step of 0.02°<sup>3</sup>. Figure 4.4 a shows the XRD patterns of WO<sub>3</sub>\_NA, WO<sub>3</sub>\_A30, WO<sub>3</sub>\_A60 and WO<sub>3</sub>\_A90 powders compared with XRD patterns of hexagonal (PDF #89-4476) and monoclinic (PDF #75-2187) WO<sub>3</sub> respectively. The XRD pattern of WO<sub>3</sub>\_NA shows the typical diffraction peaks related to the hexagonal crystal structure, which appear at 2 $\Theta$  = 14.00°, 24.36°, 26.84°, 28.22°, 33.62°, 36.58°, and 49.95° as expected, indicating the pure hexagonal phase in as prepared WO<sub>3</sub> nanorods [64]. Besides the above-mentioned diffraction peaks, with the increasing of annealing time, new peaks appear (2 $\Theta$  = 23.00°, 23.50°, 24.28°, 33.12°, 33.54°, 33.84°, 34.04°, 49.74°, 55.71°) with increasing intensity, clearly related to the monoclinic crystal structure, by suggesting the coexistence of hexagonal and monoclinic WO<sub>3</sub> phases (*h*-WO<sub>3</sub> and *m*-WO<sub>3</sub>) in WO<sub>3</sub>\_A30, WO<sub>3</sub>\_A60 and WO<sub>3</sub>\_A90 powders. So, according to XRD results shown in Figure 4.4 a, *h*-WO<sub>3</sub> starts to change phase towards *m*-WO<sub>3</sub> as soon as the annealing process begins.

By using the Reference Intensity Ratio (RIR) method, the weight ratio (W%) of *h*-WO<sub>3</sub> and *m*-WO<sub>3</sub> (W<sub>h</sub>% and W<sub>m</sub>% respectively) in WO<sub>3</sub>\_NA, WO<sub>3</sub>\_A30, WO<sub>3</sub>\_A60 and WO<sub>3</sub>\_A90 powders can be calculated, starting from the intensities of the strongest line of the X-ray diffraction patterns (*I*) as follows [131, 134]:

$$W_h = \frac{I_h}{I_h + (I_m / (RIR_m / RIR_h))}$$

$$W_m = \frac{I_m}{I_m + (I_h / (RIR_h / RIR_m))} = 1 - W_h$$

where *h* and *m* denote the different coexistent hexagonal and monoclinic crystal phases respectively and the *RIR* values depends on the analyzed crystal phases, which for the *h*- and *m*-WO<sub>3</sub> are 8.33 (PDF #89-4476) and 5.58 (PDF #75-2187). Figure 4.4 b shows the obtained values for the W<sub>h</sub>% and W<sub>m</sub>% as a function of the annealing time. The intensities of *m*-WO<sub>3</sub> peaks increase

<sup>3</sup> These analyses were carried out in collaboration with Prof. Graziella Malandrino at the Bio-nanotech Research and Innovation Tower (BRIT) laboratory of the University of Catania, Italy.

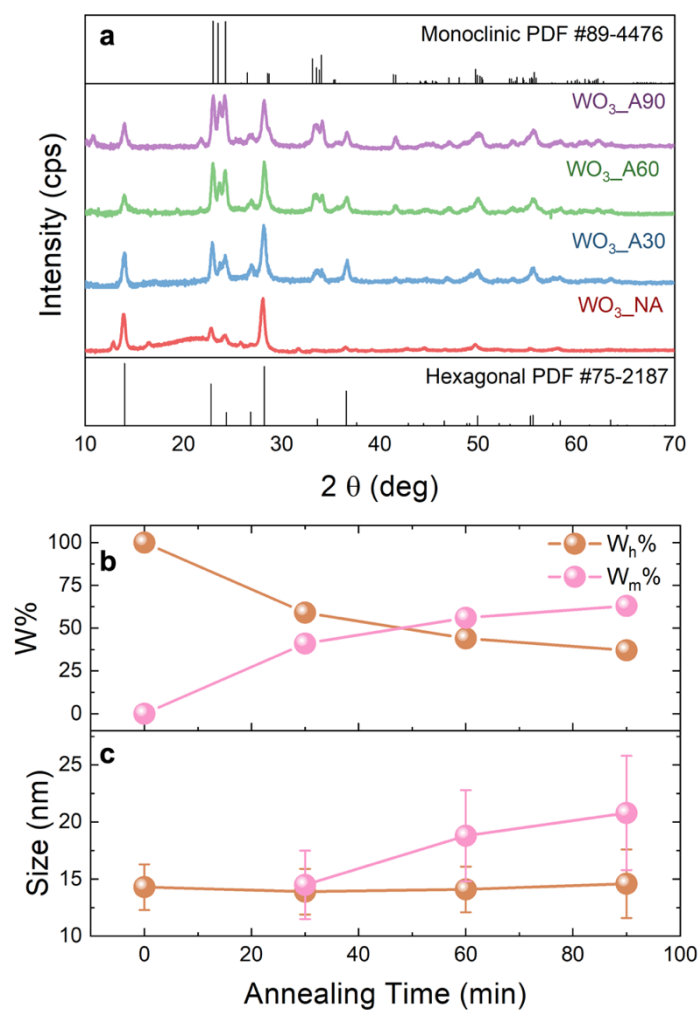


Figure 4.4: (a) XRD pattern of WO<sub>3</sub>\_NA, WO<sub>3</sub>\_A30, WO<sub>3</sub>\_A60 and WO<sub>3</sub>\_A90 powders, compared with pure hexagonal and monoclinic WO<sub>3</sub> XRD pattern; (b) weight ratio (W%) and (c) crystallites size of h-WO<sub>3</sub> and m-WO<sub>3</sub> (brown and pink spheres) as a function of the annealing time for WO<sub>3</sub> based powders [133].

gradually with increasing the annealing time, starting from 0 W% for the WO<sub>3</sub>\_NA sample until reaching 63 W% for the WO<sub>3</sub>\_A90 sample. A full phase transition into the monoclinic phase does not occur in our samples, as

longer times or higher temperatures are needed, as expected [131]. In fact, annealing conditions were chosen to allow a careful modification of hexagonal/monoclinic volume ratio, greatly useful for HER optimization. The size of the h- and m-WO<sub>3</sub> sub-micrometer crystallites (D) can be calculated by using the Scherrer equation [135] as follows:

$$D = \frac{k\lambda}{\sqrt{B_{mis}^2 - B_{instr}^2} \cos \theta}$$

where  $k$  is a dimensionless shape factor which is typical equal to 0.9,  $\lambda$  is the wavelength of used radiation which is 0.154 nm,  $B_{mis}^2$  and  $B_{instr}^2$  are the measured broadening of the half maximum intensity of the characteristic XRD peaks and the instrumental correction (0.1°) respectively (in radians) and  $\theta$  is the Bragg angle at which the XRD peak occurs. Figure 4.4 c shows the size of hexagonal and monoclinic crystallites as a function of the annealing time (error bars are reported for each measurement). It is worth to note that the thermal treatment affects the m-WO<sub>3</sub> crystallites size, which increases with the annealing time. However, h-WO<sub>3</sub> crystallites size does not depend on the annealing time. The observed reduction of  $W_h\%$  with annealing suggests a decrease of h-WO<sub>3</sub> crystallites density.

Transmission electron microscopy (TEM) analyses were performed by using a transmission electron microscope (TEM) JEOL, JEM-ARM200F operated in TEM mode, to investigate morphology and crystal structure of single nanorods<sup>4</sup>. Figure 4.5 a reveals that each nanorod is composed of a bundle of smaller needles (large 10 nm about) probably stuck together during hydrothermal synthesis. These needles are well aligned each other's, with the main dimension along the c-axis as shown by the Fast Fourier Transform (FFT) on the inset. The high-resolution micrograph of a WO<sub>3</sub> nanoneedle (Figure 4.5 b) clearly shows a phase junction among hexagonal and monoclinic structures (confirmed by respective FFT in the insets). Such

---

<sup>4</sup> These analyses were carried out in collaboration with Dr. Mario Scuderi at CNR-IMM Institute of Catania.

evidence confirms the presence of h-/m-WO<sub>3</sub> phase junctions in the WO<sub>3</sub>\_A60 powder, as expected from XRD results.

In the next paragraph, the as studied electrodes (WO<sub>3</sub> based pastes on GP) will be electrochemically analyzed, to study the HER catalytic activity as a function of the crystal structure.

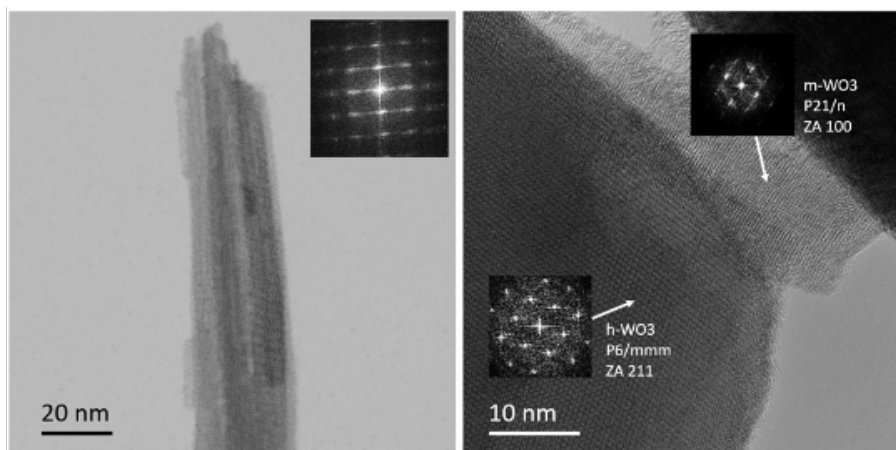


Figure 4.5: (a) TEM bright-field image of a single nanorod, composed of aligned nanoneedles; (b) high-resolution TEM image which confirms the presence of h-/m-WO<sub>3</sub> phase junction. Inset (a) FFT of Figure a; (b) FFT of h- and m-WO<sub>3</sub> [133].

### 4.3 Electrochemical H<sub>2</sub> production

#### 4.3.1 HER catalytic performance

HER catalytic activity as a function of crystal structure of WO<sub>3</sub> based electrodes was thoroughly analyzed. The electrochemical measurements were performed at room temperature by using a potentiostat (VersaSTAT 4, Princeton Applied Research, USA) and a three-electrode setup with a graphite rod electrode as counter electrode (to avoid any Pt contaminations), a saturated calomel electrode (SCE) as reference, and WO<sub>3</sub> onto GP as working electrode, in 1 M H<sub>2</sub>SO<sub>4</sub> supporting electrolyte. Electric current values were normalized to the geometrical immersed surface area of each electrode. The measured

potential vs SCE was converted into the reversible hydrogen electrode (RHE) according to the Nernst equation [128, 136]:

$$E'_{RHE} = E_{SCE}^{\theta} + E_{SCE} * 0.059 * pH \quad (4.1)$$

where  $E_{SCE}^{\theta}$  is the standard potential of the SCE electrode at 25 °C (0.241 V) and  $E_{SCE}$  is the measured potential vs SCE. The HER activities of various WO<sub>3</sub> based electrodes were investigated using a linear sweep voltammetry (LSV) recorded at 5 mV/s from -0.2 V to -0.8 V vs SCE. Electrochemical impedance spectroscopy (EIS) was performed from 100 kHz to 0.1 Hz in a potentiostatic mode with an AC voltage of 5 mV at the potential (vs SCE) at 10 mA/cm<sup>2</sup> in the LSV curves. The double layer Capacity ( $C_{dl}$ ) was determined from Cyclic Voltammetry (CV) curves, recorded at different scan rates (5 to 100 mV/s) from -0.2 V to -0.3V vs SCE. All the obtained potential vs RHE are manually corrected by  $iR_u$  compensation as follows:

$$E_{RHE} = E'_{RHE} - iR_u \quad (4.2)$$

where  $i$  is the electrode current and  $R_u$  [ $\Omega$ ] is the uncompensated resistance, measured by EIS [100]. The Mott-Schottky analyses were carried out from -0.2 V to -1.6 V vs SCE at 1000 Hz frequency.

Figure 4.6 a shows the  $iR_u$  corrected LSV curves reported vs RHE scale (Eqs. 4.1 and 4.2) of WO<sub>3</sub>\_NA, WO<sub>3</sub>\_A30, WO<sub>3</sub>\_A60 and WO<sub>3</sub>\_A90 based electrodes, at scan rate of 5 mV/s. All the polarization curves show a similar trend, with an initial current density plateau followed by a rapid increasing current density evidencing a more and more pronounced H<sub>2</sub> production. WO<sub>3</sub>\_NA and WO<sub>3</sub>\_A90 electrodes (red and violet curves, respectively) show almost overlapping polarization curves, thus revealing a similar HER behavior. WO<sub>3</sub>\_A30 electrode polarization curve (blue curve) shows a little improvement in terms of current density produced at fixed potential. WO<sub>3</sub>\_A60 electrode (green curve) shows an excellent polarization curve, with a strong current density at moderately low negative potential, revealing very good electrocatalytic HER activity. In details, the overpotential at 10 mA/cm<sup>2</sup> ( $\eta$ ) of WO<sub>3</sub>\_A60 electrode is 170 mV, whereas WO<sub>3</sub>\_NA, WO<sub>3</sub>\_A30 and



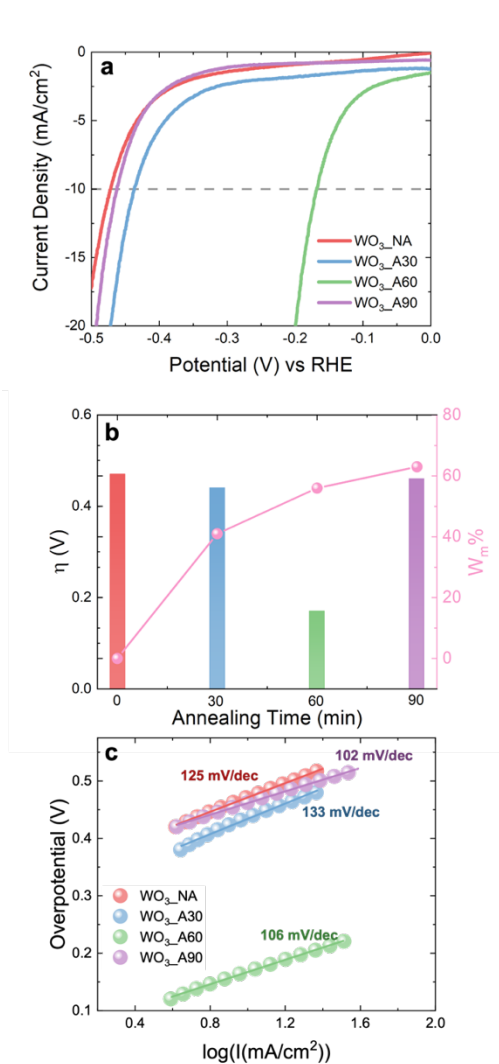


Figure 4.6: a) LSV curves, b)  $\eta$  and Wh% as a function of annealing time and c) Tafel plots related to the WO<sub>3</sub>\_NA (red), WO<sub>3</sub>\_A30 (blue), WO<sub>3</sub>\_A60 (green) and WO<sub>3</sub>\_A90 (violet) electrodes. The dashed line in (a) indicates the current density of 10 mA/cm<sup>2</sup> [133].

WO<sub>3</sub>\_A90 electrodes show  $\eta$  values of about 460 mV ( $\eta$  values are listed in Table 4.1). The supremacy of HER performance of WO<sub>3</sub>\_A60 electrode can be also appreciated by its current at overpotential of 170 mV (10 mA/cm<sup>2</sup>) which is 10 times higher than that of WO<sub>3</sub>\_NA, WO<sub>3</sub>\_A30 and WO<sub>3</sub>\_A90

	W <sub>h</sub> %	η (mV)	Tafel slope (mV/dec)	C <sub>dl</sub> (mF)	ECSA (cm <sup>2</sup> )	TOF @ η (mHz)
WO <sub>3</sub> _NA	100	470	125	2.48	83	17
WO <sub>3</sub> _A30	59	440	133	3.05	102	13
WO <sub>3</sub> _A60	44	170	106	2.98	100	15
WO <sub>3</sub> _A90	37	460	102	2.03	68	12

Table 4.1: *h*-WO<sub>3</sub> content, η, Tafel slope, C<sub>dl</sub>, ECSA and TOF of WO<sub>3</sub>\_NA, WO<sub>3</sub>\_A30, WO<sub>3</sub>\_A60 and WO<sub>3</sub>\_A90 electrodes [133].

electrodes at the same overpotential. The annealed series from 30 to 90 minutes was experimentally reproduced 2 times, confirming the best outcomes for 60 min annealing. The η and crystal phase mixture trends as a function of the annealing time are reported in Figure 4.6b. By increasing the W<sub>m</sub>% up to 56%, η decreases to its minimum value (170 mV, for WO<sub>3</sub>\_A60). A further increase of W<sub>m</sub>% (63%) leads to a worsening of HER catalytic activity, which becomes comparable to that of fully hexagonal phase. Such a behavior clearly indicates that a mixture of phase is better than a single phase. While it is clearly established that a fully hexagonal phase is much better than a fully monoclinic one [111, 116], here we demonstrate that when hexagonal and monoclinic phase coexist at a comparable extent the highest HER performance is obtained.

To deepen such experimental evidence, we analyzed the kinetics of HER in our samples. Figure 4.6c shows the Tafel plot and the relative linear fit of WO<sub>3</sub>\_NA, WO<sub>3</sub>\_A30, WO<sub>3</sub>\_A60 and WO<sub>3</sub>\_A90 electrodes (solid speres curves and solid lines, respectively). The Tafel slope is defined by the slope of the linear fit of the potential vs log[j(mA/cm<sup>2</sup>)] plot, according with the follow equation [19]:

$$E_{RHE} = b * \log(j) + a$$

Where  $E_{RHE}$  is the  $iR_u$ -free potential (V),  $b$  is the Tafel slope (V/dec),  $j$  is the current density (mA/cm<sup>2</sup>) and  $a$  is a constant. The appropriate potential region for the Tafel slope analysis is chosen to ensure that the measured current density results from faradaic reaction [19]. All Tafel plots show the same slope, in the range of 100-130 mV/dec (values are listed in Table 4.1). A slightly lower Tafel slope seems to be related to a higher monoclinic volume ratio, even if the variation among all samples is fairly limited. The lack of variation in Tafel slope is an index of the same HER mechanism, regardless on the hexagonal and monoclinic content in WO<sub>3</sub>. The Tafel slope is strictly related to the rate-determining step (RDS) among the elementary characteristic steps through which HER occurs [137]. According to Tian et al., HER process in acidic environment occurs through combinations of the following step, called the Volmer, Tafel and Heyrovsky equations respectively [137]:



where \* denotes the active adsorption site. In details, the HER occurs through a Volmer-Tafel or a Volmer-Heyrovsky mechanism depending on the electrode material. Moreover, Tafel slope around 118 mV/dec is typically related to HER for which the Volmer process act as the RDS [137]. Such a situation describes all our WO<sub>3</sub> based electrodes, for which the HER process is limited by H<sup>+</sup> adsorption process on the electrode surface. Such evidence is not in contrast with the variation of W<sub>h</sub>%/W<sub>m</sub>% ratio as this last parameter fairly regards material bulk while H adsorption process occurs at surface.

The HER activity was further evaluated by calculating the electrochemical active surface area (ECSA) parameter, measured by the double layer capacity ( $C_{dl}$ ) as follows [138]:

$$ECSA = \frac{C_{dl}}{C_s}$$

where  $C_s$  is the specific capacitance of the used electrolyte which is equal to 30  $\mu\text{F}/\text{cm}^2$  in case of 1M H<sub>2</sub>SO<sub>4</sub>  $C_s$  [19].  $C_{dl}$  was determined from cyclic voltammetry (CV) curves, recorded at different scan rates (from 5 to 100 mV/s) in the non-faradaic region from -0.2 V to -0.3 V vs SCE (see the Appendix A4), from the slope of ( $J_a - J_c$ ) vs the scan rate plot at fixed potential (-0.25V) according to the follow relation [139-141]:

$$C_{dl} = \frac{(J_a - J_c)}{2v}$$

where  $v$  is the scan rate in V/s. Figure 4.7 a shows the plot of ( $J_a - J_c$ ) recorded at -0.25 V from CV curves of Figure A4.1 vs the scan rate (red, blue, green, and violet solid sphere) and related linear fits (red, blue, green and violet solid line) which allow defining the  $C_{dl}$  at -0.25 V [101]. The  $C_{dl}$  and ECSA values are listed in Table 4.1. The  $C_{dl}$  (ECSA) values are comparable for the WO<sub>3</sub>-electrodes with intermediate m-WO<sub>3</sub> content (3.05 mF (102 cm<sup>2</sup>) and 2.98 mF (100 cm<sup>2</sup>) for WO<sub>3</sub>\_A30 and WO<sub>3</sub>\_A60), while are slightly lower for the WO<sub>3</sub>-electrodes with the prevalence of a hexagonal or monoclinic crystalline phase (2.48 mF (83 cm<sup>2</sup>) and 2.04 mF (68 cm<sup>2</sup>) for WO<sub>3</sub>\_NA and WO<sub>3</sub>\_A90). The slightly higher  $C_{dl}$  and ECSA values for WO<sub>3</sub>\_A60 are not high enough to explain its excellent catalytic HER activity. Thus, further in-depth electrochemical analysis were carried out.

The charge transfer kinetics occurring at the interface between the electrolyte and the WO<sub>3</sub> coated electrode was investigated by using EIS analysis. Figure 4.7 b shows the Nyquist plot for all the WO<sub>3</sub> based electrodes (solid spheres). All the EIS spectra exhibit a hint of a very small (inset of Figure 4.7 b) and a large semicircle in the higher and lower frequency region, respectively. The impedance data were interpreted and fitted (solid line in Figure 4.7 b) using the equivalent circuit of Armstrong and Henderson reported in Figure 4.7 b.  $R_u$  represents the uncompensated resistance used in Eq. 4.2 for the  $iR_u$  correction of LSV current,  $R_{ct}$  represents the charge transfer resistance related to the substrate electrode reaction,  $R_p$  is related to the mass charge resistance of the intermediate  $H_{ads}$  on the surface of catalytic material which is also called *pseudo-resistance* and  $C_{dl}$  and  $C_p$  are constant phase capacitances, which represents the double layer capacitance and the pseudo-capacitance (at  $\eta$ )

respectively and are described by pre-exponential ( $P_{dl}$  and  $P_p$ ) and an exponential ( $n_{dl}$  and  $n_p$ ) factors [142]. All fit values are reported in Table 4.2.

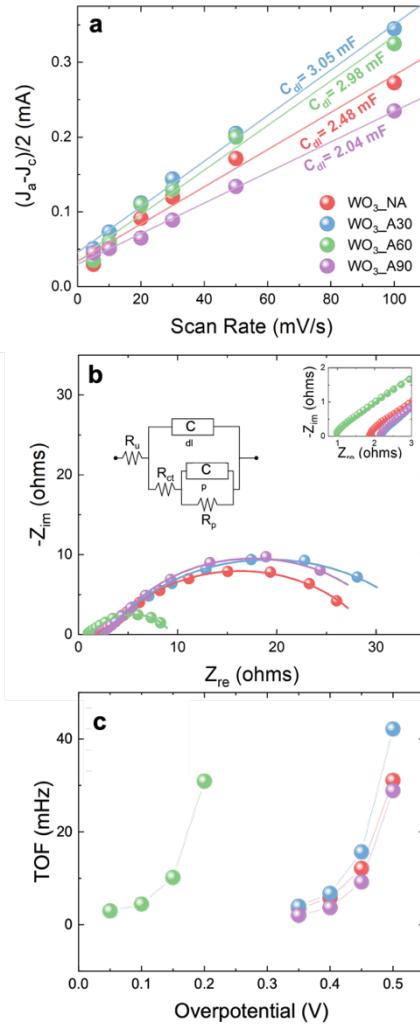


Figure 4.7: (a) plot of  $(J_a - J_c)$  recorded at  $-0.25$  V vs the scan rate (solid sphere) and related linear fits (solid line), (b) EIS analyses and (c) TOF as a function of overpotential of WO<sub>3</sub>\_NA (red), WO<sub>3</sub>\_A30 (blue), WO<sub>3</sub>\_A60 (green) and WO<sub>3</sub>\_A90 (violet) electrodes. Inset: Armstrong and Henderson equivalent circuit and magnification of high frequency region [133].

	$P_{dl}$ (*10 <sup>-3</sup> )	$n_{dl}$	$P_p$ (*10 <sup>-3</sup> )	$n_p$	$R_u$ (ohm)	$R_{ct}$ (ohm)	$R_p$ (ohm)
<b>WO<sub>3</sub>_NA</b>	1	0.7	4	0.7	1.9	2.3	25.4
<b>WO<sub>3</sub>_A30</b>	3	0.7	5	0.7	2.2	2.3	31
<b>WO<sub>3</sub>_A60</b>	0.4	0.8	5	0.7	2	1.2	7.3
<b>WO<sub>3</sub>_A90</b>	1	0.7	2	0.7	2.1	2.7	27

Table 4.2: EIS parameter of WO<sub>3</sub>\_NA, WO<sub>3</sub>\_A30, WO<sub>3</sub>\_A60 and WO<sub>3</sub>\_A90 electrodes [133].

$P_{dl}$  and  $n_{dl}$  are similar for all WO<sub>3</sub>-based electrodes as well as  $P_p$  and  $n_p$ . The  $R_{ct}$  values are similar each other regardless of crystal phase composition of WO<sub>3</sub> nanostructures-based electrodes, by confirming that the substrate role is the same as well the substrate coverage for all WO<sub>3</sub> based electrodes. The sum of  $R_{ct}$  and  $R_p$  represents the total faradaic resistance of the electrode at fixed potential [142]. The smallest value of  $R_p$ , which results into the smallest faradaic resistance, is obtained for the WO<sub>3</sub>\_A60 electrode which possesses the highest HER activity. Since  $R_{ct}$  and  $R_p$  are strictly correlated to the active Volmer, Tafel or Heyrovsky mechanisms, the catalytic activity of WO<sub>3</sub>\_A60 electrode can be ascribed to a more favorable H<sup>+</sup> adsorption on the surface, thanks to a lowering of the total faradaic resistance of the HER mechanism, thus pointing out the correlation between the H<sup>+</sup> adsorption process and the phase junction formation which depends on the m-WO<sub>3</sub> and h-WO<sub>3</sub> content in WO<sub>3</sub>-based electrodes.

To further study the HER activity of WO<sub>3</sub> based electrodes, the Turn-Over Frequency (TOF) is calculated as a function of the overpotential. TOF is an intrinsic activity marker of the efficiency of the HER process [143]. It measures the amount of reactant consumed or product formed for the given amount of active catalyst per unit time [144]:

$$TOF = \frac{j}{xnF}$$

where  $j$  is the measure current density [A],  $x$  is equal to 2 and is the transferred electron number when a molecule of H<sub>2</sub> is produced,  $n$  is the moles number [moles] and  $F$  is the Faraday constant. Figure 4.7 c shows the TOF as a function of overpotential. The TOF of WO<sub>3</sub> based electrode at  $\eta$  is about the same (the value are listed in Table 4.1), thus confirming that the only relevant difference in HER activity between the WO<sub>3</sub> based electrode is the potential at which the HER starts.

The electrochemical HER parameters of WO<sub>3</sub>\_A60 electrode are reported in Table 4.3 for a comparison with data reported in literature for WO<sub>3</sub> based electrodes. Our electrode shows the lower overpotential, thus confirming the promising HER performances of h-WO<sub>3</sub>/m-WO<sub>3</sub> phase-junction based nanostructures. The presence of two crystal phases at comparable extents could be responsible for this advantageous performance.

	$\eta$ (mV)	Tafel slope (mV/dec)	C <sub>dl</sub> (mF)	ECSA (cm <sup>2</sup> )	TOF @ $\eta$ (mHz)	Ref.
WO <sub>3-x</sub> nanoplates on carbon nanofibers	185	89	-	-	-	112
WO <sub>3</sub> @NPRGO	225	87	-	-	-	118
WO <sub>3</sub> ·H <sub>2</sub> O nanoplates	300	97	-	-	-	145
Ag-WO <sub>3</sub>	207	52.4	54.92	-	-	146
WS <sub>2</sub> -WC-WO <sub>3</sub>	312	59	11.8	295	20	128
WS <sub>2</sub> /WO <sub>3</sub> heterostructure	395	50	-	-	-	129
h-WO <sub>3</sub> /m-WO <sub>3</sub> nanorods	170	106	2.98	100	15	Our work

Table 4.3: Comparison between electrochemical HER parameters for WO<sub>3</sub> based nanostructured reported in literature and our data [133].

#### 4.4 Effect of the hexagonal/monoclinic phase junction presence

To better understand the effect of hexagonal/monoclinic phase junction formation in WO<sub>3</sub> HER catalytic activity, Mott-Schottky analysis was carried out, in 1 M H<sub>2</sub>SO<sub>4</sub> aqueous solution, for the study of the band bending of the semiconductor at the liquid-semiconductor interface. The Mott Schottky relation can be obtained by using the model of a parallel plate capacitor as follow [147-150]:

$$\frac{1}{C^2} = \frac{2}{\varepsilon_0 \varepsilon_r e N_d} \left( E - E_{FB} - \frac{kT}{e} \right) \quad (4.6)$$

where  $C$  is the space region capacitance,  $\varepsilon_0$  is the permittivity of the free space,  $\varepsilon_r$  is the dielectric constant of the semiconductor, which is 50 for WO<sub>3</sub> [151],  $e$  is the electron charge,  $N_d$  is the donor concentration in cm<sup>-3</sup>,  $E_{FB}$  is the flat band potential,  $k$  is the Boltzmann constant and  $T$  is the temperature. WO<sub>3</sub> based electrodes were characterized by measuring their capacitance as a function of applied potential [147-149]. The typical Mott-Schottky plot ( $C^{-2}$  vs applied potential) is shown in Figure 4.8a. A linear trend from -1.1 V to -0.7 V vs SCE is shown for WO<sub>3</sub>\_NA, WO<sub>3</sub>\_A30, and WO<sub>3</sub>\_A90 electrodes and from -0.5 V to -0.4 V for WO<sub>3</sub>\_A60 electrode.

According to Eq. 4.6, the flat band potential  $E_{FB}$  and the donor density  $N_d$  are calculated as x axis intercept and slope from the linear part of the plot and are reported in Figure 4.8 b (filled and hollow spheres respectively) [147-150]. The minimum  $E_{FB}$  value (-0.5V) is obtained for WO<sub>3</sub>\_A60 electrode, for which the lower  $N_d$  ( $2.6 \times 10^{18}$  cm<sup>-3</sup>) is recorded (do note inverse Y scales for  $E_{FB}$  and  $N_d$  in Figure 4.8 b). The  $E_{FB}$  is related to the band bending at the liquid-semiconductor interface in equilibrium conditions, so by combining this value with the open circuit potential (OCP) of each WO<sub>3</sub> based electrodes (reported in Table 4.4) the actual band-bending with respect to H<sup>+</sup>/H<sub>2</sub> level can be defined. The results of such exercise are reported in Figure 4.8 c. WO<sub>3</sub>\_A60 electrode shows the lowest band bending as well as the lowest depletion region, which leads to the lowest energy barrier for electrons moving from WO<sub>3</sub> towards the electrolyte (depicted as the light blue region).



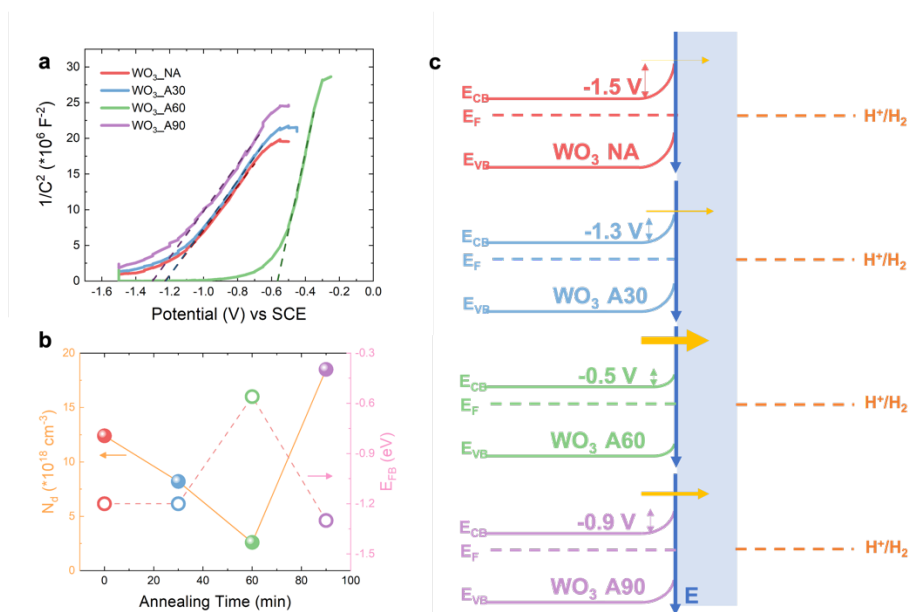


Figure 4.8: (a) Mott-Schottky plot and (b) related donor concentration ( $N_d$ ) and flat band potential ( $E_{FB}$ ) of WO<sub>3</sub>\_NA (red), WO<sub>3</sub>\_A30 (blue), WO<sub>3</sub>\_A60 (green) and WO<sub>3</sub>\_A90 (violet) electrodes; (c) scheme of relative position of energy levels and band bending related to H<sup>+</sup>/H<sub>2</sub> energy level at semiconductor-liquid interface for each WO<sub>3</sub> based electrodes. The thickness of the yellow arrows denotes the magnitude of the cathodic current [133].

	$E_{FB}$ (V)	OCP (V)	Band bending (V)	$N_d$ ( $\times 10^{18} \text{ cm}^{-3}$ )
<b>WO<sub>3</sub>_NA</b>	-1.2	-0.3	-1.5	12.4
<b>WO<sub>3</sub>_A30</b>	-1.2	-0.1	-1.3	8.2
<b>WO<sub>3</sub>_A60</b>	-0.6	0.1	-0.5	2.6
<b>WO<sub>3</sub>_A90</b>	-1.3	0.4	-0.9	18.5

Table 4.4: Results of Mott Schottky analyses for WO<sub>3</sub>\_NA, WO<sub>3</sub>\_A30, WO<sub>3</sub>\_A60 and WO<sub>3</sub>\_A90 electrodes [133].

A larger electron flux is thus expected for this sample (as drawn by the thickness of yellow horizontal arrows) in comparison to others. Lower band bending corresponds to a lower  $\eta$  for HER, thus explaining the better catalytic activity of the WO<sub>3</sub>\_A60 electrode.

### 4.5 The HER mechanism

Morphological and electrochemical analyses of WO<sub>3</sub> based electrodes allow to define a model which can explain the better catalytic performance of the WO<sub>3</sub>\_A60 electrode. The evidence obtained so far can be summarized as follows:

- (i) XRD and TEM analyses demonstrates the h-/m-WO<sub>3</sub> phase junction formation. The  $W_m\%$  strongly depends on annealing time, as well as the monoclinic crystallites size;
- (ii) WO<sub>3</sub>\_NA, WO<sub>3</sub>\_A30, WO<sub>3</sub>\_A60 and WO<sub>3</sub>\_A90 electrodes show polarization curves with the same trend (Figure 4.6 a), but polarization curve of WO<sub>3</sub>\_A60 is shifted towards lower potentials by achieving lower  $\eta$  of 170 mV at 10 mA/cm<sup>2</sup>;
- (iii) Tafel slopes and TOF values of WO<sub>3</sub> based electrodes suggest that the HER mechanism is the same regardless of the m-WO<sub>3</sub> and h-WO<sub>3</sub> content and so on the phase junction formation. Moreover, Tafel slopes values suggest that the HER mechanism is limited by the H<sup>+</sup> adsorption mechanism on the active material surface;
- (iv) WO<sub>3</sub>\_NA, WO<sub>3</sub>\_A30, WO<sub>3</sub>\_A60 and WO<sub>3</sub>\_A90 electrodes show similar  $C_{dl}$  and ECSA thus ruling out the active surface role in the HER catalytic activity and in the phase junction formation;
- (v) EIS analysis shows the same quasi-negligible electrode substrate role for each WO<sub>3</sub>-based electrodes, and the possibility to ascribe the superior HER activity of WO<sub>3</sub>\_A60 electrode to a lowering of the total Faradic resistance of the HER mechanism caused by the m-WO<sub>3</sub> and h-WO<sub>3</sub> phase junction formation.
- (vi) Mott-Schottky analyses highlight the energy level structure at semiconductor-liquid interface, by revealing the smallest band bending for the WO<sub>3</sub>\_A60 electrode, which leads to the highest

cathodic current flux towards the electrolyte and so to the lowest  $\eta$  for the activation of the HER process.

Taking into account these considerations, a schematic representation of the correlation between the enhancement of the HER activity and the formation of an m- and h-WO<sub>3</sub> phase (lilac and brown part respectively) junction is proposed in Figure 4.9. The thermal treatment leads to a stable phase junction formation in correspondence of the grain boundary between h- and m-WO<sub>3</sub> crystallites (red lines in Figure 4.9) without affecting the morphology of WO<sub>3</sub>-based nanostructures, as shown by SEM images in Figure 4.3. As depicted in Figure 4.9, the concentration of h-/m-WO<sub>3</sub> phase junctions depends on the annealing time and so on the  $W_h\%$  and the  $W_m\%$ . The WO<sub>3</sub>\_A60 powder shows similar  $W_h\%$  and  $W_m\%$  values (see Figure 4.4 b) and similar h- and m-WO<sub>3</sub> crystallites sizes (see Figure 4.4c), which should lead to a higher density of phase junctions. On the contrary, the WO<sub>3</sub>\_NA, the WO<sub>3</sub>\_A30 and the WO<sub>3</sub>\_A90 powder show a lower (or zero) phase junctions density, because of prevalence of one crystal phase. At the semiconductor-liquid interface, the phase junctions affects the total band bending (Figure 4.8c). The lower band bending results in a higher cathodic current, and so in a higher concentration of available electrons useful to lower the total Faradaic resistance. The phase junction interface becomes the main site for H<sup>+</sup> adsorption, and for H<sub>2</sub> production thanks to largely available electrons, as shown in Figure 4.9. The presence of a high concentration of phase junction lowers the required potential for HER activation, and so  $\eta$ , thus confirming our experimental evidence related to WO<sub>3</sub>\_A60.

### 4.6 Conclusion

In conclusion, h-/m-WO<sub>3</sub> phase junction has been successfully fabricated in hydrothermal synthesized WO<sub>3</sub> nanorods, annealed at 400 °C for 30, 60 and 90 min. The hexagonal and monoclinic content strongly depends on annealing time as well as the dimension of as formed monoclinic crystallites. In particular, the 60 min annealed WO<sub>3</sub> powders show a monoclinic content of 56 % and comparable monoclinic and hexagonal crystallites sizes.

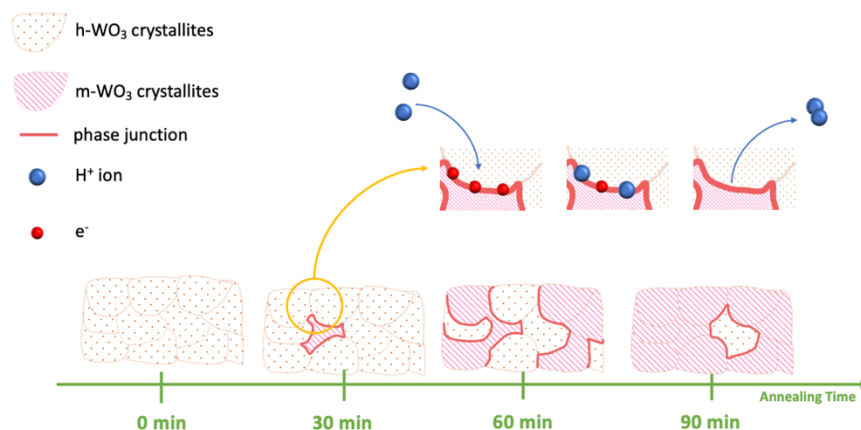


Figure 4.9: Schematic representation of the HER mechanism in correspondence of the h-/m-WO<sub>3</sub> phase junction (brown and pink area). The HER predominantly occurs at the phase junction interface (red lines), in which many electrons (red balls) are available for the adsorption of H<sup>+</sup> (blue balls) and production of H<sub>2</sub> [133].

This sample exhibits exceptional catalytic activity for HER in 1 M H<sub>2</sub>SO<sub>4</sub> electrolyte with an overpotential of 170 mV at 10 mA/cm<sup>2</sup>. The advantage of this h-/m-WO<sub>3</sub> combination can be ascribed to the formation of numerous phase junction interfaces at which the HER can occur faster thanks to larger availability of electrons, as demonstrated by Tafel, EIS and Mott-Schottky analyses and ECSA and TOF determination. The obtained catalyst represents a potential candidate for Pt-free electrochemical production of clean hydrogen in acid solutions, by paving the way to a further study and engineering of simple phase junction formation in semiconductor for Pt-free HER application.



# Chapter 5

## WO<sub>3</sub> nanorods for electrochemical energy storage

*Electrochemical energy storage devices, such as batteries and supercapacitors (electrochemical double layer capacitors and pseudocapacitors) have aroused a great interest in scientific community, since the efficient use of green and renewable energy sources requires high capacitive and long-lifetime devices. Among them, pseudocapacitors materials represent suitable candidates for development of high capacitance energy storage devices. Transition metal oxide nanostructures are commonly used for development of pseudocapacitor since electrochemical reactions occurs at nanometer solid-liquid interface. In this chapter, the synthesis of WO<sub>3</sub> nanorods and hierarchical urchin-like nanostructures by hydrothermal method and the subsequently calcination processes will be described. Morphology and crystal phase of WO<sub>3</sub> nanostructures investigation by scanning electron microscopy (SEM) and X-ray diffraction (XRD) will be presented, as well as the energy storage performances of WO<sub>3</sub> nanostructures-based electrodes, evaluated by cyclic voltammetry (CV) and galvanostatic charge-discharge (GCD) tests. The experimental results show that promising values of specific capacitance (632 F/g at 5 mV/s and 466 F/g at 0.5 A/g) are obtained when pure hexagonal crystal phase WO<sub>3</sub> hierarchical urchin-like nanostructures are used. A detailed modeling of surface and diffusion-controlled mechanisms in energy storage process will be given. Further, the realization of an asymmetric supercapacitor as proof of concept will be presented. WO<sub>3</sub> urchin-like nanostructures and a graphene paper electrode are used as cathode and anode respectively, revealing the highest energy density (134 W\*h\*Kg<sup>-1</sup>) at power density of 135 W\*Kg<sup>-1</sup> and the highest power density (13500 W\*Kg<sup>-1</sup>) at energy density of 26 W\*h\*Kg<sup>-1</sup>. The presented correlation among physical features and electrochemical performances of WO<sub>3</sub> nanostructures provides a solid base for further developing energy storage devices based on transition metal oxides.*

### 5.1 Electrochemical energy storage

In the global panorama, the use of green and renewable source of energy aroused a great interest in scientific community, to solve the problems related to the CO<sub>2</sub> emission and to the finite supply of fossil fuels. In this scenario, the development of efficient energy storage devices is crucial to efficiently use these new energy sources. In the panorama of energy storage systems, supercapacitors (Electrical Double Layer Capacitors and pseudocapacitor) and batteries are used depending on the power and energy density required by application. A schematic of the energy storage mechanism in supercapacitors and batteries is shown in Figure 5.1. Batteries are the choice when high energy density is required, since energy storage mechanism is due to redox reactions involving almost all active material [152], while Electrical Double Layer Capacitors (EDLC) represent a promising solution in high power density applications, since the electrochemical reactions driving the energy storage mechanism occur at the surface of active material [153]. To overcome the differences between EDLC and batteries a new device, called pseudocapacitor, has been developed. Pseudocapacitors are typically obtained by using high porous transition metal oxide-based electrodes [154, 155]. The charge storage mechanism of a pseudocapacitor is based on fast faradic reactions occurring at or near the electrode surface and leading to high levels of charge storage [156-157]. Indeed, a pseudocapacitor works as a battery, but redox reactions occur at the surface, like in an EDLC [154], thus joining intermediate power and energy density of both kinds of devices. This behavior results in a combination of diffusion and surface limited charge storage mechanisms, which can be individuated by cyclic voltammetry analysis [158]. Figure 5.2 shows the Ragone plot in which EDLC, batteries and pseudocapacitors are reported as a function of supplied power and energy density.

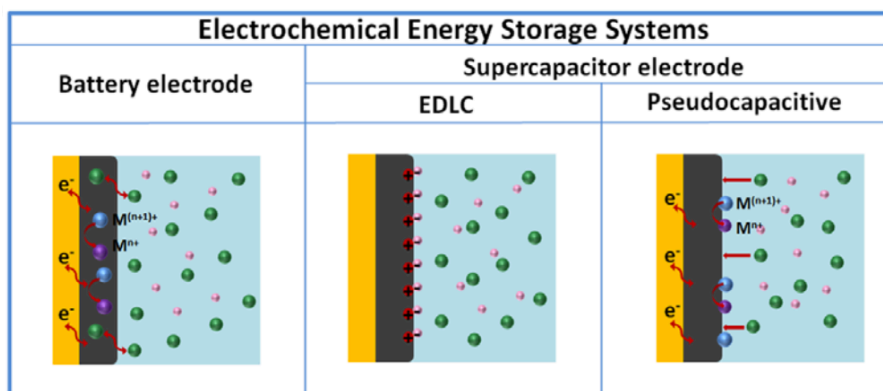


Figure 5.1: Schematic of the energy storage mechanism of batteries and supercapacitors (EDLC and pseudocapacitors) [154].

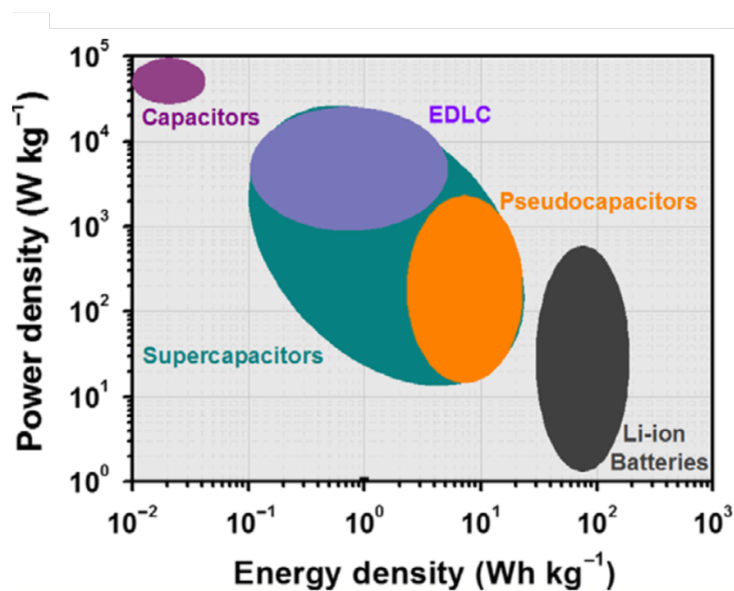


Figure 5.2: Ragone plot (specific power density against specific energy density) of energy storage devices [154]



### 5.1.1 Overview on WO<sub>3</sub> as pseudocapacitor

The most used materials for pseudocapacitor electrodes are transition metal oxides, among which WO<sub>3</sub> has emerged as favorable material thanks to its properties. Indeed, WO<sub>3</sub> is an *n*-type semiconductor with high electrochemical stability in acidic environments, high theoretical electronic conductivity ( $10 \cdot 10^{-6} \text{ s} \cdot \text{cm}^{-1}$ ), high intrinsic density ( $>7 \text{ g} \cdot \text{cm}^{-3}$ ) and high specific capacitance ( $C_s$ ) [159]. Several WO<sub>3</sub> nanostructures for energy storage application can be found in literature, with a very ample range of  $C_s$  [62, 160, 161]. Low cost and simple hydrothermal method can produce hexagonal WO<sub>3</sub> nanorods [162] with  $C_s$  of 538 F/g at 5 mV/s, hexagonal WO<sub>3</sub> nanofibers [45] with  $C_s$  of 436 F/g at 1 A/g, hexagonal WO<sub>3</sub> nanostructures [130] with  $C_s$  of 377 F/g at 2 mV/s. A careful and reproducible determination of specific capacitance is compulsory, linked to a detailed morphological and crystallographic characterization, to better understand the ultimate performance for energy storage of this material. Among the effective strategies to further improve electrochemical properties of WO<sub>3</sub>, crystal phase modulation can be effective, since the hexagonal crystalline structure of WO<sub>3</sub> is widely claimed in literature as the most suitable for electrochemical charge storage due to favorable H<sup>+</sup> intercalation-release pathways [130].

In the next paragraphs a detailed structural and electrochemical characterization of hexagonal WO<sub>3</sub> nanostructures synthesized by hydrothermal method will be reported. A careful protocol for electrode realization and evaluation of charge storage and release will be described with a modeling of storage process in terms of surface and diffusion-controlled mechanisms. At last, an asymmetric supercapacitor will be realized by using WO<sub>3</sub> nanostructures electrode as cathode and graphene paper (GP) electrode as anode.

### 5.2 Electrode realization and characterization

Hexagonal WO<sub>3</sub> nanorods are synthesized as reported in Chapter 2, without further post-synthesis processing (denoted as WO<sub>3</sub>\_AsPrep). Some samples underwent a calcination process on a hot plate at 70°C for 40 minutes or at

400 °C for 60 minutes (denoted as WO<sub>3</sub>\_Ann70 or WO<sub>3</sub>\_Ann400, respectively). The obtained WO<sub>3</sub> based nanostructures were used for the realization of pastes (20 mg of nanostructures powder, 0.1 ml of Nafion and 4 ml of deionized water). Part of these pastes was filtered by a 1.2 µm filter to select only the nanorods morphology. Graphene paper (GP, 2x1 cm<sup>2</sup>, Sigma Aldrich, 240 µm thick) was used as substrates and the electrodes are produced by drop casting the obtained WO<sub>3</sub>-based pastes. The acronyms “NF” and “F” are used for electrodes prepared with the non-filtered and filtered WO<sub>3</sub> based pastes, respectively. A Mettler Toledo MX5 Microbalance (sensitivity: 0.01 mg) was used to measure the mass of electrode (substrate + WO<sub>3</sub> nanostructures) and of bare substrate.

The morphological analyses were carried out by a scanning electron microscope (SEM) Gemini Field Emission SEM Carl Zeiss SUPRATM 25 (FEG-SEM, Carl Zeiss Microscopy GmbH, Jena, Germany) in In-LENS mode. Figure 5.3 shows low (a, c, e) and high (b, d, f) SEM images of (a-b) WO<sub>3</sub>\_AsPrep, (c-d) WO<sub>3</sub>\_Ann70, and (e-f) WO<sub>3</sub>\_Ann400 powders, thus demonstrating that the different thermal treatments does not change the morphology of the WO<sub>3</sub> based powder. WO<sub>3</sub> powder appears as composed of large or small aggregates of nanorods if NF or F solution is used, respectively, as seen by low magnification SEM images in Figure 5.4 a and b. The NF WO<sub>3</sub> powder is characterized by urchin-like agglomerates (about 3 µm in size) of nanorods (Figure 5.4 c), stacked on top of a thick WO<sub>3</sub> nanorods film (Figure 5.4 d). Instead, the F WO<sub>3</sub> powder shown in Figure 5.4 b does not have urchin-like agglomerates but only oddly aligned nanorods 0.5-1 µm long and 50 nm large, as high magnification SEM images in Figure 5.4 e shows.

Film structure was analyzed through XRD using a Smartlab Rigaku diffractometer, in grazing incidence 0.5°, equipped with a rotating anode of Cu Kα radiation operating at 45 kV and 200 mA. The scans were acquired from 10° to 70° with a step of 0.02°<sup>5</sup>. Figure 5.4 f shows the XRD patterns of WO<sub>3</sub>\_AsPrep, WO<sub>3</sub>\_Ann70 and WO<sub>3</sub>\_Ann400 powders compared with XRD patterns of hexagonal (PDF #89-4476) and monoclinic (PDF #75-2187) WO<sub>3</sub>,

---

<sup>5</sup> These analyses were carried out in collaboration with Prof. Graziella Malandrino at the Bio-nanotech Research and Innovation Tower (BRIT) laboratory of the University of Catania

respectively. The XRD pattern of the WO<sub>3</sub>\_AsPrep powders is not well defined, with little pronounced peaks at typical positions of hexagonal phase, thus suggesting a poor crystalline nature of these powders, and a bump at around  $2\theta = 20.00^\circ$ , which can be associated with an earlier unknown nonstoichiometric phase [68]. Instead, the typical diffraction peaks of hexagonal structure are shown in the XRD pattern of WO<sub>3</sub>\_Ann70, which

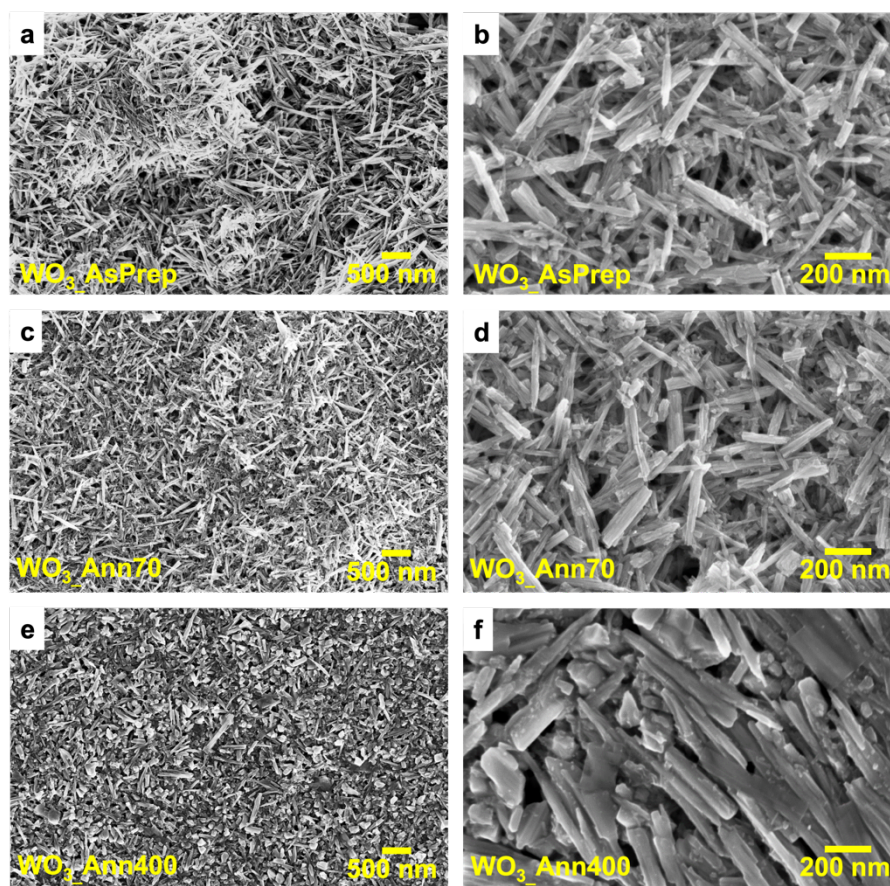


Figure 5.3: Low (a-c-e) and high (b-d-f) magnification SEM images of (a-b) WO<sub>3</sub>\_AsPrep, (c-d) WO<sub>3</sub>\_Ann70, (e-f) WO<sub>3</sub>\_Ann400. Reproduced by [67]

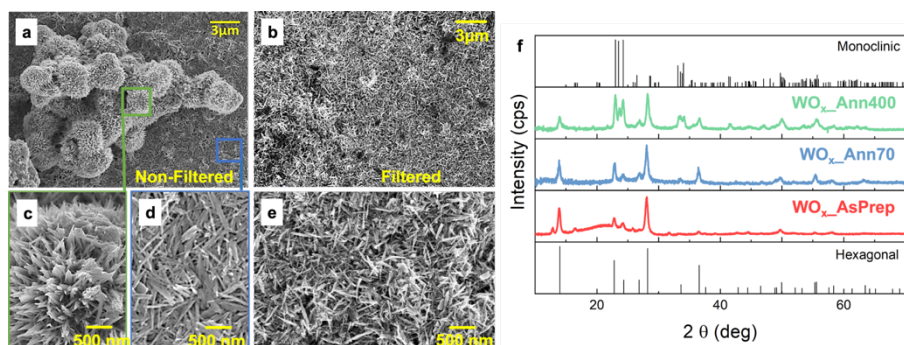


Figure 5.4: low magnification SEM images of (a) NF and (b) F WO<sub>x</sub> powder; high resolution SEM images of (c) urchin-like nanostructures and (d) nanorods presents in the NF WO<sub>3</sub> powder and (e) nanorods present in the F WO<sub>3</sub> powder; (f) XRD patterns of WO<sub>3</sub>\_AsPrep, WO<sub>3</sub>\_Ann70 and WO<sub>3</sub>\_Ann400 powders compared with the hexagonal and monoclinic characteristic patterns [67].

appear at  $2\theta = 14.00^\circ, 24.36^\circ, 26.84^\circ, 28.22^\circ, 33.62^\circ, 36.58^\circ, \text{ and } 49.95^\circ$ , thus confirming its pure hexagonal phase [64]. Moreover, peaks clearly related to monoclinic crystal structure appear ( $2\theta = 23.00^\circ, 23.50^\circ, 24.28^\circ, 33.12^\circ, 33.54^\circ, 33.84^\circ, 34.04^\circ, 49.74^\circ, 55.71^\circ$ ) when the WO<sub>3</sub> powder is annealed at 400°C, by suggesting a partial phase transition and the coexistence of hexagonal and monoclinic WO<sub>3</sub> phases (*h*-WO<sub>3</sub> and *m*-WO<sub>3</sub>) in WO<sub>3</sub>\_Ann400.

In the next paragraph, the as characterized WO<sub>3</sub> based electrodes will be electrochemically analyzed for the evaluation of the energy storage performance as a function of the crystal structure (effect of thermal treatment) and morphology (effect of filtering process) of WO<sub>3</sub> based nanostructures.

### 5.3 Specific capacitance quantification

The electrochemical measurements were performed at room temperature by using a potentiostat (VersaSTAT 4, Princeton Applied Research, USA) and a three-electrode setup with a platinum counter electrode, a saturated calomel electrode (SCE) as reference, WO<sub>3</sub> casted GP as working electrode (10x10 mm immersed area), in 1 M H<sub>2</sub>SO<sub>4</sub> supporting electrolyte. Cyclic voltammetry (CV) curves were recorded at different scan rates (5 to 100 mV/s) in the -0.5 V to 0 V vs SCE potential range and galvanostatic charge-discharge (GCD)

tests were conducted at different current densities (0.5 to 5 A/g) in the potential range -0.5÷0 V. Figure 5.5 a shows CV curves (from -0.5 V to 0 V at 50 mV/s) of electrodes obtained by using the NF (solid line) and F (dotted line) WO<sub>3</sub>\_AsPrep, WO<sub>3</sub>\_Ann70 and WO<sub>3</sub>\_Ann400 pastes based electrodes (red, blue, and green lines respectively). Electrodes obtained with filtered (F) pastes show similar quasi-rectangular CV curves, with a relatively small area under the CV curve. Larger area are observed when using NF WO<sub>3</sub> pastes. The largest CV curve is obtained for the WO<sub>3</sub>\_Ann70 powder, thus suggesting that WO<sub>3</sub> with pure hexagonal crystal phase and urchin-like nanostructures and nanorods morphologies gives the best performances for energy storage application.

Basing on the above consideration, the NF WO<sub>3</sub>\_Ann70 electrode results the most appropriate for investigating energy storage mechanism. Figure 5.5b shows CV curves performed at different voltage scan rates (from 5 to 100 mV/s). CV curves of NF WO<sub>3</sub>\_AsPrep and WO<sub>3</sub>\_Ann400 electrodes, and of F WO<sub>3</sub>\_AsPrep, WO<sub>3</sub>\_Ann70 and WO<sub>3</sub>\_Ann400 electrodes are reported in Figure A5.1. All WO<sub>3</sub> based electrodes show similar trends for CV curves, despite of the area under the curve. No obvious redox peaks can be observed in the CV curves of Figure 5.5 b and the curves exhibit the typical shape described for WO<sub>3</sub> based electrode [62, 130, 161, 163-165]. CV curves significantly change by increasing the potential scan rate from 5 to 100 mV/s tending to a squarer shape. Indeed, the lower ion intercalation at higher scan rates could results in a weakening of the diffusion-controlled storage mechanisms, thus leading to charge storage driven by surface contributions. The coexistence of diffusion and surface limited contributions results in a pseudocapacitive behavior, as expected [45, 130, 152, 158]. Moreover, the absence of redox peaks in CV curves of Figure 5.5b and the quasi-rectangular shape indicate the presence of reversible and fast surface redox reactions at constant rate. The Specific Capacitance (or pseudocapacitance) ( $C_s$ ) can be defined from CV curves as follows [156]:

$$C_s = \frac{\int IdV}{mv\Delta V} \quad (5.1)$$

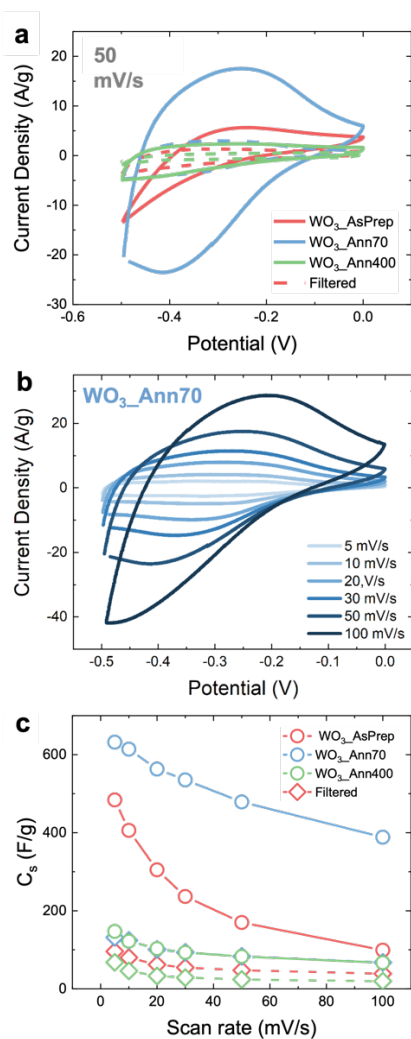


Figure 5.5: (a) CV curves obtained at 50 mV/s of NF (solid lines) and F (dotted lines) WO<sub>3</sub>\_AsPrep, WO<sub>3</sub>\_Ann70 and WO<sub>3</sub>\_Ann400 pastes electrodes; (b) CV curves of WO<sub>3</sub>\_Ann70 electrode obtained at different scan rates; (c) C<sub>s</sub> as a function of scan rate obtained from CV curves of NF (solid lines) and F (dotted lines) WO<sub>3</sub>\_AsPrep, WO<sub>3</sub>\_Ann70 and WO<sub>3</sub>\_Ann400 pastes electrodes. The potential is measured versus SCE. Reproduced by [67].

where  $I$  is the measured current (mA),  $V$  is the measured potential (V),  $m$  is the active WO<sub>3</sub> mass (mg),  $v$  is the voltage scan rate (V/s) and  $\Delta V$  is the potential range (V). Figure 5.5 c shows the C<sub>s</sub> value as a function of voltage

scan rate of NF (circled symbols) and F (rhombohedral symbols) WO<sub>3</sub>\_AsPrep, WO<sub>3</sub>\_Ann70 and WO<sub>3</sub>\_Ann400 pastes-based electrodes (red, blue, and green symbols, respectively). The highest C<sub>s</sub> values are obtained for the NF WO<sub>3</sub>\_Ann70 (632 F/g at 5 mV/s), as expected, while the NF WO<sub>3</sub>\_AsPrep and WO<sub>3</sub>\_Ann400 paste-based electrodes show low C<sub>s</sub>, thus confirming the poor energy storage activity of WO<sub>3</sub> nanostructures with poor crystalline nature or with mixture of crystalline phases. The high C<sub>s</sub> value obtained for the WO<sub>3</sub>\_Ann70 electrode can be ascribed to the high crystalline nature and the pure hexagonal structure, which presents favorable H<sup>+</sup> intercalation-release pathways [130]. It should be emphasized that as-prepared WO<sub>3</sub> nanorods, even if with hexagonal peaks in XRD spectrum, do not give the best results and a soft annealing up to 70°C is needed to greatly improve the storage efficiency. On the other hand, a strong calcination (as at 400°C) is detrimental because the hexagonal phase starts to be lost. Also, the presence of urchin-like nanostructures affects the C<sub>s</sub> since this morphology contributes to increase the porosity of the electrochemical active film. Such a porosity may improve the mass transport of electrolyte ions to the entire electrochemical active surface, useful when high power densities are required because of improvement of available electrochemical active surface [152]. The C<sub>s</sub> of electrodes obtained from F WO<sub>3</sub> pastes are very low compared to those obtained from NF WO<sub>3</sub> pastes. This is probably due to the low porosity of the dense film of WO<sub>3</sub> nanorods, as shown in SEM images of Figure 5.4 b and e. All the electrodes show the same trend of C<sub>s</sub> as a function of scan rate (Figure 5.5 c): as the scan rate increases, the C<sub>s</sub> decreases. Such a feature of C<sub>s</sub> confirms the pseudocapacitor behavior, for which diffusion and surface-controlled storage mechanisms act at the same time depending on the voltage scan rate: at lower scan rate, both mechanisms are active which results in higher C<sub>s</sub>, while at higher scan rate only surface mechanisms are active inducing a C<sub>s</sub> decrease.

C<sub>s</sub> calculated from CV curves represents an approximation of the real value, whereby the electrochemical activity of WO<sub>3</sub>\_Ann70 based electrode is more in-depth investigated by performing robust electrochemical analysis to unveil its energy storage activity through GCD analysis, which studies the electrochemical galvanostatic charge-discharge mechanism to define accurately the Specific Capacitance and the internal series resistance of the

electrode [152, 153, 154, 166]. Figure 5.6 a shows the GCD curves obtained at different current densities (from 0.5 to 10 A/g) in the voltage range of -0.5 to 0 V: the discharge time of the hexagonal WO<sub>3</sub> nanostructures significantly decreases as the current density increases, as expected. The charge and discharge curves are symmetric, indicating poor energy loss, high reversibility and high coulombic efficiency during the charge and discharge process [155, 167]. Moreover, the GCD curves display a non-linearity at different current densities, thus suggesting that surface and diffusion-limited processes occur at the interface between electrolyte and electrode [161]. Moreover, the GCD curves show an IR drop related to the internal resistance of the electrode (see arrows in Figure 5.6 a) which increases as the current density increases, thus suggesting that at higher current density fewer active sites are accessible for the electrochemical reaction [164]. The resulting equivalent series resistance

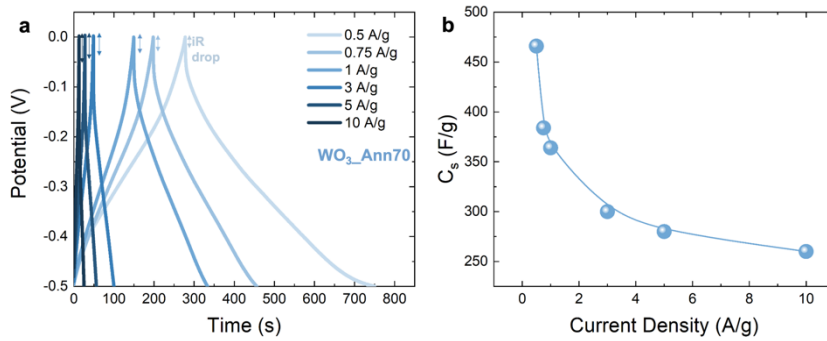


Figure 5.6: (a) GCD curves of NF WO<sub>3</sub>\_Ann70 paste-based electrode obtained in 1 M H<sub>2</sub>SO<sub>4</sub> solution at different current density. The iR drop is indicated for each GCD curve; (b) C<sub>s</sub> as a function of current density obtained from the GCD curves; potential measured versus SCE [67].

are 30, 28, 27, 23, 20 and 16 Ω at current densities of 0.5, 0.75, 1, 3, 5 and 10 A/g. C<sub>s</sub> can be calculated also from GCD curve as follow [156]:

$$C_s = \frac{It_s}{m\Delta V} \quad (5.2)$$

where  $I$  is the applied current (mA),  $t_s$  is the discharge time,  $m$  is the active WO<sub>3</sub> mass (mg), and  $\Delta V$  is the potential range (V). Figure 5.6 b shows the related C<sub>s</sub>: as the current density increases, the C<sub>s</sub> decreases from 466 F/g at



0.5 A/g to 260 F/g at 5 A/g, which are slightly lower than results previously obtained from CV curves because of the chosen current density [166] (lower current densities give higher C<sub>s</sub>), but in accordance with them.

In the next paragraph, a detailed study of the CV curves of the WO<sub>3</sub> electrodes is performed, to understand the energy storage mechanism as a function of the morphology and of the crystal structure.

### 5.4 Investigation of energy storage mechanism

#### 5.4.1 Surface and diffusion limited mechanisms

CV is a powerful tool for the electrochemical behavior comprehension since CV analyses allow to define the suitable potential range for electrochemical characterization and the type of electrochemical reactions (diffusion or surface limited) [153]. To study the role of crystalline quality and morphology of WO<sub>3</sub> nanostructures in energy storage activity, the CV curves were in deep analyzed and described in terms of surface and diffusion-limited contribution. Generally, at fixed potential  $V$  the current ( $i$ ) depends on the scan rate ( $\nu$ ) as follows [130]:

$$i(V) = a\nu^b \quad (5.3)$$

where  $a$  and  $b$  are parameters. At the electrode/electrolyte interface, if the charge exchange is limited by diffusion of ions (as in ideal battery),  $b$  is equal to 0.5, while if the charge exchange is limited by surface process (as in ideal EDLC), then  $b$  is equal to 1 [130, 158]. By considering the CV curves of NF WO<sub>3</sub>\_AsPrep and WO<sub>3</sub>\_Ann70 and F WO<sub>3</sub>\_AsPrep pastes-based electrodes performed at 5, 10, 20 and 30 mV/s (Figure A5.1 a, Figure 5.5 b, and Figure A5.1 b respectively), the cathodic current values at fixed potentials are taken in consideration for the determination of  $b$  value. From the linear fits of  $\ln(i)$  as a function of  $\ln(\nu)$ , shown in Figure 5.7,  $b$  value is extracted and reported as a function of potential in Figure 5.8. Figure 5.8 a shows the comparison

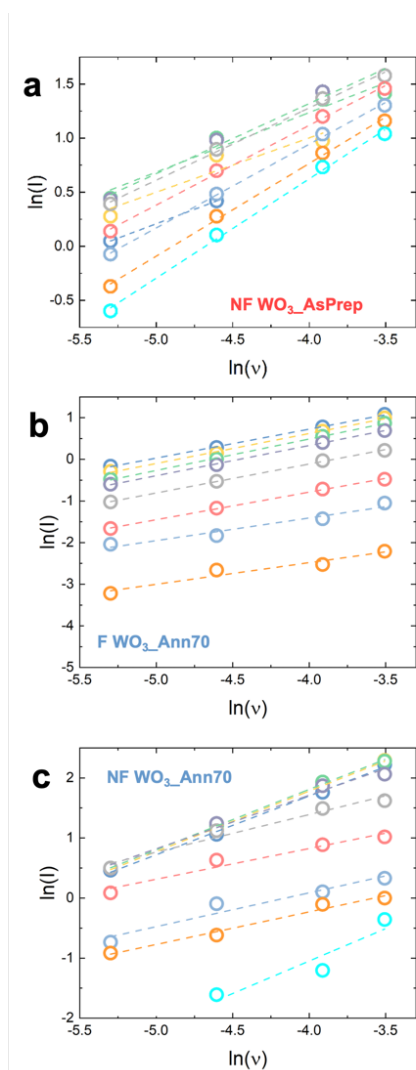


Figure 5.7: plots of  $\ln(I)$  as a function of  $\ln(v)$  at different potential values obtained by considering CV curves of (a)  $\text{NF WO}_3\text{-AsPrep}$ , (b)  $\text{F WO}_3\text{-Ann70}$  and (c)  $\text{WO}_3\text{-Ann70}$  paste-based electrodes at 5, 10, 20 and 30 mV/s at fixed potentials. The b value can be determined from the linear fit of curves obtained at fixed potential. Reproduced by [67].

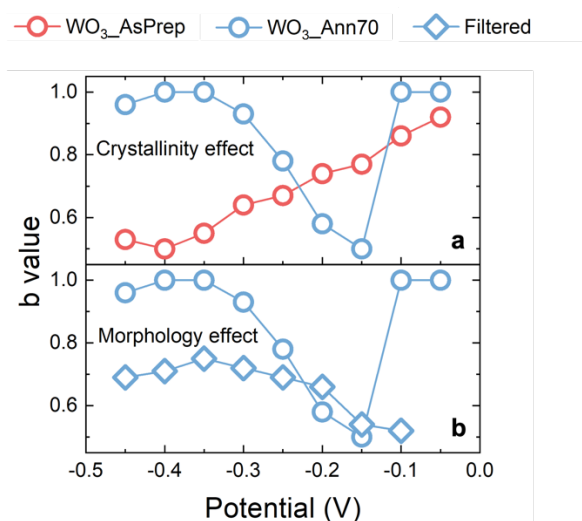


Figure 5.8: Comparison of  $b$  values obtained for (a) NF WO<sub>3</sub>\_AsPrep and WO<sub>3</sub>\_Ann70 pastes electrodes and (b) NF and F WO<sub>3</sub>\_Ann70 pastes electrodes as a function of applied potential at 5 mV/s. The potential is measured versus SCE. Reproduced by [67].

between the obtained  $b$  values (at 5 mV/s) as a function of potential for NF WO<sub>3</sub>\_AsPrep and WO<sub>3</sub>\_Ann70 electrodes (red and blue circles respectively) to highlights the role of crystalline structure in energy storage. The  $b$  value ranges between 0.5 and 1, thus confirming the pseudocapacitor behavior of tested WO<sub>3</sub> based electrodes. The pure hexagonal crystalline structure of WO<sub>3</sub>\_Ann70 electrode contributes to improve the surface role at more negative potentials and at potentials close to 0 V ( $b$  tends to 1), while the diffusion contributions are well present at around -0.2 to -0.1 V ( $b$  tends to 0.5). This results in a clearly potential region separation for the activation of surface and diffusion-limited processes. The low crystallinity of the WO<sub>3</sub>\_AsPrep electrode leads to a mixture of surface and diffusion contribution to almost all intermediate potentials, with a  $b$  value that gradually switches from 0.5 at -0.5 V to 1 at 0 V. Figure 5.8 b describes also the role of WO<sub>3</sub> morphology in the energy storage activity by comparing  $b$  values obtained from CV curves of NF and F WO<sub>3</sub>\_Ann70 paste-based electrodes at 5 mV/s (blue circle and rhombohedral symbols, respectively). The absence of urchin-like nanostructures in F pastes leads to a lowering of surface-limited contributions at all potentials ( $b$  value always lower than 0.8). Taking into

account the above consideration, the better energy storage performances of NF WO<sub>3</sub>\_Ann70 can be ascribed to the activation of surface-limited contributions, which seem to be more effective than the diffusion-limited ones for almost all potentials. The surface-limited contributions are mainly given by the presence of hexagonal urchin-like nanostructures, which, thanks to their morphology, possess a higher wettability, as well as a larger surface area immersed in the electrolyte solution.

#### 5.4.2 Kinetic mechanism of energy storage

The kinetics of electrochemical processes can be studied by applying the model proposed by Dunn et al. [158], which allows to determine diffusion and surface limited current contributions to the measured total current during CV analysis. According to this model, the total current at fixed potential  $I(V)$  depends on the scan rate  $\nu$  as follows [158]:

$$I(V) = k_1\nu + k_2\nu^{1/2} \quad (5.4)$$

where  $k_1$  and  $k_2$  are the coefficients related to surface and diffusion contributions to the total current, respectively. The kinetics analysis described above is applied for low scan rates, to avoid errors due to the polarization and to the ohmic losses occurring at high scan rates [130, 168].  $k_1$  and  $k_2$ , and consequently the diffusion and current contributions, can be calculated, since the Eq. (5.4) can be rewritten as follows:

$$I(V)\nu^{-1/2} = k_1\nu^{1/2} + k_2$$

From the linear fit of  $I(V)\nu^{-1/2}$  as a function of  $\nu^{1/2}$  the surface ( $k_1$ ) and diffusion ( $k_2$ ) contribution can be defined. Figure 5.9 shows the  $I(V)\nu^{-1/2}$  plot as a function of  $\nu^{1/2}$  obtained from CV curves of NF WO<sub>3</sub>\_AsPrep and WO<sub>3</sub>\_Ann70 and the F WO<sub>3</sub>\_AsPrep electrodes performed at 5, 10, 20 and 30 mV/s.

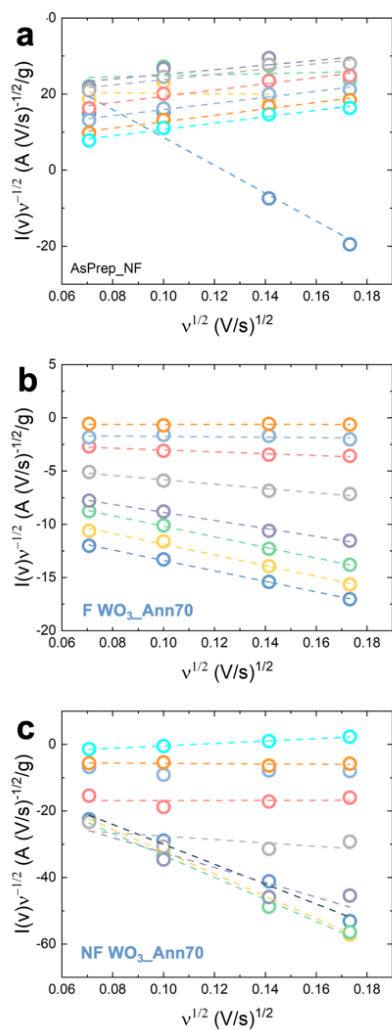


Figure 5.9: plot of  $I(V)v^{-1/2}$  as a function of  $v^{1/2}$  for the determination of surface and diffusion contributes to the total current measured during CV analysis of at (a) NF WO<sub>3</sub>\_AsPrep, (b) F WO<sub>3</sub>\_Ann70 and (c) WO<sub>3</sub>\_Ann70 pastes-based electrodes at 5, 10, 20 and 30 mV/s at fixed potentials. The linear fits allows to determine  $K_1$  and  $K_2$  at each potential. Reproduced by [67].

Figure 5.10 a shows the comparison between surface-limited current contribution ( $I_s$ ) calculated at 5 mV/s as a function of potential for NF WO<sub>3</sub>\_AsPrep and WO<sub>3</sub>\_Ann70 pastes electrodes (red and blue circle

respectively), while Figure 5.10 b shows the comparison between  $I_s$  as a function of potential for NF and F WO<sub>3</sub>\_Ann70 pastes electrodes (blue circle and rhombohedral symbols, respectively).  $I_s$  increases as  $b$  approaches 1, as expected, thus confirming that the better energy storage performances of NF WO<sub>3</sub>\_Ann70 paste electrodes are strictly correlated to the presence of surface-limited mechanisms. The diffusion-limited current contribution ( $I_d$ ) is reported in Figure A5.2.

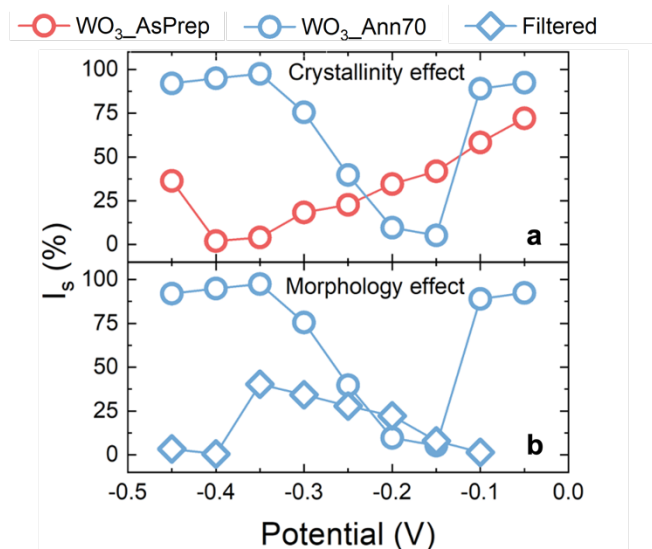


Figure 5.10: Comparison of surface-limited current contribution ( $I_s$ ) for (a) NF WO<sub>3</sub>\_AsPrep and WO<sub>3</sub>\_Ann70 pastes electrodes and (b) NF and F WO<sub>3</sub>\_Ann70 pastes electrodes as a function of applied potential at 5 mv/s. The potential is measured versus SCE. Reproduced by [67]

The obtained results confirm that the energy storage behavior of WO<sub>3</sub> is pseudocapacitive, by highlighting the morphology and crystal structure role in the activation of surface or redox mechanism as a function of applied potential. In the next paragraph, the better WO<sub>3</sub> electrode will be used as cathode for the realization of an asymmetric supercapacitor device as proof of concept, subsequently comparing the obtained data with those reported in literature.

### 5.5 Prototype and comparison with literature

To evaluate the energy storage activity of WO<sub>3</sub> based electrodes in realistic conditions, an asymmetric supercapacitor (ASC) has been realized, in which the above characterized electrode and a GP electrode act as cathode and anode, respectively, in the two-electrode setup shown in Figure 5. 11 with 1 M H<sub>2</sub>SO<sub>4</sub> electrolyte solution. By using an

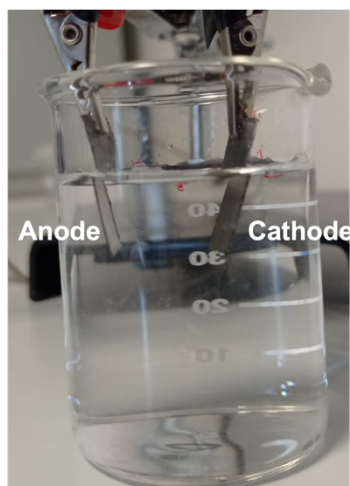


Figure 5. 11: Photograph of the ASC devices with cathode and anode (red and yellow cable respectively).

asymmetric configuration, a wide potential range can be explored, to reach the maximum value of energy and power density [169]. To evaluate the C<sub>s</sub>, CV and GCD were performed in the operating voltage range from -1 V to 0.8 V. Figure 5.12 a shows CV curves obtained at different scan rates (from 5 to 100 mV/s). The proportional expansion of CV curves as the scan rate increases reveals a fast charging/discharging capability [45]. At negative potentials the CV curves are quite similar to those of the single WO<sub>3</sub> based electrode (see Figure 5.5 b for more details). Figure A5.3 a shows the C<sub>s</sub> obtained from CV curves as a function of the scan rate: the C<sub>s</sub> decreases as the scan rate increases from 232 F/g at 10 mV/s to 115 F/g at 100 mV/s. The relatively high values of C<sub>s</sub> confirm the promising charge storage characteristics of WO<sub>3</sub>. This can be probably ascribed to the high wettability of the WO<sub>3</sub> urchin-like

nanostructures (see details in high magnification SEM image in Figure 5.4 c), which is useful for increasing the electrochemical active surface.

Figure 5.12 b shows the GCD curves obtained at different current density (from 0.1 A/g to 3 A/g, the lowest current densities curves are reported in the inset) in the potential ranges from -1 V to 0.8 V. The charge and discharge curves are asymmetric, again confirming the existence of a pseudocapacitive behavior of the WO<sub>3</sub> based electrode [167]. The  $C_s$  as a function of the current density is reported in Figure A5.3 b. As the current density increases, the  $C_s$  decreases from 300 F/g at 0.1 A/g to 50 F/g at 10 A/g, as expected.

Ragone plot is commonly used to compare different energy storage devices, by using the energy and power density ( $E_d$  (W\*h\*Kg<sup>-1</sup>) and  $P_d$  (W\*Kg<sup>-1</sup>) respectively), defined from GCD analysis as follow [45]:

$$E_d = \frac{1}{2} C_s \Delta V^2 \quad (5.5)$$

$$P_d = E_d \Delta t \quad (5.6)$$

where  $C_s$  is the specific capacitance obtained from GCD curves,  $\Delta V$  is the potential interval and  $\Delta t$  is the discharge time. The as tested ASC device shows the higher  $E_d$  of 134 W\*h\*Kg<sup>-1</sup> at  $P_d$  of 135 W\*Kg<sup>-1</sup> and the higher  $P_d$  of 13500 W\*Kg<sup>-1</sup> at  $E_d$  of 26 W\*h\*Kg<sup>-1</sup>. Figure 5.13 shows the Ragone plot ( $P_d$  reported as a function of  $E_d$ ). Values related to our WO<sub>3</sub> based ASC are reported as red stars, for each analyzed current density, while the spheres are data reported from literature (see color legend for references). In a Ragone plot, batteries lie in the bottom right corner, while capacitors stay in the upper left corner, as Figure 5.2 shows; pseudocapacitors bridge the gap. Our data span a very wide range of performances with many experimental points, which is a key feature for maximization of  $E_d$  and  $P_d$ . The  $E_d$  and  $P_d$  obtained in the present case are higher than those of several previously reported ASC based on WO<sub>3</sub>-WO<sub>3</sub>·0.5H<sub>2</sub>O mixtures (23.4 W\*h\*Kg<sup>-1</sup> at 5200 W\*Kg, orange ball) [163], RuO<sub>2</sub>/h-WO<sub>3</sub> nanorods (20 W\*h\*Kg<sup>-1</sup> at 400 W\*Kg and 15 W\*h\*Kg<sup>-1</sup> at 4000 W\*Kg green balls) [164], graphene-WO<sub>3</sub> nanowire nanocomposite (95 W\*h\*Kg<sup>-1</sup> at 1000 W\*Kg and 25 W\*h\*Kg<sup>-1</sup> at 6000 W\*Kg, violet balls)



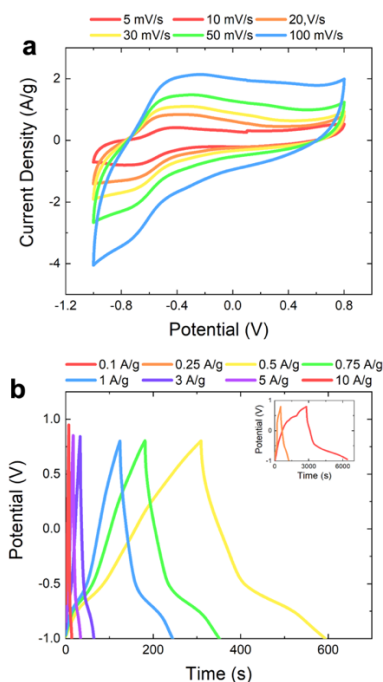


Figure 5.12: (a) CV curves at different scan rate of the ASC realized by using GP as anode and NF WO<sub>3</sub>\_ann70 paste electrode; (b) GCD of ASC in the potential range between -1 to 0.8 V. The inset shows a magnification of GCD curves at higher current density. Potential are measured versus SCE. Reproduced by [67].

[165], carbon-WO<sub>3</sub> nanocomposite (35 W\*h\*Kg<sup>-1</sup> at 200 W\*Kg and 18 W\*h\*Kg<sup>-1</sup> at 10000 W\*Kg, yellow balls) [167]. These promising results can be ascribed to the good agreement between the highly pure hexagonal crystal structure and the urchin-like morphology, which allows to increase the electrolyte exposed surface, as well as the wettability of WO<sub>3</sub> based electrode.

## 5.6 Conclusion

In conclusion, WO<sub>3</sub> nanostructures, synthesized by simple and low-cost hydrothermal technique, followed by air calcination, were investigated as potential candidates for electrodes in pseudocapacitors. The WO<sub>3</sub> nanostructures crystal structure strongly depends on the post growth annealing

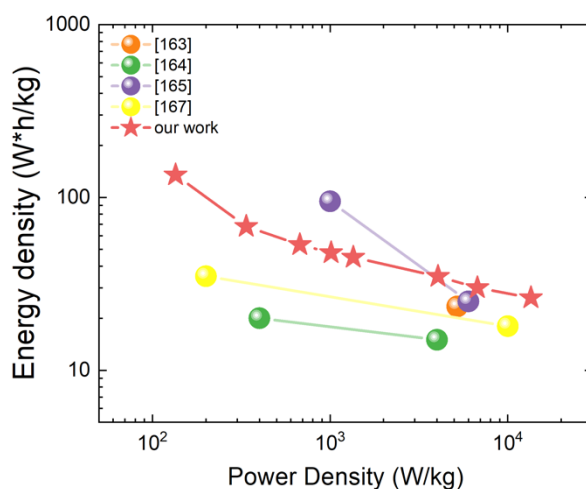


Figure 5.13: Ragone plot obtained from the as tested WO<sub>3</sub> based ASC (red stars) compared to those reported in literature for WO<sub>3</sub> based ASC. Reproduced by [67].

temperatures, reaching a pure hexagonal structure after air annealing at 70°C. As synthesized WO<sub>3</sub> nanostructures present two typologies (3 μm large urchin-like and much smaller nanorods) which have been selected by filtering procedure. The electrochemical energy storage mechanisms are described in terms of surface and diffusion limited processes, highlighting the role of morphology and crystal structure. Exceptional energy storage activity is obtained for the pure hexagonal WO<sub>3</sub> nanostructures if both urchin-like nanostructures and nanorods are presents, with a C<sub>s</sub> of 632 F/g at 5 mV/s and of 466 F/g at 0.5 A/g. This is probably due to the higher exposed surface of the sample with both nanostructures, since urchin like nanostructures avoid the compaction of the nanorods. This electrode was used for the realization of an asymmetric supercapacitor, showing promising performances over a large range of energy and power ranges. The Ragone plot confirms the good ASC performances of the as synthesized WO<sub>3</sub>-based electrode compared to those reported in literatures, by paving the way to the development of low cost and highly performing WO<sub>3</sub> based-energy storage devices



## Conclusion and perspective

The aim of this thesis was the controlled synthesis of  $\text{WO}_3$  nanostructures, the engineering of the crystal phase and the study of performances in sensing, hydrogen production and energy storage applications. The hydrothermal synthesis of hexagonal  $\text{WO}_3$  nanorods and urchin-like nanostructures was in depth investigated and controlled to define the optimized procedure which leads to the reproducible synthesis of well-defined 1D hexagonal  $\text{WO}_3$  nanostructures with interesting physical and chemical properties, such as high stability in acidic environment and good performance in electrochemical applications.

The as synthesized  $\text{WO}_3$  nanorods were used for  $\text{H}_2$  sensing. The response and recovery curve were modeled by using the Langmuir adsorption model, thus individuating two different and independent mechanisms which are active simultaneously. The fast process (lifetimes of few seconds) is attributed to  $\text{H}_2$  interaction with adsorbed O at  $\text{WO}_3$  surface, in the response phase, and to O adsorption (barrier of 0.29 eV), in the recovery phase. Since a high concentration of  $\text{H}_2$  consumes all adsorbed oxygen leaving  $\text{WO}_3$  uncovered, the slow process (lifetimes of hundreds of seconds) is attributed to generation (barrier of 0.46 eV) and recombination (barrier of 0.82 eV) of oxygen vacancy in  $\text{WO}_3$  nanorods.

$\text{WO}_3$  nanorods were also used for the NO sensing. The experimental data show an unexpected trend which suggests that the interaction occurs through reducing processes, contrary to what was expected from an oxidizing gas-*n*-type semiconductor interaction. The Langmuir adsorption theory was used to model the experimental data, by individuating two interaction channels between NO and the adsorbed oxygen species on the  $\text{WO}_3$  surface, whose activation depends on the temperature. The fast and the slow channels are attributed to the interaction between NO and  $\text{O}_{ads}^{2-}$  and  $\text{O}_{ads}^-$ , respectively, with lifetimes of the order of few seconds in the first case and of  $\approx 450$  s in the latter case. The recovery phase is dominated by the O adsorption on the  $\text{WO}_3$  surface in the form of  $\text{O}_{ads}^-$  and  $\text{O}_{ads}^{2-}$  with lifetimes of few seconds in the first case and of 100-300 s in the second case.

Post growth thermal treatments were used to modify the crystal phase of  $\text{WO}_3$  nanostructures, thus obtaining an intriguing hexagonal-monoclinic phase junction which improves the catalytic activity of  $\text{WO}_3$  towards the electrochemical HER. The hexagonal and monoclinic contents strongly depend on the annealing time as well as the dimension of the as-formed monoclinic crystallites. In particular, the 60 min annealed  $\text{WO}_3$  powders show a monoclinic content of 56% and comparable monoclinic and hexagonal crystallite sizes. This sample exhibits exceptional catalytic activity for HER in 1 M  $\text{H}_2\text{SO}_4$  electrolyte with an overpotential of 170 mV at 10  $\text{mA}/\text{cm}^2$ , lower than those reported in literature for the Pt-free electrodes studied for HER (see Table 4.3 for more detail). The advantage of this h-/m- $\text{WO}_3$  combination can be ascribed to the formation of numerous phase junction interfaces at which the HER can occur faster thanks to the larger availability of electrons, as demonstrated by the Tafel, EIS, and Mott–Schottky analyses and ECSA and TOF determination.

The energy storage properties of  $\text{WO}_3$  were also studied as a function of morphology and crystal structure. The electrochemical energy storage mechanisms are described in terms of surface and diffusion limited processes, highlighting the role of morphology and crystal structure. Exceptional energy storage activity is obtained for the pure hexagonal  $\text{WO}_3$  nanostructures if both urchin-like nanostructures and nanorods are presents, with a  $C_s$  of 632 F/g at 5 mV/s and of 466 F/g at 0.5 A/g. This electrode was used for the realization of an asymmetric supercapacitor, showing promising performances over a large range of energy and power ranges, with energy and power density higher than those reported in literature.

Further experiments are ongoing to enhance the energy storage properties and HER catalytic activity of  $\text{WO}_3$  nanostructures. The doping and the decoration with noble metals will be studied, to modify and improve the chemical and physical properties, and to apply  $\text{WO}_3$  nanostructures in other fields, such as photoelectrochemical application and  $\text{H}_2$  gas storage.



# Appendix

## A1: Electrodeposition of WO<sub>3</sub> nanostructured film

As mentioned in Chapter 2, there are many techniques to synthesize nanostructured WO<sub>3</sub>: sputtering [170], thermal evaporation [171], sol-gel [172], electrodeposition [173] and hydrothermal [174]. Before the optimization of the hydrothermal synthesis, we studied the electrodeposition as synthesis technique for WO<sub>3</sub> films, since it represents a promising approach which combines low temperature, high control, and low-cost [175-179]. Typically, the used electrolyte is a peroxo-tungstic-acid (PTA) solution which produces WO<sub>3</sub> by an electroreduction process in acidic conditions. Unfortunately, long electrodeposition process leads to cracked WO<sub>3</sub> films; still, the early stage of synthesis is disregarded in literature despite of the great potentialities in producing nanostructures. Thus, understanding the growth kinetics at early stages is of paramount importance for WO<sub>3</sub> nanostructure synthesis by electrodeposition. In the next paragraphs, the electrodeposition process is investigated for a careful synthesis of WO<sub>3</sub> thin films. The electrodeposition potential and times are largely spanned, and morphological and compositional analyses were conducted to model the WO<sub>3</sub> growth kinetics at early stages.

### A1.1 Synthesis and morphological characterization

Samples were synthesized by using electrodeposition technique with a peroxo-tungstic-acid (PTA) solution (6.5 g of W metallic powder in a mixture of 40 ml of H<sub>2</sub>O<sub>2</sub> (30%) and 4 ml of deionized water) [173]. As this reaction is exothermic, the PTA solution was constantly stirred for 24 h in a cold bath (between 0-10 °C). The obtained colorless solution was filtered with a 0.1 μm filter and refluxed for 6 h at 55°C to remove H<sub>2</sub>O<sub>2</sub> in excess. Then, dilution with an equal volume of anhydrous absolute ethanol was operated, to prevent precipitation of peroxo complexes [2], yielding a yellow-colored PTA

solution (Figure A1.1) with a pH of 1.24. Once cooled at room temperature, the solution was used as electrolyte during electrodeposition in the three-electrode electrochemical cell shown in Figure A1.1, with Ag/AgCl electrode as reference electrode, a platinum wire as counter electrode, and an Indium-Tin-Oxide (ITO) coated glass as working electrode. The ITO substrates were cut in 1 cm x 2 cm pieces and then washed with deionized water. Immersed area of each sample was measured after the process, to have comparable current density values. To prevent PTA degradation, the solution was stored at 4 °C between different synthesis and discarded one week after preparation. Films were deposited under potentiostatic condition by using a Versastat 4 potentiostat, by varying deposition time ( $t_d$ ) and applied potential ( $-V_d$ ) for different samples. Just after electrodeposition the samples, promptly rinsed with deionized water, were dark blue, but fully bleached in 1 day at room atmosphere.

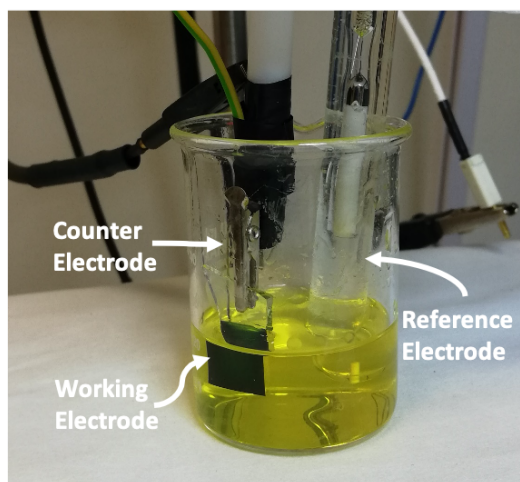


Figure A1.1: experimental setup for the electrodeposition of  $\text{WO}_3$  films. It's possible to distinguish the working electrode, the counter electrode, and the reference electrode. They are immersed into the peroxy-tungstic acid (PTA) solution [42].

The morphological analyses were carried out by a scanning electron microscope (SEM) Gemini Field Emission SEM Carl Zeiss SUPRATM 25 (FEG-SEM). Figure A1.2 shows high (a-c) and low (d-f) magnification SEM images of electrodeposited films, obtained by using different



## Appendix A1: Electrodeposition of WO<sub>3</sub> nanostructured film

electrodeposition parameters:  $V_d=0.35$  V and  $t_d=10$  min (a),  $V_d=0.45$  V and  $t_d=3$  min (b),  $V_d=0.55$  V and  $t_d=20$  s (c),  $V_d=0.65$  V and  $t_d=3$  min (d),  $V_d=0.45$  V and  $t_d=10$  min (e),  $V_d=0.55$  V and  $t_d=3$  min (f). Figure A1.2 a-c show continuous electrodeposited films (even at much lower magnification), while Figure A1.2 d-f show SEM images of samples with broken WO<sub>3</sub> film, composed of  $\mu\text{m}$  sized islands, already visible at low magnification. The film breaking is probably caused by high mechanical stress, due to lattice mismatch, for thick WO<sub>3</sub> film [180, 181]. Thus, increasing  $V_d$  and/or  $t_d$  leads to cracked films: at  $V_d=0.45$  V passing from (b) 3 to (e) 10 min causes film breaking, as well as at  $V_d=0.55$  V from (c) 20 s to (e) 3 min.

By observing the high magnification SEM images (Figure A1.2 a-c) a specific pattern can be seen, revealing that WO<sub>3</sub> film is made of nanograins with an average lateral size of 50 nm, regardless of  $V_d$  and  $t_d$ .

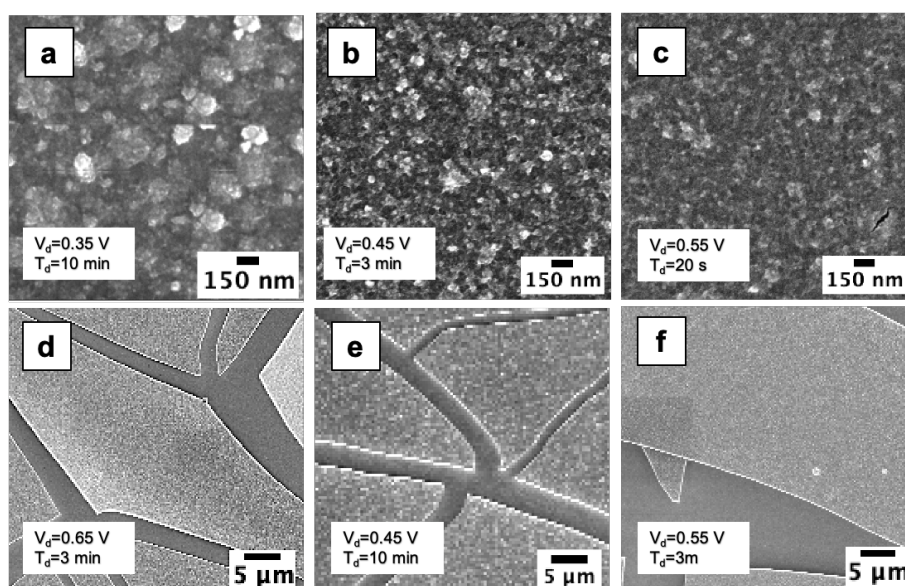


Figure A1.2 SEM images of electrodeposited WO<sub>3</sub> by using: a)  $V_d=0.35$  V and  $t_d=10$  min; b)  $V_d=0.45$  V and  $t_d=3$  min; c)  $V_d=0.55$  V and  $t_d=20$  s; d)  $V_d=0.65$  V and  $t_d=3$  min; e)  $V_d=0.45$  V and  $t_d=10$  min; f)  $V_d=0.55$  V and  $t_d=3$  min. It's possible to observe that that depending on  $V_d$  and  $t_d$ , the obtained films are uncracked [42].

Atomic Force Microscopy (AFM) studies were carried out by a Bruker-Innova microscope operating in contact mode and employing ultra-sharpened Si tips

(MSNL-10 from Bruker, with anisotropic geometry, radius of curvature  $\sim 2$  nm, tip height  $\sim 2.5$   $\mu\text{m}$ , front angle  $\sim 15^\circ$ , back angle  $\sim 25^\circ$ , side angle  $22.5^\circ$ ). The Si tips were substituted as soon as a resolution loose was observed during the AFM images acquisition. Each AFM images was acquired using a scan rate of 0.3 Hz and acquiring 512x512 lines. The acquired AFM images were analyzed using the SPMLABANALYSES V7.00 software. Figure A1.3 shows the AFM image of the sample deposited at  $V_d=0.45$  V for 6 s and the relative AFM line spectrum. The obtained size distribution confirms that height of these nanograins is around 50 nm. Joining the information from high resolution SEM images (Figure A1.2 a-c) we can assume that WO<sub>3</sub> film is composed by nanograins, 50 nm in diameter. The WO<sub>3</sub> islands formed after the film cracking possess the same pattern (Figure A1.2 e), meaning that the morphology does not depend on the electrodeposition parameters, at least for the used ones.

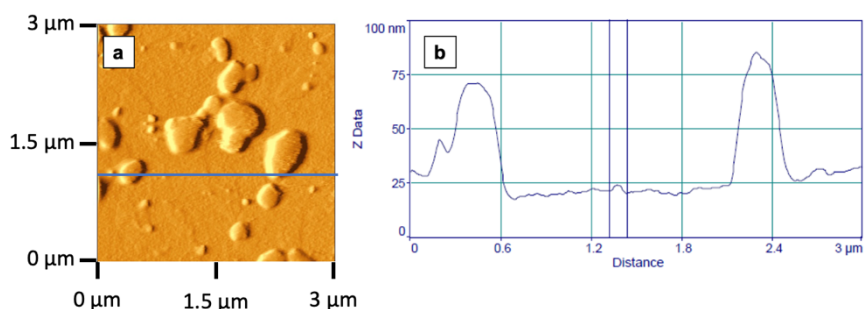


Figure A1.3: a) AFM image of the sample deposited by applying  $V_d=0.45$  V for 6 s. The blue line identifies the region in which the line spectrum showed in b) is obtained [42].

To investigate the early-stage growth kinetics an uncracked film deposition is needed, thus it was useful to correlate electrodeposition parameters ( $V_d$  and  $t_d$ ) with occurrence of film cracking. To do this, all samples were analyzed by SEM and placed in a deposition map (Figure A1.4) as a function of  $V_d$  and  $t_d$ . The uncracked (cracked) films are reported with green (red) balls. It's possible to individuate a border (grey colored region) between cracked and uncracked films, allowing to choose the parameters combination leading to desired WO<sub>3</sub> films. As expected, the higher the potential is, the shorter the time to get uncracked films. In literature, to investigate the electrodeposition of WO<sub>3</sub>

films a cathodic potential of 0.45 V for 10 min is often used [181-182]. From Figure A1.4 we observe that these parameters lead to cracked film, even if this combination lies very close to the border. In Figure A1.2 e we show that using  $V_d=0,45$  V and  $t_d=10$  min leads to quite large (tens of  $\mu\text{m}$ ) islands.

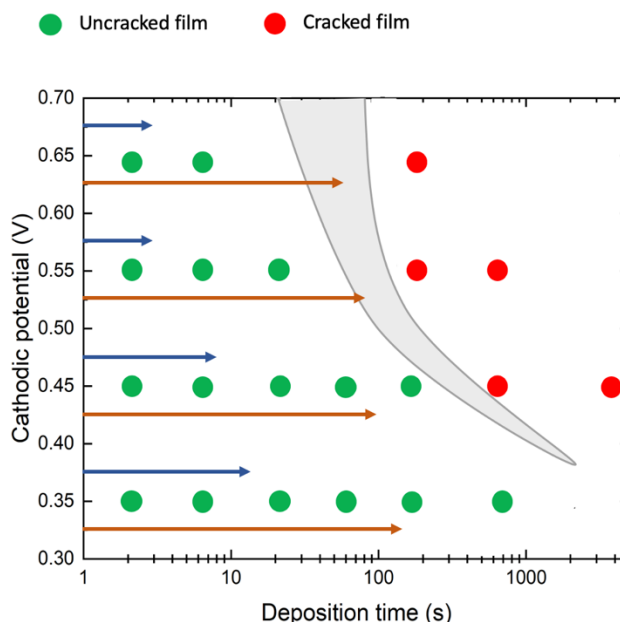


Figure A1.4: Deposition map: each electrodeposited sample is reported here as a function of  $V_d$  and  $t_d$ . The WO<sub>3</sub> films are reported as green or red dots if they result uncracked or cracked, respectively. Per each deposition at fixed  $V_d$ , two arrows indicate the time extent to get the maximum current ( $t_m$ , blue arrow) or the saturation current ( $t_s$ , orange arrow) [42].

Even if small differences in concentration of PTA solution and/or in lab procedures can affect the border line position in our deposition map, we preferred to stay well apart from that border to proceed with a quantitative investigation of growth kinetics of WO<sub>3</sub> film. Thus, in the following only uncracked samples will be considered.

Transmittance spectra were obtained by using an UV-VIS-NIR spectrophotometer Varian Cary 500. Figure A1.5 shows the Tauc plot obtained from transmittance spectrum of a sample deposited with  $V_d=0.45$  V for 3 min. Such a combination allows to have a WO<sub>3</sub> film thick enough to create a homogeneous film, but uncracked (Figure A1.2b). The linear fit (red line) of Tauc plot gives information about the band gap [69], which results

3.37±0.01 eV. This value suggests that the film is amorphous, according to the data reported in literature [2].

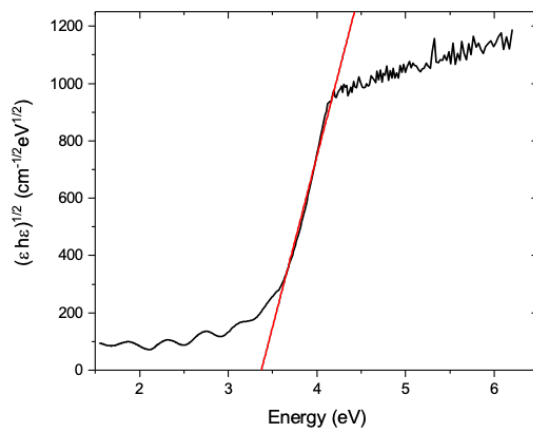


Figure A1.5: Tauc plot of sample deposited at  $V_d=0.45V$  for 3 min. The red line is the linear fit [42].

The WO<sub>3</sub> films were also analyzed by X-ray diffraction using a Bruker Discover™ diffractometer equipped with thin film attachments and a K<sub>α</sub> Cu source.<sup>1</sup> The XRD pattern of this film is reported in Figure A1.6, showing only peaks related to the ITO substrate and confirming the amorphous phase of the electrodeposited WO<sub>3</sub> film.

In the next paragraph, the nucleation and growth processes will be modeled and described.

---

<sup>1</sup> These analyses were carried out in collaboration with Dr. Alessandra Alberti of CNR-IMM Catania, Italy

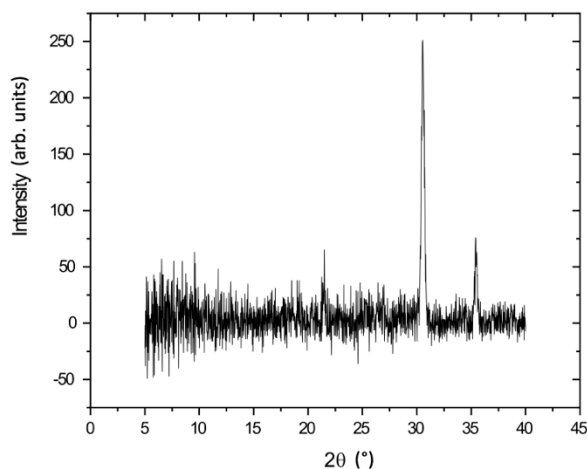


Figure A1.6: XRD pattern of the sample deposited by applying  $V_d=0.45$  V for 3 min. The peaks are related to the ITO presence in the substrate [42].

## A1.2 Nucleation and growth model

During electrodeposition, the cathodic (negative) current is acquired as a function of time, giving insights into the kinetics of the process. As an example, in Figure A1.7 a (lin-log scale) we report the transient of cathodic current density for five samples obtained at  $V_d=0.45$  V, by varying  $t_d$  from 2 s to 180 s. The same current transient is showed by all samples, as expected, with an increase up to a maximum ( $I_m$ ) at 7 s ( $t_m$ ) and a decrease leading to a plateau after around 100 s ( $t_s$ ). During the first 100 s the current shows a variation of more than 20% in its value and such a feature talks about early stage kinetics of electrodeposition process. It should be noted that similar trends also occur for other cathodic potentials (Figure A1.7 b) with a time extent of transient lower at higher cathodic potential.

To account for the current transient, we considered the Sharifker-Hills model (S-H model) [183], that describes film growth process during electrodeposition in terms of nucleation and diffusion processes. According to the S-H model, nucleation can be instantaneous or progressive. In the instantaneous case, all nucleation centers are speedily formed as electrodeposition starts and nuclei density remains constant from there on.

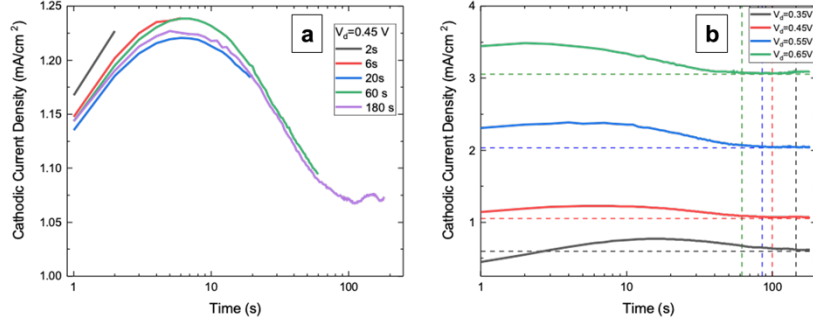


Figure A1.7: (a) Current transients recorded during the samples electrodeposition at  $V_d = 0.45$  V; (b) Current transients recorded during the samples electrodeposition by applying different  $V_d$  for 3 min. The dotted lines allow to individuate the different  $t_s$  for the different  $V_d$  values. Reproduced by [42].

A diffusive region starts to grow up around each nucleus leading to current increase; as soon as diffusion regions overlap each other, at  $t=t_m$ , a current decrease occurs, because of transition from convergent to linear diffusion. In the progressive nucleation, nuclei are continuously formed during growth, so that nuclei density increases linearly with time. Also in this case, transition from convergent to linear regime is obtained at  $t=t_m$ .

In Figure A1.8, kinetics transients for instantaneous and progressive nucleations, as described by the S-H model, are reported as normalized current, according to the following relation:

$$\frac{i^2}{i_m^2} = \frac{1.9542}{t/t_m} \{1 - \exp[-1.2564(t/t_m)]\}^2 \quad (\text{A1.1})$$

for instantaneous nucleation and

$$\frac{i^2}{i_m^2} = \frac{1.2254}{t/t_m} \{1 - \exp[-2.3367(t/t_m)^2]\}^2 \quad (\text{A1.2})$$

for progressive nucleation [183].

It is evident that for progressive nucleation a steeper current increase is observed in comparison to the instantaneous case, allowing to discriminate nucleation type. In the same figure we reported the experimental current

transient of our sample, as an example, deposited with a cathodic potential of 0.35 V for 3 min. Our experimental transient curves show trend compatible with instantaneous nucleation process. For  $t > t_m$ , the experimental curve results slightly higher than theoretical one, probably because of a more efficient diffusion process. Similar comparison was done for all experimental current transients, confirming that WO<sub>3</sub> electrodeposition is characterized by an instantaneous nucleation process, probably ascribed to the ITO substrate whose surface could drive a fast formation of WO<sub>3</sub> nuclei. The instantaneous nucleation could also be confirmed by the evidence that WO<sub>3</sub> film is composed of 50 nm sized grains (Figure A1.2 a-c), regardless of the cathodic potential or growth time.

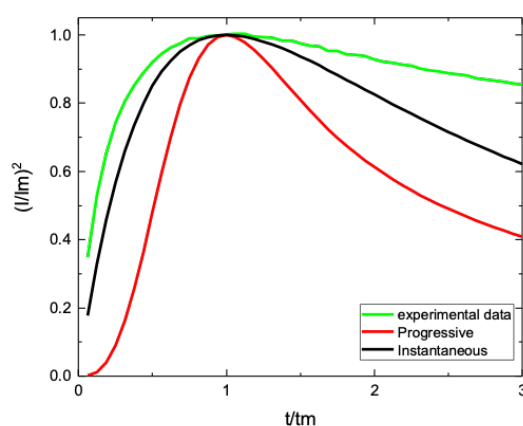


Figure A1.8: Comparison between the experimental data (green curve) and the theoretical data of the Sharifker-Hills model for instantaneous and progressive nucleation (black and red curve, respectively). The experimental curve is related to electrodeposition of WO<sub>3</sub> by using  $V_d = 0.35$  V and  $t_d = 3$  m [42].

In order to study the electrodeposition kinetics, it is useful to observe high resolution SEM images (Figure A1.9) referring to early stage growth. At cathodic potential of 0.45 V,  $t_m$  and  $t_s$  are 7s and 100s, respectively, thus we found, as expected, a full coverage of substrate only after 100 s (Figure A1.9

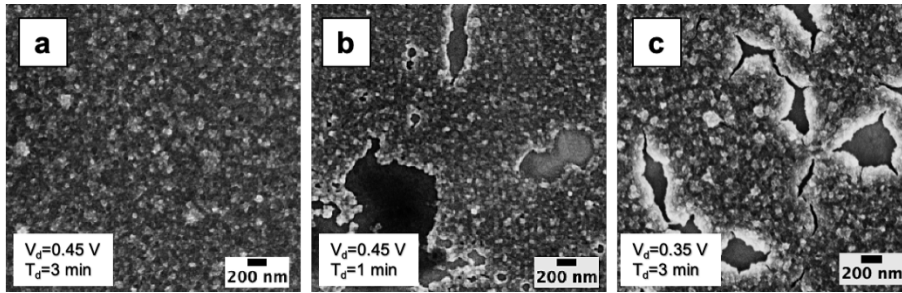


Figure A1.9: High resolution SEM images of the samples deposited by applying a) 0.45 V for 3 min, b) 0.45 V for 1 min and c) 0.35 V for 3 min [42].

a), while at 60 s the electrodeposited WO<sub>3</sub> (Figure A1.9 b) presents many holes (200 nm sized) waiting to be filled by prolonging the growth. By reducing the cathodic potential to 0.35 V, a deposition of 3 min (Figure A1.9 c) gives a similar result to 60 s - 0.45 V sample, with many holes surrounded by the growing WO<sub>3</sub>. Thus, we can assume that electrodeposition transient proceeds with growth of isolated grains up to  $t_m$ , then merging of grains occurs roughly up to  $t_s$ , and an almost continuous film is got after  $t_s$ . Such considerations are useful to drive the deposition of a nanostructured versus continuous WO<sub>3</sub> film, as for times between  $t_m$  and  $t_s$  the uncomplete substrate coverage, leading to the observed holes, could increase the surface over volume ratio of W oxide. For the determination of W and O content Rutherford backscattering spectrometry (RBS, 2.0 MeV He<sup>+</sup> beam at normal incidence) with 165° backscattering angle was employed, by using a 3.5 MV HVEE Singletron accelerator. RBS spectra were analyzed using XRump software [184]. Figure A1.10 shows the RBS spectra of samples deposited at 0.45 V for 60 s. The arrows indicate the energy of He ions backscattered by W (1.836 MeV), Sn (1.752 MeV), Si (1.138 MeV) or O (731.8 keV) atoms on the surface of analyzed films. The signals for W and O are present as expected, while Sn (present in the ITO) and Si (glass below ITO) ones appear at lower energy since they are buried below WO<sub>3</sub> and ITO films, respectively. The inset reports only the W signal at increasing deposition times. The area below W peak quantifies the W dose on analyzed sample. The result of such exercise is reported in Figure A1.11 a), for different deposition parameters. The O content of WO<sub>3</sub> film is more challenging because of overlapping of RBS signal related



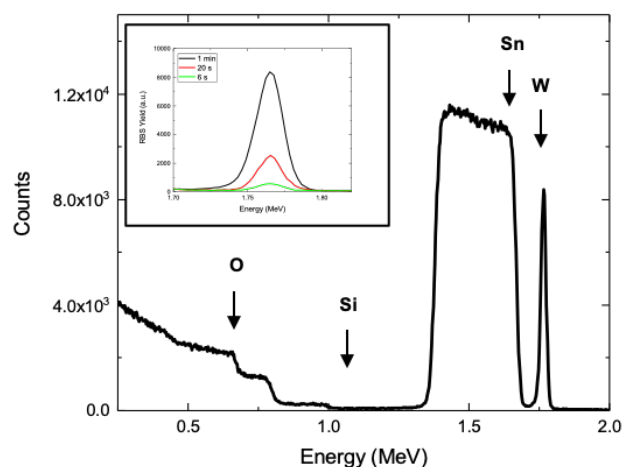


Figure A1.10: RBS spectra of electrodeposited WO<sub>3</sub>. The normal configuration is used for the determination of W dose from the integration of the peak related to the W presence for the sample deposited by using  $V_d=0.45$  V for 1 min; Inset: W peak of samples deposited by using  $V_d=0.45$  V for 6 s, 20 s and 1 min [42].

to underlying layers (ITO and glass). To overcome this, RBS spectra in glancing configuration were acquired, to enhance backscattering from surface. A W:O=1:3 stoichiometry was obtained by comparing the O and W dose in selected samples. Figure A1.11 a (log-log scale) reports the dose of W in electrodeposited films as a function of  $t_d$ . An increase with time of W dose is visible for 0.45 V. At lower and higher cathodic potential, a corresponding lower and higher W dose is found, as expected. As far as the W deposition rate is concerned, at 6 s an average value of  $1.7 \times 10^{15}$  at./cm<sup>2</sup> is obtained, while at 180 s the average rate increases to  $4 \times 10^{17}$  at./cm<sup>2</sup>s. Figure A1.11 b shows the time variation of electrical charge exchanged at working electrode per unit area of WO<sub>3</sub> film (obtained as time integral of current density). These last data follow the same trend observed in Figure A1.11 a and roughly agree with W dose, suggesting that at increasing current an increasing deposition rate occurs. To correlate these data with the growth kinetics, a model for the WO<sub>3</sub> electrodeposition is needed.

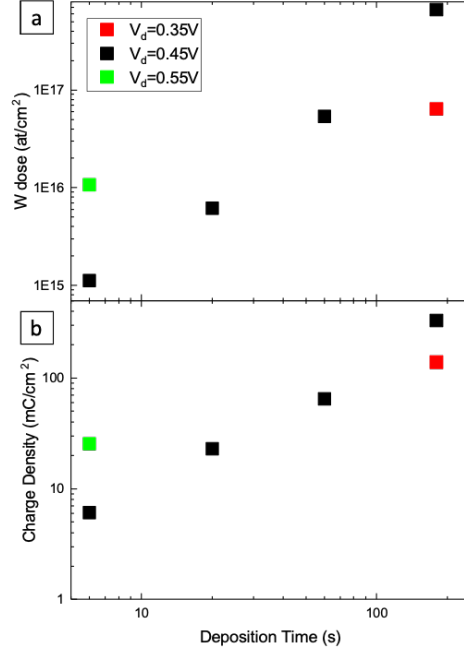
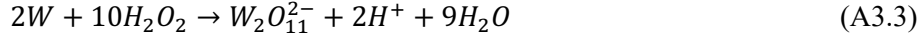
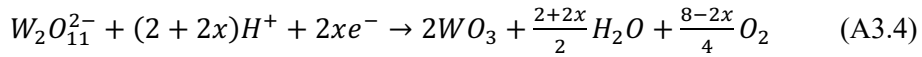


Figure A1.11: (a) W dose obtained from RBS spectra as a function of  $t_d$  for different  $V_d$  values; (b) charge density obtained from the integration of the current transient as a function of  $t_d$  for different  $V_d$  values [42].

According to Meulenkamp, electrodeposition of WO<sub>3</sub> from a PTA solution proceeds via a reduction process, starting with PTA dissociation [186]:



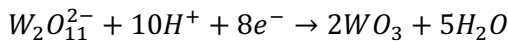
and followed by reduction of the peroxotungstate ion ( $W_2O_{11}^{2-}$ ) towards WO<sub>3</sub> formation [186]:



In the last reaction,  $x$  is the number of electrons exchanged for depositing a single WO<sub>3</sub> unit, thus relating the current at the working electrode to the deposition rate. According to the above chemical reaction,  $x = 0$  or 4 leads to high or null O<sub>2</sub> production. A high (low) value of  $x$  is related to a low (high)

effectiveness of current versus deposition rate, since a large (small) current exchanged at the working electrode is required to proceed with WO<sub>3</sub> deposition. Meulenkamp experimentally showed that  $x$  ranges between 1 and 3.5 [186]. Figure A1.12 reports the  $x$  value measured per each sample. In fact,  $x$  is the ratio between W dose (Figure A1.11 a) and charge exchanged at working electrode (Figure A1.11 b). For a cathodic potential of 0.45 V, a decreasing trend for  $x$  is clearly visible with time, starting from  $x=34$  at beginning, and reaching  $x=3.12$  only at 180 s, well after  $t_s$ . This reveals that for the whole transient the effectiveness of current versus deposition rate is very low. In fact, at early stage the W deposition rate is quite low in comparison to longer times, but it requires a current higher than at longer times. It is worth noting that  $x$  reaches a value which is in accordance with the reaction (A3.4) as soon as the transient ends up, i.e., at  $t_s$ . After the current transient the growth of WO<sub>3</sub> film proceeds with an effective use of exchanged charges at working electrode. In comparison to 0.45 V, higher or lower cathodic potentials leads to lower or higher  $x$  values for the same deposition time. This evidence confirms that the effectiveness of current is potential dependent as the current transient is.

After the transient, the WO<sub>3</sub> deposition seems to be compatible with the following reaction:



for which no O<sub>2</sub> production is needed. For longer times, the  $x$  value saturates and a constant chemical reaction like the above one can describe the WO<sub>3</sub> electrodeposition. At early stage some auxiliary process must be invoked to account for the larger current observed. Actually, during the transient an evident color change of samples is observed which can be caused by an H intercalation [1, 9], made even more effective by the holes present in the WO<sub>3</sub> layer (Figure A1.9). The H intercalation is a reduction process which can explain the quite larger current and the very high  $x$  value observed during the transient.

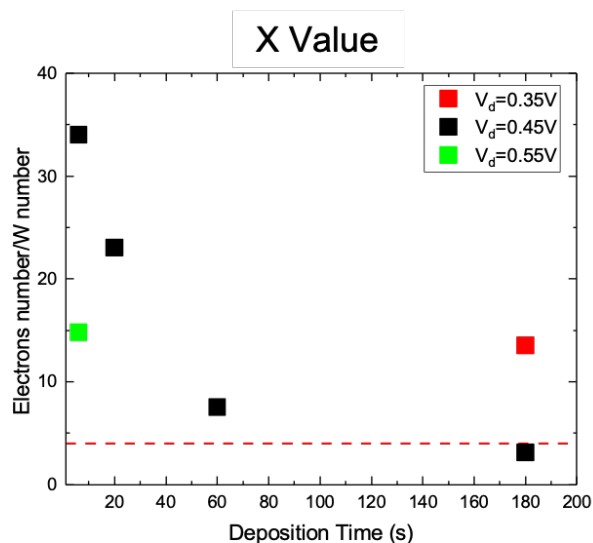


Figure A1.12: Exchanged electrons during the deposition of a single W atom for the samples deposited at different  $V_d$  for different  $t_d$ . The red line is the upper limit for this quantity which is 4 [42].

### A1.3 Conclusion

The electrodeposition of WO<sub>3</sub> film from a PTA solution was investigated at different cathodic potentials (0.35 – 0.65 V) and deposition times (2-1800 s). At long times and/or high cathodic potential a broken WO<sub>3</sub> film is obtained. Several combinations of electrodeposition parameters (deposition map) have been used to investigate the film synthesis and its morphology (continuous or broken films). The growth kinetics before breaking was deeply investigated, thus obtaining that the electrodeposition of a WO<sub>3</sub> film proceeds with an initial transient stage, with partial coverage of the substrate and a time-dependent current, followed by a steady state stage leading to continuous film and constant current. The WO<sub>3</sub> electrodeposition on ITO substrates shows an instantaneous nucleation and is diffusion-controlled, producing nanostructured films (50 nm sized grains) with 1:3 W:O stoichiometry. A quantitative analysis compared the current at the working electrode to the W deposition rate, validating a chemical reaction underlying the microscopic

mechanism for WO<sub>3</sub> deposition at longer times. At early stages of deposition, a larger current is observed despite a reduced W deposition rate, and a possible H intercalation process is discussed.

## A2. Addition of capping agent

For the hydrothermal synthesis of  $\text{WO}_3$  nanorods, NaCl is generally used as capping agent. It can be added before or after the acidification process with HCl, by leading to different results in terms of amount of produced  $\text{WO}_3$  nanostructures. Figure A1.1 shows SEM images of  $\text{WO}_3$  nanostructures on ITO substrates obtained by adding the NaCl (a) before and (b) after the acidification process. The latter case a large amount of well-defined nanostructures is produced, by suggesting a certain interaction between the NaCl and the HCl which disables the capping agent role in the first case.

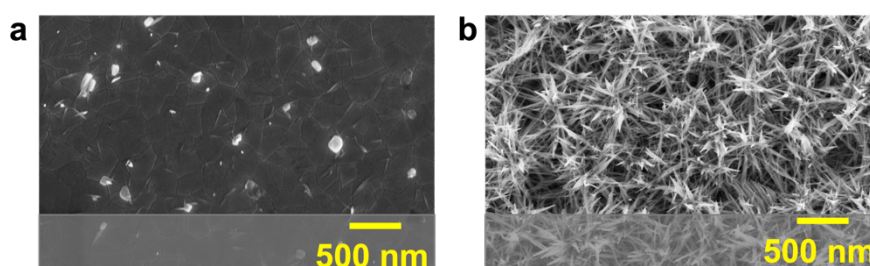


*Figure A2.1: SEM images of the  $\text{WO}_3$  nanostructures powder on ITO substrates obtained at 2.2 pH for 2 hours: the capping agent (NaCl) is added (a) before and (b) after the acidification*

### A3: WO<sub>3</sub> as catalyst for solid state H<sub>2</sub> gas storage

Beyond the electrochemical method, H<sub>2</sub> can be stored in gaseous form, by exploiting the physisorption and the chemisorption processes. Under appropriate pressure and temperature conditions, the Van der Waals interactions allow the adsorption of H<sub>2</sub> on the surface of the active materials, whereby the condition of large surface area is crucial for the development of efficient storage system. Because of the low intensity of the Van der Waals interactions, the physisorption occurs only at low temperatures, of the order of 77 K.

Carbon based materials represent a suitable candidate for this purpose, thanks to their high chemical and mechanical stability, molecular size pores, high surface area, and light weight [187, 188]. Among them, the biochar is a new generation material produced from agri-food waste, which aroused a great interest in scientific community for its properties. The biochar is produced after an oxygen-free pyrolysis and activation processes of biomass consisting of lignocellulose, obtained from rice, maize, sawdust, and similar waste. It is a porous and carbon-rich material, characterized by the presence of many functional groups on the surface, which make it suitable as catalyst support [189].

Metal oxide semiconductor nanostructures are versatile candidates as catalyst, thanks to the possibility to easily modulate their physical and chemical parameters. Among them, WO<sub>3</sub> represent a suitable choice for the hydrogenation process, thanks to its affinity for reducing gases, whereby the interaction between WO<sub>3</sub> and H<sub>2</sub> is widely studied in literature [1, 8, 64]. In the next paragraph, the mechanical production of biochar and hexagonal WO<sub>3</sub> nanorods mixture is described, as well as the initial tests of hydrogenation performance<sup>1</sup>.

---

<sup>1</sup> These analyses were carried out at University of Pavia in collaboration with Prof. Chiara Milanese.

## A3.1 Mixture preparation and characterization

Hexagonal WO<sub>3</sub> nanorods are prepared as described in Chapter 2. Thermogravimetric analysis (TGA) is carried out by using a TGA Q5000 of Thermal Analysis, to individuate mass variation as a function of temperature, for the determination of the thermal stability of the sample. Figure A3.1 shows the TGA of WO<sub>3</sub> nanorods. At 100 °C a mass loss of about 4 % is observed, which

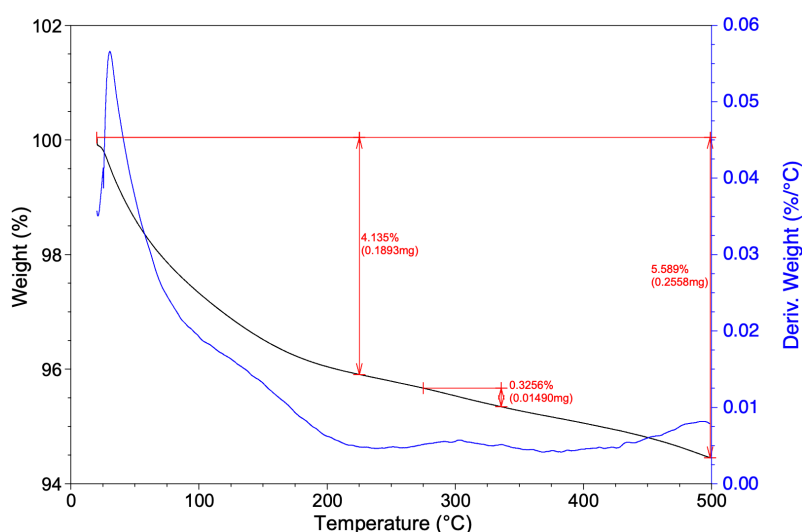


Figure A3.1: TGA of WO<sub>3</sub> nanorods, and its derivate (black and blue curve respectively), and the determination of mass loss (red).

can be ascribed to the loss of water encapsulated in the WO<sub>3</sub> powder. At 500 °C the mass loss does not exceed the 6 % thus indicating that the WO<sub>3</sub> are more stable in that temperature range.

WO<sub>3</sub> powder was further analyzed, by performing a differential scanning calorimetric (DSC) analysis, by using a DSC Q2000 V24 10 Build 122. This analysis allows to verify if any phase transition occurs in the tested temperature range, by measuring the amount of heat required for the temperature increase. Figure A3.2 shows the DSC spectrum of WO<sub>3</sub> nanorods obtained by increasing temperature from 0 to 350°C (first segment), by



lowering the temperature from 350 to 0 °C (second segment), and by increasing again the temperature from 0 to 350 °C (third segment).

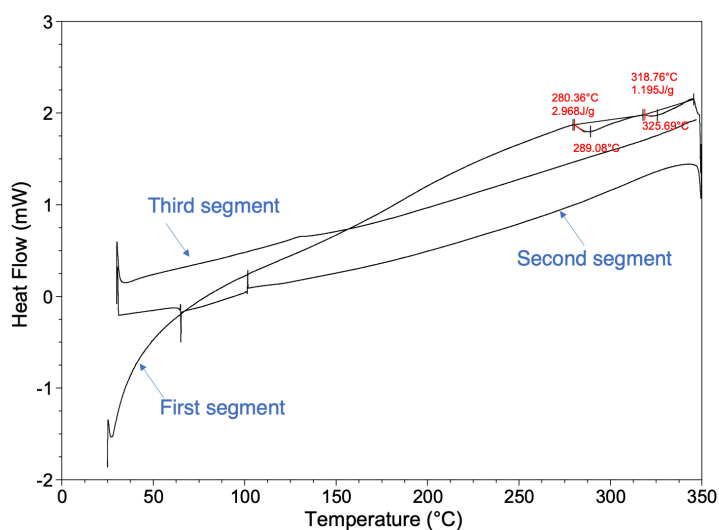


Figure A3.2: DSC spectrum of WO<sub>3</sub> nanorods.

Along the first segment, at around 280 °C and at 319 °C two wide peaks appears. At these temperatures the TGA confirms that no mass loss can be observed (Figure A3.1) by confirming that at these temperatures phase transitions occur from hexagonal to monoclinic and from monoclinic to orthorhombic, with enthalpy of 2.97 and 1.20 J/g respectively [2]. The first and the third segment are different each other, thus revealing that the phase transitions which occur from 280 and 320 °C are not reversible. These analyses confirm the stability of hexagonal WO<sub>3</sub> until 200-250 °C.

The used biochar was synthesized from rice husk as follows: rice husk was dried in air in an oven at 80 °C for one night and finely pulverized by using a ball milling. The obtained biochar powder was stored at room temperature, since rice husk is characterized by low humidity which makes it difficult for bacteria and mold to grow. A pyrolysis treatment was carried out at 650°C for 12 hours in an inert nitrogen atmosphere. After the natural cooling down, the biochar was activated with KOH. In detail, the biochar was mixed with KOH in a 1:6 concentration ratio, and the obtained compound is thermally treated at 350°C for 1 hour, and at 800 °C for 1 hour in a nitrogen atmosphere. To

remove the K exceeds, after the activation the biochar was washed with HCl 0.6 M as follows: a mixture of biochar and HCl (80 ml per gram of biochar) was stirred for 1 hour and the obtained solution is filtered by using a Büchner and a paper filter. After the washing of the obtained powder with water, the biochar was dried in air in a muffle at 80°C for 1 day.

The as prepared biochar was homogeneous blended with hexagonal WO<sub>3</sub> nanorods (4 %) with a turbula. In the next paragraph, the hydrogenation test of this mixture will be described.

### A3.2 PCT analysis

Hydrogenation tests were carried out by performing a pressure composition at constant temperature (PCT) analysis, by using a PCTPro-2000 of the Setaram-HyEnergy company shown in Figure A3.3. Measurements occurs in high vacuum and at 77 K, since the sample holder is cooled in a liquid nitrogen bath. The hydrogen stored in the analyzed sample was determined by performing a pressure analyses, considering the ideal gas law with the correction for the real case [190]:

$$\left[ \Delta P + a \left( \frac{\Delta n}{V} \right)^2 \right] (V - \Delta n b) = \Delta n R T$$

in which  $\Delta P$  is the pressure variation after the adsorption or desorption process,  $V$  is the volume of the sample holder (which is defined by a calibration process performed before the PCT measurement),  $\Delta n$  is the H<sub>2</sub> moles difference which results from the adsorption or desorption process,  $R$  is the ideal gas constant,  $T$  is the temperature, and  $a$  and  $b$  are the correction constant for the pressure and the volume of the gas respectively.

To study the physisorption of H<sub>2</sub> in the biochar-WO<sub>3</sub> (activated) mixture, the PCT analysis was performed by varying the pressure from 0 to 20 bar and by measuring the H<sub>2</sub> adsorbed content (%) after reaching the equilibrium condition. The analysis was performed also by considering the biochar without any catalyst (not activated). Figure A3.4 shows the amount of adsorbed H<sub>2</sub> (wt%) at different pressure conditions of the activated and of the

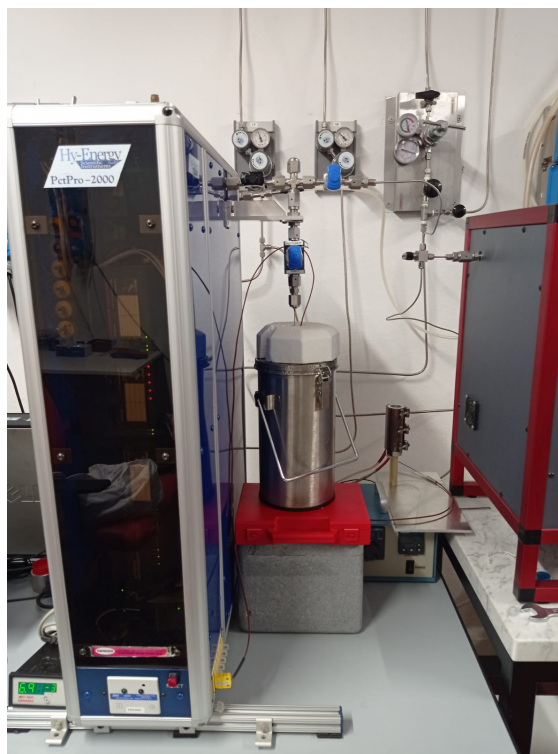


Figure A3.3: PCT instrument and nitrogen bath in which the sample holder is immersed.

not activated mixture (red and blue balls respectively). The amount of adsorbed H<sub>2</sub> is the same (~3.8 wt%), regardless of the presence of the WO<sub>3</sub> nanorods. The catalytic activity depends on the WO<sub>3</sub>-biochar junction formation, whereby the obtained results suggest that the mechanical mixing procedure which does not guarantee the WO<sub>3</sub> adhesion on the biochar.

### A3.3 Conclusion

The WO<sub>3</sub> nanorods were tested as catalyst for the H<sub>2</sub> gas storage. A mixture of WO<sub>3</sub> and biochar (obtained from rice husk) is prepared by using a turbula in a 4% concentration. TGA analysis of WO<sub>3</sub> nanorods shows that by increasing the temperature a weight loss of 4% is observed, associated to the

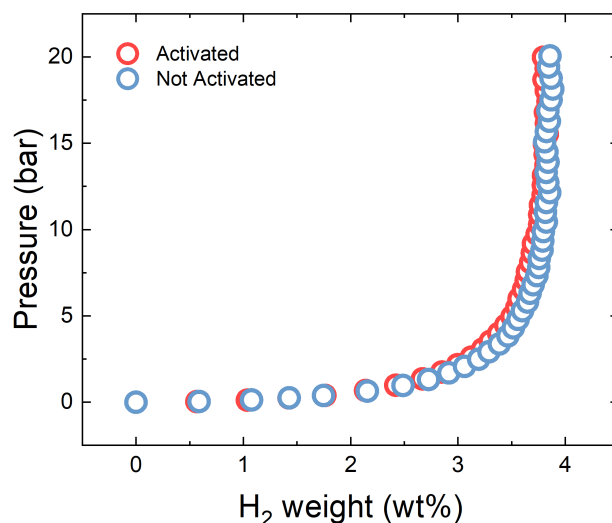


Figure A3.4: Results of PCT analyses on the activated (WO<sub>3</sub> and biochar) and not activated (biochar) samples (red and blue spheres respectively).

encapsulated water evaporation. DSC analyses of the WO<sub>3</sub> nanorods confirms that irreversible phase transitions occur at 280 °C and at 320 °C (from hexagonal to monoclinic and from monoclinic to orthorhombic respectively). The WO<sub>3</sub>-biochar mixture is tested by performing a PCT analyses, to evaluate the amount of adsorbed H<sub>2</sub> gas. The same value is obtained for the biochar and for the WO<sub>3</sub>-biochar mixture. This can be ascribed to the mechanic mixing process, which does not allow the WO<sub>3</sub>-biochar junction formation, crucial for the activation of the catalytic process. In the next future, different mixing procedure will be tested, such as the mixing in aqueous phase, following by the centrifugation and the drying of the obtained mixture. This process could make the adhesion of WO<sub>3</sub> on biochar surface more likely, as well as the formation of the WO<sub>3</sub>-biochar junction

## A4. Cyclic Voltammetry in the non-faradaic region

Figure A4.1 shows the CV of (a) WO<sub>3</sub>\_NA, (b) WO<sub>3</sub>\_A30, (c) WO<sub>3</sub>\_A60 and (d) WO<sub>3</sub>\_A90 electrodes in the non-faradaic region (-0.3 V –0.2 V) for the determination of the ECSA.

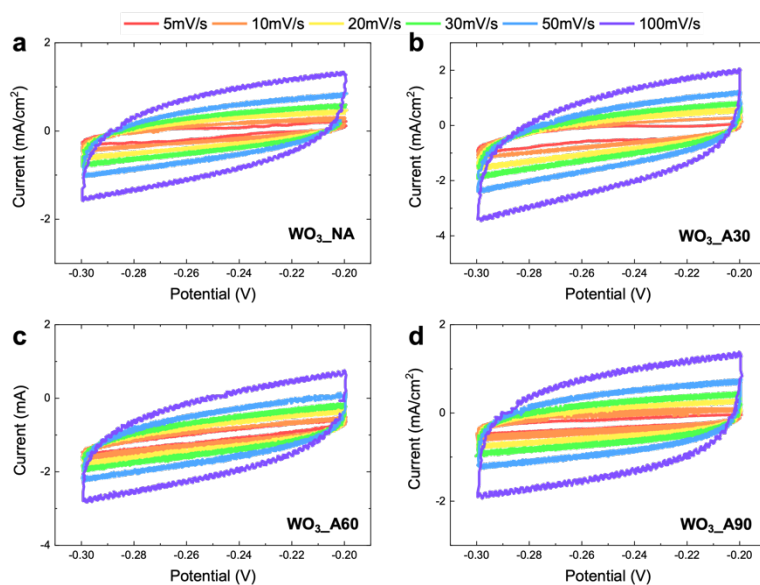


Figure A4.1: CV at different scan rate in the non-faradic region ranging between -0.3 V to -0.2 V vs SCE of (a) WO<sub>3</sub>\_NA, (b) WO<sub>3</sub>\_A30, (c) WO<sub>3</sub>\_A60 and (d) WO<sub>3</sub>\_A90 electrodes [133].

## A5. Supplementary electrochemical measurements

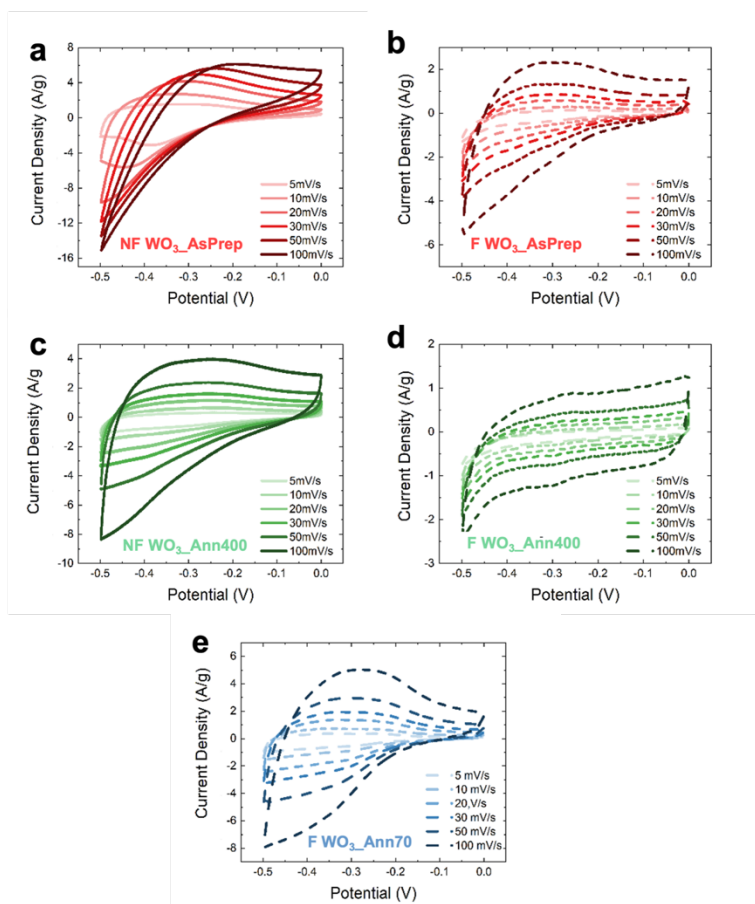


Figure A5.1: CV curves at different scan rates of NF and F (a and b) WO<sub>3</sub>\_AsPrep, (c and d) WO<sub>3</sub>\_Ann400 and (e) WO<sub>3</sub>\_Ann70 pastes, respectively [67].

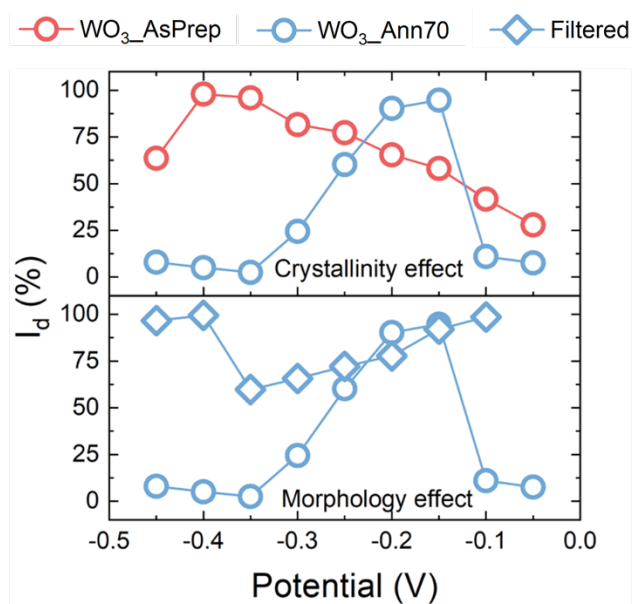


Figure A5.2: Comparison of diffusion-limited current contribution ( $I_d$ ) for (a) NF  $WO_3_{AsPrep}$  and  $WO_3_{Ann70}$  pastes-based electrodes and (b) NF and F  $WO_3_{Ann70}$  pastes-based electrodes as a function of the applied potential. The potential is measured versus SCE. Reproduced by [67].

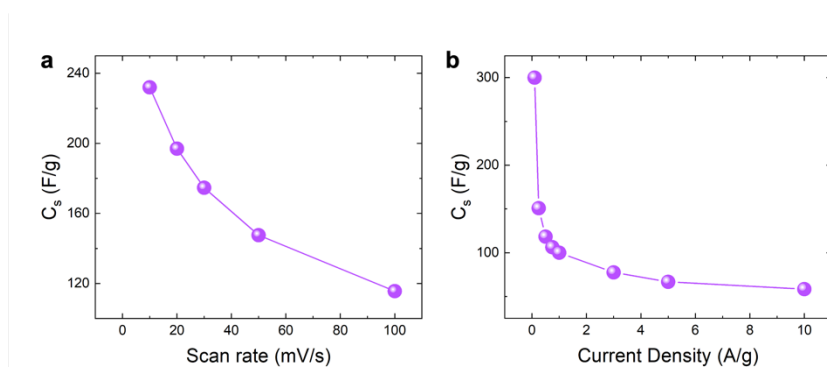


Figure A5.3:  $C_s$  as a function of (a) scan rate and (b) current density obtained from the GCD curves of the  $WO_3$  based ASC [67].

## References

- [1] Deb, S. K. Opportunities and Challenges in Science and Technology of WO<sub>3</sub> for Electrochromic and Related Applications. *Sol. Energy Mater. Sol. Cells* 2008, 92 (2), 245–258. <https://doi.org/10.1016/j.solmat.2007.01.026>.
- [2] Zheng, H.; Ou, J. Z.; Strano, M. S.; Kaner, R. B.; Mitchell, A.; Kalantar-Zadeh, K. Nanostructured Tungsten Oxide - Properties, Synthesis, and Applications. *Adv. Funct. Mater.* 2011, 21 (12), 2175–2196. <https://doi.org/10.1002/adfm.201002477>.
- [3] Ninh, T.; Schubert, W. D. Tungsten: Properties, Chemistry, Technology of the Element, Alloys, and Chemical Compounds; 2000; Vol. 37. <https://doi.org/10.5860/choice.37-2788>.
- [4] Cui, Y.; Liang, F.; Ji, C.; Xu, S.; Wang, H.; Lin, Z.; Liu, J. Discoloration Effect and One-Step Synthesis of Hydrogen Tungsten and Molybdenum Bronze (H x MO<sub>3</sub>) Using Liquid Metal at Room Temperature. *ACS Omega* 2019, 4 (4), 7428–7435. <https://doi.org/10.1021/acsomega.9b00840>.
- [5] Deb, S. K. Optical and Photoelectric Properties and Colour Centres in Thin Films of Tungsten Oxide. *Philos. Mag.* 1973, 27 (4), 801–822. <https://doi.org/10.1080/14786437308227562>.
- [6] Hersh, H. N.; Kramer, W. E.; McGee, J. H. Mechanism of Electrochromism in WO<sub>3</sub>. *Appl. Phys. Lett.* 1975, 27 (12), 646–648. <https://doi.org/10.1063/1.88346>.
- [7] Hashimoto, S.; Matsuoka, H. Mechanism of Electrochromism for Amorphous WO<sub>3</sub> Thin Films. *J. Appl. Phys.* 1991, 69 (2), 933–937. <https://doi.org/10.1063/1.347335>.



- [8] Georg, A.; Graf, W.; Neumann, R.; Wittwer, V. Mechanism of the Gasochromic Coloration of Porous WO<sub>3</sub> Films. *Solid State Ionics* 2000, 127 (3), 319–328. [https://doi.org/10.1016/S0167-2738\(99\)00273-8](https://doi.org/10.1016/S0167-2738(99)00273-8).
- [9] Granqvist, C. G. Electrochromic Tungsten Oxide Films: Review of Progress 1993-1998. *Sol. Energy Mater. Sol. Cells* 2000, 60 (3), 201–262. [https://doi.org/10.1016/S0927-0248\(99\)00088-4](https://doi.org/10.1016/S0927-0248(99)00088-4).
- [10] Murata, A.; Oka, N.; Nakamura, S.; Shigesato, Y. Visible-Light Active Photocatalytic WO<sub>3</sub> Films Loaded with Pt Nanoparticles Deposited by Sputtering. *J. Nanosci. Nanotechnol.* 2012, 12 (6), 5082–5086. <https://doi.org/10.1166/jnn.2012.4894>.
- [11] Tahir, M. B.; Nabi, G.; Rafique, M.; Khalid, N. R. Nanostructured-Based WO<sub>3</sub> Photocatalysts: Recent Development, Activity Enhancement, Perspectives and Applications for Wastewater Treatment. *Int. J. Environ. Sci. Technol.* 2017, 14 (11), 2519–2542. <https://doi.org/10.1007/s13762-017-1394-z>.
- [12] Miyauchi, M. Photocatalysis and Photoinduced Hydrophilicity of WO<sub>3</sub> Thin Films with Underlying Pt Nanoparticles. *Phys. Chem. Chem. Phys.* 2008, 10 (41), 6258–6265. <https://doi.org/10.1039/b807426g>.
- [13] Shaver, P. J. Activated Tungsten Oxide Gas Detectors. *Appl. Phys. Lett.* 1967, 11 (8), 255–257. <https://doi.org/10.1063/1.1755123>.
- [14] Akiyama, M.; Tamaki, J.; Miura, N.; Yamazoe, N. Tungsten Oxide-Based Semiconductor Sensor Highly Sensitive to NO and NO

## References

---

2. Chemistry Letters. 1991, pp 1611–1614.  
<https://doi.org/10.1246/cl.1991.1611>.
- [15] Barrett, E. P. S.; Georgiades, G. C.; Sermon, P. A. The Mechanism of Operation of WO<sub>3</sub>-Based H<sub>2</sub>S Sensors. Sensors Actuators B. Chem. 1990, 1 (1–6), 116–120.  
[https://doi.org/10.1016/0925-4005\(90\)80184-2](https://doi.org/10.1016/0925-4005(90)80184-2).
- [16] Jayaraj, M. K. Nanostructured Metal Oxides and Devices; 2020.
- [17] Wu, C. M.; Naseem, S.; Chou, M. H.; Wang, J. H.; Jian, Y. Q. Recent Advances in Tungsten-Oxide-Based Materials and Their Applications. Front. Mater. 2019, 6 (March), 1–17.  
<https://doi.org/10.3389/fmats.2019.00049>.
- [18] Shinde, P. A.; Jun, S. C. Review on Recent Progress in the Development of Tungsten Oxide Based Electrodes for Electrochemical Energy Storage. ChemSusChem 2020, 13 (1), 11–38. <https://doi.org/10.1002/cssc.201902071>.
- [19] Li, Y.; Zhai, X.; Liu, Y.; Wei, H.; Ma, J.; Chen, M.; Liu, X.; Zhang, W.; Wang, G.; Ren, F.; Wei, S. WO<sub>3</sub>-Based Materials as Electrocatalysts for Hydrogen Evolution Reaction. Front. Mater. 2020, 7 (May), 1–8. <https://doi.org/10.3389/fmats.2020.00105>.
- [20] Cong, S.; Geng, F.; Zhao, Z. Tungsten Oxide Materials for Optoelectronic Applications. Adv. Mater. 2016, 28 (47), 10518–10528. <https://doi.org/10.1002/adma.201601109>.
- [21] Wang, F.; Di Valentin, C.; Pacchioni, G. Electronic and Structural Properties of WO<sub>3</sub>: A Systematic Hybrid DFT Study. J. Phys. Chem. C 2011, 115 (16), 8345–8353.  
<https://doi.org/10.1021/jp201057m>.

- [22] Chatten, R.; Chadwick, A. V.; Rougier, A.; Lindan, P. J. D. The Oxygen Vacancy in Crystal Phases of WO<sub>3</sub>. *J. Phys. Chem. B* 2005, 109 (8), 3146–3156. <https://doi.org/10.1021/jp045655r>.
- [23] Lin, F.; Li, C. P.; Chen, G.; Tenent, R. C.; Wolden, C. A.; Gillaspie, D. T.; Dillon, A. C.; Richards, R. M.; Engtrakul, C. Low-Temperature Ozone Exposure Technique to Modulate the Stoichiometry of WO<sub>x</sub> Nanorods and Optimize the Electrochromic Performance. *Nanotechnology* 2012, 23 (25). <https://doi.org/10.1088/0957-4484/23/25/255601>.
- [24] Grätzel, M. PECreview. *Nature* 2001, 414 (November), 338–344.
- [25] Pereira-Ramos, J. P.; Baddour-Hadjean, R.; Kumagai, N.; Tanno, K. Improvement of the Electrochemical Behaviour of WO<sub>3</sub> as Reversible Cathodic Material for Lithium Batteries. *Electrochim. Acta* 1993, 38 (2–3), 431–436. [https://doi.org/10.1016/0013-4686\(93\)85161-Q](https://doi.org/10.1016/0013-4686(93)85161-Q).
- [26] Gabrielli, C.; Keddad, M.; Perrot, H.; Torresi, R. Lithium Insertion in WO<sub>3</sub> Studied by Simultaneous Measurements of Impedance, Electrogravimetric and Electro-Optical Transfer Functions. *J. Electroanal. Chem.* 1994, 378 (1–2), 85–92. [https://doi.org/10.1016/0022-0728\(94\)87059-4](https://doi.org/10.1016/0022-0728(94)87059-4).
- [27] Landauer, R. Information Is Inevitably Physical. *Feynman and Computation*. 2018, pp 77–92. <https://doi.org/10.1201/9780429500459>.
- [28] Poole Jr, C. P.; Owens, F. O.; *Introduction to nanotechnology*. John Wiley & Sons, 2003.

- [29] Kar, K. K.; Rana, S.; Pandey, J.; *Handbook of polymer nanocomposites processing, performance and application*. Berlin/Heidelberg, Germany: Springer, 2015.
- [30] Dong, C.; Zhao, R.; Yao, L.; Ran, Y.; Zhang, X.; Wang, Y. A Review on WO<sub>3</sub> Based Gas Sensors: Morphology Control and Enhanced Sensing Properties. *J. Alloys Compd.* 2020, 820, 153194. <https://doi.org/10.1016/j.jallcom.2019.153194>.
- [31] Sachs, M.; Park, J. S.; Pastor, E.; Kafizas, A.; Wilson, A. A.; Francàs, L.; Gul, S.; Ling, M.; Blackman, C.; Yano, J.; Walsh, A.; Durrant, J. R. Effect of Oxygen Deficiency on the Excited State Kinetics of WO<sub>3</sub> and Implications for Photocatalysis. *Chem. Sci.* 2019, 10 (22), 5667–5677. <https://doi.org/10.1039/c9sc00693a>.
- [32] Chen, R. S.; Wang, W. C.; Lu, M. L.; Chen, Y. F.; Lin, H. C.; Chen, K. H.; Chen, L. C. Anomalous Quantum Efficiency for Photoconduction and Its Power Dependence in Metal Oxide Semiconductor Nanowires. *Nanoscale* 2013, 5 (15), 6867–6873. <https://doi.org/10.1039/c3nr01635h>.
- [33] Cho, H. D.; Yoon, I. T.; Chung, K. B.; Kim, D. Y.; Kang, T. W.; Yuldashev, S. U. Low-Temperature Photoluminescence of WO<sub>3</sub> Nanoparticles. *J. Lumin.* 2018, 195 (October 2017), 344–347. <https://doi.org/10.1016/j.jlumin.2017.11.053>.
- [34] <https://rmis.jrc.ec.europa.eu/?page=crm-list-2020-e294f6>
- [35] Rizzo, A.; Goel, S.; Grilli, M. L.; Iglesias, R.; Jaworska, L.; Lapkovskis, V.; Novak, P.; Postolnyi, B. O.; Valerini, D. The Critical Raw Materials in Cutting Tools for Machining Applications: A Review. *Materials* (Basel). 2020, 13 (6). <https://doi.org/10.3390/ma13061377>.

- [36] Takano, K.; Inouye, A.; Yamamoto, S.; Sugimoto, M.; Yoshikawa, M.; Nagata, S. Gasochromic Properties of Nanostructured Tungsten Oxide Films Prepared by Sputtering Deposition. *Japanese J. Appl. Physics, Part 1 Regul. Pap. Short Notes Rev. Pap.* 2007, 46 (9 B), 6315–6318. <https://doi.org/10.1143/JJAP.46.6315>.
- [37] Baek, Y.; Yong, K. Controlled Growth and Characterization of Tungsten Oxide Nanowires Using Thermal Evaporation of WO<sub>3</sub> Powder. *J. Phys. Chem. C* 2007, 111 (3), 1213–1218. <https://doi.org/10.1021/jp0659857>.
- [38] Messier, R. Deposition Processes. *MRS Bull.* 1988, 13 (12), 29–32. <https://doi.org/10.1557/S0883769400063661>.
- [39] Shankar, N.; Yu, M. F.; Vanka, S. P.; Glumac, N. G. Synthesis of Tungsten Oxide (WO<sub>3</sub>) Nanorods Using Carbon Nanotubes as Templates by Hot Filament Chemical Vapor Deposition. *Mater. Lett.* 2006, 60 (6), 771–774. <https://doi.org/10.1016/j.matlet.2005.10.009>.
- [40] Yang, B.; Zhang, Y.; Drabarek, E.; Barnes, P. R. F.; Luca, V. Enhanced Photoelectrochemical Activity of Sol-Gel Tungsten Trioxide Films through Textural Control. *Chem. Mater.* 2007, 19 (23), 5664–5672. <https://doi.org/10.1021/cm071603d>.
- [41] Zheng, H.; Sadek, A. Z.; Latham, K.; Kalantar-Zadeh, K. Nanoporous WO<sub>3</sub> from Anodized RF Sputtered Tungsten Thin Films. *Electrochem. commun.* 2009, 11 (4), 768–771. <https://doi.org/10.1016/j.elecom.2009.01.033>.
- [42] Mineo, G.; Ruffino, F.; Mirabella, S.; Bruno, E. Investigation of WO<sub>3</sub> Electrodeposition Leading to Nanostructured Thin Films.

- Nanomaterials 2020, 10 (8), 1–12.  
<https://doi.org/10.3390/nano10081493>.
- [43] Mangalaraj, D.; Poongodi, S. Electrodeposition—a Simple and Effective Method for the Preparation of Metal Oxide Nanostructured Thin Films. *Springer Proc. Phys.* 2017, 189, 49–60.  
[https://doi.org/10.1007/978-3-319-44890-9\\_6](https://doi.org/10.1007/978-3-319-44890-9_6).
- [44] Gan, Y. X.; Jayatissa, A. H.; Yu, Z.; Chen, X.; Li, M. Hydrothermal Synthesis of Nanomaterials. *J. Nanomater.* 2020, 2020.  
<https://doi.org/10.1155/2020/8917013>.
- [45] Zheng, F.; Xi, C.; Xu, J.; Yu, Y.; Yang, W.; Hu, P.; Li, Y.; Zhen, Q.; Bashir, S.; Liu, J. L. Facile Preparation of WO<sub>3</sub> Nanofibers with Super Large Aspect Ratio for High Performance Supercapacitor. *J. Alloys Compd.* 2019, 772, 933–942.  
<https://doi.org/10.1016/j.jallcom.2018.09.085>.
- [46] Lee, Y.; Lee, T.; Jang, W.; Soon, A. Unraveling the Intercalation Chemistry of Hexagonal Tungsten Bronze and Its Optical Responses. *Chem. Mater.* 2016, 28 (13), 4528–4535.  
<https://doi.org/10.1021/acs.chemmater.5b03980>.
- [47] Ahmadian, H.; Tehrani, F. S.; Aliannezhadi, M. Hydrothermal Synthesis and Characterization of WO<sub>3</sub> Nanostructures: Effects of Capping Agent and PH. *Mater. Res. Express* 2019, 6 (10). <https://doi.org/10.1088/2053-1591/ab3826>.
- [48] Gu, Z.; Zhai, T.; Gao, B.; Sheng, X.; Wang, Y.; Fu, H.; Ma, Y.; Yao, J. Controllable Assembly of WO<sub>3</sub> Nanorods/Nanowires into Hierarchical Nanostructures. *J. Phys. Chem. B* 2006, 110 (47), 23829–23836. <https://doi.org/10.1021/jp065170y>.

- [49] Li, N.; Chang, T.; Gao, H.; Gao, X.; Ge, L. Morphology-Controlled WO<sub>3-x</sub> Homojunction: Hydrothermal Synthesis, Adsorption Properties, and Visible-Light-Driven Photocatalytic and Chromic Properties. *Nanotechnology* **2019**, *30* (41). <https://doi.org/10.1088/1361-6528/ab2a38>.
- [50] Liu, X.; Su, X.; Yang, C.; Ma, K. Hydrothermal Synthesis of WO<sub>3</sub> · 0.33H<sub>2</sub>O Nanorod Bundles as a Highly Sensitive Cyclohexene Sensor. *Sensors (Switzerland)* **2019**, *19* (5). <https://doi.org/10.3390/s19051257>.
- [51] Park, S. M.; Nah, Y. C.; Nam, C. Effects of Hydrothermal Treatment Duration on Morphology of WO<sub>3</sub> Nanostructures. *J. Nanosci. Nanotechnol.* **2017**, *17* (10), 7719–7722. <https://doi.org/10.1166/jnn.2017.14824>.
- [52] Wang, X.; Zhang, H.; Liu, L.; Li, W.; Cao, P. Controlled Morphologies and Growth Direction of WO<sub>3</sub> Nanostructures Hydrothermally Synthesized with Citric Acid. *Mater. Lett.* **2014**, *130*, 248–251. <https://doi.org/10.1016/j.matlet.2014.05.138>.
- [53] Wang, J.; Khoo, E.; Lee, P. S.; Ma, J. Synthesis, Assembly, and Electrochromic Properties of Uniform Crystalline WO<sub>3</sub> Nanorods. *J. Phys. Chem. C* **2008**, *112* (37), 14306–14312. <https://doi.org/10.1021/jp804035r>.
- [54] Wei, S.; Zhao, J.; Hu, B.; Wu, K.; Du, W.; Zhou, M. Hydrothermal Synthesis and Gas Sensing Properties of Hexagonal and Orthorhombic WO<sub>3</sub> Nanostructures. *Ceram. Int.* **2017**, *43* (2), 2579–2585. <https://doi.org/10.1016/j.ceramint.2016.11.064>.
- [55] Xie, Y. P.; Liu, G.; Yin, L.; Cheng, H. M. Crystal Facet-Dependent Photocatalytic Oxidation and Reduction Reactivity of

- Monoclinic WO<sub>3</sub> for Solar Energy Conversion. *J. Mater. Chem.* 2012, 22 (14), 6746–6751. <https://doi.org/10.1039/c2jm16178h>.
- [56] Yao, S.; Qu, F.; Wang, G.; Wu, X. Facile Hydrothermal Synthesis of WO<sub>3</sub> Nanorods for Photocatalysts and Supercapacitors. *J. Alloys Compd.* 2017, 724, 695–702. <https://doi.org/10.1016/j.jallcom.2017.07.123>.
- [57] Zheng, F.; Zhang, M.; Guo, M. Controllable Preparation of WO<sub>3</sub> Nanorod Arrays by Hydrothermal Method. *Thin Solid Films* 2013, 534, 45–53. <https://doi.org/10.1016/j.tsf.2013.01.102>.
- [58] Sōmiya, S.; Roy, R. Hydrothermal Synthesis of Fine Oxide Powders. *Bull. Mater. Sci.* 2000, 23 (6), 453–460. <https://doi.org/10.1007/BF02903883>.
- [59] Peng, T.; Ke, D.; Xiao, J.; Wang, L.; Hu, J.; Zan, L. Hexagonal Phase WO<sub>3</sub> Nanorods: Hydrothermal Preparation, Formation Mechanism and Its Photocatalytic O<sub>2</sub> Production under Visible-Light Irradiation. *J. Solid State Chem.* 2012, 194, 250–256. <https://doi.org/10.1016/j.jssc.2012.05.016>.
- [60] Kondalkar, V. V.; Kharade, R. R.; Mali, S. S.; Mane, R. M.; Patil, P. B.; Patil, P. S.; Choudhury, S.; Bhosale, P. N. Nanobrick-like WO<sub>3</sub> Thin Films: Hydrothermal Synthesis and Electrochromic Application. *Superlattices Microstruct.* 2014, 73, 290–295. <https://doi.org/10.1016/j.spmi.2014.05.039>.
- [61] Shinde, P. A.; Lokhande, A. C.; Chodankar, N. R.; Patil, A. M.; Kim, J. H.; Lokhande, C. D. Temperature Dependent Surface Morphological Modifications of Hexagonal WO<sub>3</sub> Thin Films for High Performance Supercapacitor Application. *Electrochim. Acta* 2017, 224, 397–404. <https://doi.org/10.1016/j.electacta.2016.12.066>.



- [62] Wu, X.; Yao, S. Flexible Electrode Materials Based on WO<sub>3</sub> Nanotube Bundles for High Performance Energy Storage Devices. *Nano Energy* 2017, 42 (October), 143–150. <https://doi.org/10.1016/j.nanoen.2017.10.058>.
- [63] Bhosale, N. Y.; Mali, S. S.; Hong, C. K.; Kadam, A. V. Hydrothermal Synthesis of WO<sub>3</sub> Nanoflowers on Etched ITO and Their Electrochromic Properties. *Electrochim. Acta* 2017, 246, 1112–1120. <https://doi.org/10.1016/j.electacta.2017.06.142>.
- [64] Mineo, G.; Moulace, K.; Neri, G.; Mirabella, S.; Bruno, E. H<sub>2</sub> Detection Mechanism in Chemoresistive Sensor Based on Low-Cost Synthesized WO<sub>3</sub> Nanorods. *Sensors Actuators B Chem.* 2021, 348, 130704. <https://doi.org/10.1016/j.snb.2021.130704>.
- [65] Wang, M. Plasma-Induced Nanoporous Metal Oxides with Nitrogen Doping for High-Performance Electrocatalysis. *Nanotechnology* 2017, 28 (24). <https://doi.org/10.1088/1361-6528/aa7178>.
- [66] Oura, K., Lifshits, V. G., Saranin, A. A., Zotov, A. V., & Katayama, M. (2013). *Surface science: an introduction*. Springer Science & Business Media.
- [67] Mineo, G.; Scuderi M.; Pezzotti Escobar G.; Mirabella, S.; Bruno, E. Engineering of nanostructured WO<sub>3</sub> powders for asymmetric supercapacitors, Submitted to *Nanomaterials*, 2022
- [68] Solonin, Y. M.; Khyzhun, O. Y.; Graivoronskaya, E. A. Nonstoichiometric Tungsten Oxide Based on Hexagonal WO<sub>3</sub>. *Cryst. Growth Des.* 2001, 1 (6), 473–477. <https://doi.org/10.1021/cg015545z>.

- [69] Raciti, R.; Bahariqushchi, R.; Summonte, C.; Aydinli, A.; Terrasi, A.; Mirabella, S. Optical Bandgap of Semiconductor Nanostructures: Methods for Experimental Data Analysis. *J. Appl. Phys.* 2017, 121 (23). <https://doi.org/10.1063/1.4986436>.
- [70] Glencross, D. A.; Ho, T. R.; Camiña, N.; Hawrylowicz, C. M.; Pfeffer, P. E. Air Pollution and Its Effects on the Immune System. *Free Radic. Biol. Med.* 2020, 151 (October 2019), 56–68. <https://doi.org/10.1016/j.freeradbiomed.2020.01.179>.
- [71] <https://www.clarity.io/blog/how-measuring-different-types-of-air-pollutants-creates-a-more-holistic-picture-of-air-pollution>
- [72] Shi, J.; Cheng, Z.; Gao, L.; Zhang, Y.; Xu, J.; Zhao, H. Facile Synthesis of Reduced Graphene Oxide/Hexagonal WO<sub>3</sub> Nanosheets Composites with Enhanced H<sub>2</sub>S Sensing Properties. *Sensors Actuators, B Chem.* **2016**, 230, 736–745. <https://doi.org/10.1016/j.snb.2016.02.134>.
- [73] Ji, H.; Zeng, W.; Xu, Y.; Li, Y. Nanosheet-Assembled Hierarchical WO<sub>3</sub> Flower-like Nanostructures: Hydrothermal Synthesis and NH<sub>3</sub>-Sensing Properties. *Mater. Lett.* **2019**, 250, 155–158. <https://doi.org/10.1016/j.matlet.2019.05.023>.
- [74] Hua, Z.; Tian, C.; Qiu, Z.; Li, Y.; Tian, X.; Wang, M.; Li, E. An Investigation on NO<sub>2</sub> Sensing Mechanism and Shielding Behavior of WO<sub>3</sub> Nanosheets. *Sensors Actuators, B Chem.* **2018**, 259 (2), 250–257. <https://doi.org/10.1016/j.snb.2017.12.016>.
- [75] Zhang, Y.; Zeng, W.; Li, Y. NO<sub>2</sub> and H<sub>2</sub> Sensing Properties for Urchin-like Hexagonal WO<sub>3</sub> Based on Experimental and First-

- Principle Investigations. *Ceram. Int.* **2019**, *45* (5), 6043–6050. <https://doi.org/10.1016/j.ceramint.2018.12.075>.
- [76] Arafat, M. M.; Dinan, B.; Akbar, S. A.; Haseeb, A. S. M. A. Gas Sensors Based on One Dimensional Nanostructured Metal-Oxides: A Review. *Sensors (Switzerland)* **2012**, *12* (6), 7207–7258. <https://doi.org/10.3390/s120607207>.
- [77] Zhang, J.; Liu, X.; Neri, G.; Pinna, N. Nanostructured Materials for Room-Temperature Gas Sensors. *Adv. Mater.* **2016**, *28* (5), 795–831. <https://doi.org/10.1002/adma.201503825>.
- [78] Nazemi, H.; Joseph, A.; Park, J.; Emadi, A. Advanced Micro- and Nano-Gas Sensor Technology: A Review. *Sensors (Switzerland)* **2019**, *19* (6). <https://doi.org/10.3390/s19061285>.
- [79] Kalanur, S. S. Structural, Optical, Band Edge and Enhanced Photoelectrochemical Water Splitting Properties of Tin-Doped WO<sub>3</sub>. *Catalysts* **2019**, *9* (5). <https://doi.org/10.3390/catal9050456>.
- [80] Yang, J.; Sudik, A.; Wolverton, C.; Siegel, D. J. High Capacity Hydrogen Storage Materials: Attributes for Automotive Applications and Techniques for Materials Discovery. *Chem. Soc. Rev.* **2010**, *39* (2), 656–675. <https://doi.org/10.1039/b802882f>.
- [81] Zhao, H.; Lu, D.; Wang, J.; Tu, W.; Wu, D.; Koh, S. W.; Gao, P.; Xu, Z. J.; Deng, S.; Zhou, Y.; You, B.; Li, H. Raw Biomass Electroreforming Coupled to Green Hydrogen Generation. *Nat. Commun.* **2021**, *12* (1), 1–10. <https://doi.org/10.1038/s41467-021-22250-9>.

- [82] Ohsawa, M. Ishikawa, K. Takahashi, M. Watanabe, K. Nishimaki, K. Yamagata, K.I. Katsura, Y. Katayama, S. Asoh, S. Ohta, Hydrogen acts as a therapeutic antioxidant by selectively reducing cytotoxic oxygen radicals, *Nat. Med.* **13** (2007) 688–694. <https://doi.org/10.1038/nm1577>.
- [83] Hübert, T.; Boon-Brett, L.; Black, G.; Banach, U. Hydrogen Sensors - A Review. *Sensors Actuators, B Chem.* **2011**, *157* (2), 329–352. <https://doi.org/10.1016/j.snb.2011.04.070>.
- [84] Luo, Y.; Zhang, C.; Zheng, B.; Geng, X.; Debliquy, M. Hydrogen Sensors Based on Noble Metal Doped Metal-Oxide Semiconductor: A Review. *Int. J. Hydrogen Energy* **2017**, *42* (31), 20386–20397. <https://doi.org/10.1016/j.ijhydene.2017.06.066>.
- [85] Wu, C. H.; Zhu, Z.; Huang, S. Y.; Wu, R. J. Preparation of Palladium-Doped Mesoporous WO<sub>3</sub> for Hydrogen Gas Sensors. *J. Alloys Compd.* **2019**, *776*, 965–973. <https://doi.org/10.1016/j.jallcom.2018.10.372>.
- [86] Chang, C. H.; Chou, T. C.; Chen, W. C.; Niu, J. S.; Lin, K. W.; Cheng, S. Y.; Tsai, J. H.; Liu, W. C. Study of a WO<sub>3</sub> Thin Film Based Hydrogen Gas Sensor Decorated with Platinum Nanoparticles. *Sensors Actuators, B Chem.* **2020**, *317* (May), 128145. <https://doi.org/10.1016/j.snb.2020.128145>.
- [87] Mattoni, G.; De Jong, B.; Manca, N.; Tomellini, M.; Caviglia, A. D. Single-Crystal Pt-Decorated WO<sub>3</sub> Ultrathin Films: A Platform for Sub-Ppm Hydrogen Sensing at Room Temperature. *ACS Appl. Nano Mater.* **2018**, *1* (7), 3446–3452. <https://doi.org/10.1021/acsanm.8b00627>.
- [88] Tian, F. H.; Gong, C.; Peng, Y.; Xue, X. H<sub>2</sub> Sensing Mechanism under Different Oxygen Concentration on the Hexagonal

- WO<sub>3</sub> (001) Surface: A Density Functional Theory Study. *Sensors Actuators, B Chem.* **2017**, *244*, 655–663. <https://doi.org/10.1016/j.snb.2016.12.035>.
- [89] Urso, M.; Leonardi, S. G.; Neri, G.; Petralia, S.; Conoci, S.; Priolo, F.; Mirabella, S. Room Temperature Detection and Modelling of Sub-Ppm NO<sub>2</sub> by Low-Cost Nanoporous NiO Film. *Sensors Actuators, B Chem.* **2020**, *305* (2), 127481. <https://doi.org/10.1016/j.snb.2019.127481>.
- [90] Mukherjee, K.; Majumder, S. B. Analyses of Response and Recovery Kinetics of Zinc Ferrite as Hydrogen Gas Sensor. *J. Appl. Phys.* **2009**, *106* (6). <https://doi.org/10.1063/1.3225996>.
- [91] Bange, K. Colouration of Tungsten Oxide Films: A Model for Optically Active Coatings. *Sol. Energy Mater. Sol. Cells* **1999**, *58* (1), 1–131. [https://doi.org/10.1016/S0927-0248\(98\)00196-2](https://doi.org/10.1016/S0927-0248(98)00196-2).
- [92] Mirzaei, A.; Kim, J. H.; Kim, H. W.; Kim, S. S. Gasochromic WO<sub>3</sub> Nanostructures for the Detection of Hydrogen Gas: An Overview. *Appl. Sci.* **2019**, *9* (9). <https://doi.org/10.3390/app9091775>.
- [93] Censabella, M.; Iacono, V.; Scandurra, A.; Moulaei, K.; Neri, G.; Ruffino, F.; Mirabella, S. Low Temperature Detection of Nitric Oxide by CuO Nanoparticles Synthesized by Pulsed Laser Ablation. *Sensors Actuators B Chem.* **2022**, *358* (January), 131489. <https://doi.org/10.1016/j.snb.2022.131489>.
- [94] Tao, P.; Xu, Y.; Zhou, Y.; Song, C.; Qiu, Y.; Dong, W.; Zhang, M.; Shao, M. Nitrogen Oxide (NO) Gas-Sensing Properties of Bi<sub>2</sub>MoO<sub>6</sub> Nanosheets Synthesized by a Hydrothermal Method. *Mater. Res.* **2017**, *20* (3), 786–790. <https://doi.org/10.1590/1980-5373-MR-2016-0824>.

- [95] Murali, G.; Reddeppa, M.; Seshendra Reddy, C.; Park, S.; Chandrakalavathi, T.; Kim, M. D.; In, I. Enhancing the Charge Carrier Separation and Transport via Nitrogen-Doped Graphene Quantum Dot-TiO<sub>2</sub> Nanoplate Hybrid Structure for an Efficient NO Gas Sensor. *ACS Appl. Mater. Interfaces* **2020**, *12* (11), 13428–13436. <https://doi.org/10.1021/acsami.9b19896>.
- [96] Ramu, S.; Chandrakalavathi, T.; Murali, G.; Kumar, K. S.; Sudharani, A.; Ramanadha, M.; Peta, K. R.; Jeyalakshmi, R.; Vijayalakshmi, R. P. UV Enhanced NO Gas Sensing Properties of the MoS<sub>2</sub> Monolayer Gas Sensor. *Mater. Res. Express* **2019**, *6* (8). <https://doi.org/10.1088/2053-1591/ab20b7>.
- [97] Cai, Z. X.; Li, H. Y.; Yang, X. N.; Guo, X. NO Sensing by Single Crystalline WO<sub>3</sub> Nanowires. *Sensors Actuators, B Chem.* **2015**, *219*, 346–353. <https://doi.org/10.1016/j.snb.2015.05.036>.
- [98] Moon, H. G.; Choi, Y. R.; Shim, Y. S.; Choi, K. Il; Lee, J. H.; Kim, J. S.; Yoon, S. J.; Park, H. H.; Kang, C. Y.; Jang, H. W. Extremely Sensitive and Selective NO Probe Based on Villi-like WO<sub>3</sub> Nanostructures for Application to Exhaled Breath Analyzers. *ACS Appl. Mater. Interfaces* **2013**, *5* (21), 10591–10596. <https://doi.org/10.1021/am402456s>.
- [99] Chen, D.; Yin, L.; Ge, L.; Fan, B.; Zhang, R.; Sun, J.; Shao, G. Low-Temperature and Highly Selective NO-Sensing Performance of WO<sub>3</sub> Nanoplates Decorated with Silver Nanoparticles. *Sensors Actuators, B Chem.* **2013**, *185*, 445–455. <https://doi.org/10.1016/j.snb.2013.05.006>.
- [100] Anantharaj, S.; Ede, S. R.; Karthick, K.; Sam Sankar, S.; Sangeetha, K.; Karthik, P. E.; Kundu, S. Precision and Correctness in the Evaluation of Electrocatalytic Water Splitting: Revisiting Activity

- Parameters with a Critical Assessment. *Energy Environ. Sci.* **2018**, *11* (4), 744–771. <https://doi.org/10.1039/c7ee03457a>.
- [101] Sekar, S.; Aqueel Ahmed, A. T.; Pawar, S. M.; Lee, Y.; Im, H.; Kim, D. Y.; Lee, S. Enhanced Water Splitting Performance of Biomass Activated Carbon-Anchored WO<sub>3</sub> Nanoflakes. *Appl. Surf. Sci.* **2020**, *508* (September 2019), 145127. <https://doi.org/10.1016/j.apsusc.2019.145127>.
- [102] Zou, X.; Zhang, Y. Noble Metal-Free Hydrogen Evolution Catalysts for Water Splitting. *Chem. Soc. Rev.* **2015**, *44* (15), 5148–5180. <https://doi.org/10.1039/c4cs00448e>.
- [103] <https://www.alfalaval.com/industries/energy-and-utilities/sustainablesolutions/sustainable-solutions/clean-energy/green-hydrogen/>
- [104] Zheng, T.; Sang, W.; He, Z.; Wei, Q.; Chen, B.; Li, H.; Cao, C.; Huang, R.; Yan, X.; Pan, B.; Zhou, S.; Zeng, J. Conductive Tungsten Oxide Nanosheets for Highly Efficient Hydrogen Evolution. *Nano Lett.* **2017**, *17* (12), 7968–7973. <https://doi.org/10.1021/acs.nanolett.7b04430>.
- [105] Hansen, J. N.; Prats, H.; Toudahl, K. K.; Mørch Secher, N.; Chan, K.; Kibsgaard, J.; Chorkendorff, I. Is There Anything Better than Pt for HER? *ACS Energy Lett.* **2021**, *6* (4), 1175–1180. <https://doi.org/10.1021/acsenergylett.1c00246>.
- [106] Battiato, S.; Bruno, L.; Terrasi, A.; Mirabella, S. Superior Performances of Electroless-Deposited Ni-P Films Decorated with an Ultralow Content of Pt for Water-Splitting Reactions. *ACS Appl. Energy Mater.* **2022**, *5* (2), 2391–2399. <https://doi.org/10.1021/acsaem.1c03880>.

- [107] Kibsgaard, J.; Chorkendorff, I. Considerations for the Scaling-up of Water Splitting Catalysts. *Nat. Energy* **2019**, *4* (6), 430–433. <https://doi.org/10.1038/s41560-019-0407-1>.
- [108] Gong, M.; Wang, D. Y.; Chen, C. C.; Hwang, B. J.; Dai, H. A Mini Review on Nickel-Based Electrocatalysts for Alkaline Hydrogen Evolution Reaction. *Nano Res.* **2016**, *9* (1), 28–46. <https://doi.org/10.1007/s12274-015-0965-x>.
- [109] Safizadeh, F.; Ghali, E.; Houlachi, G. Electrocatalysis Developments for Hydrogen Evolution Reaction in Alkaline Solutions - A Review. *Int. J. Hydrogen Energy* **2015**, *40* (1), 256–274. <https://doi.org/10.1016/j.ijhydene.2014.10.109>.
- [110] Zhao, G.; Rui, K.; Dou, S. X.; Sun, W. Heterostructures for Electrochemical Hydrogen Evolution Reaction: A Review. *Adv. Funct. Mater.* **2018**, *28* (43), 1–26. <https://doi.org/10.1002/adfm.201803291>.
- [111] Zhang, X.; Jin, G.; Wang, D.; Chen, Z.; Zhao, M.; Xi, G. Crystallographic Phase and Morphology Dependent Hydrothermal Synthesis of Tungsten Oxide for Robust Hydrogen Evolution Reaction. *J. Alloys Compd.* **2021**, *875*, 160054. <https://doi.org/10.1016/j.jallcom.2021.160054>.
- [112] Chen, J.; Yu, D.; Liao, W.; Zheng, M.; Xiao, L.; Zhu, H.; Zhang, M.; Du, M.; Yao, J. WO<sub>3-x</sub> Nanoplates Grown on Carbon Nanofibers for an Efficient Electrocatalytic Hydrogen Evolution Reaction. *ACS Appl. Mater. Interfaces* **2016**, *8* (28), 18132–18139. <https://doi.org/10.1021/acsami.6b05245>.
- [113] Ham, D. J.; Phuruangrat, A.; Thongtem, S.; Lee, J. S. Hydrothermal Synthesis of Monoclinic WO<sub>3</sub> Nanoplates and Nanorods Used as an Electrocatalyst for Hydrogen Evolution



- Reactions from Water. *Chem. Eng. J.* **2010**, *165* (1), 365–369. <https://doi.org/10.1016/j.cej.2010.09.003>.
- [114] Mohamed, M. M.; Salama, T. M.; Hegazy, M. A.; Abou Shahba, R. M.; Mohamed, S. H. Synthesis of Hexagonal WO<sub>3</sub> Nanocrystals with Various Morphologies and Their Enhanced Electrocatalytic Activities toward Hydrogen Evolution. *Int. J. Hydrogen Energy* **2019**, *44* (10), 4724–4736. <https://doi.org/10.1016/j.ijhydene.2018.12.218>.
- [115] Lv, Y.; Chen, Z.; Liu, Y.; Wang, T.; Ming, Z. Oxygen Vacancy Improves the Hydrogen Evolution Reaction Property of WO<sub>3-x</sub> Nanosheets. *Nano-Structures and Nano-Objects* **2018**, *15*, 114–118. <https://doi.org/10.1016/j.nanoso.2017.08.017>.
- [116] Rajalakshmi, R.; Rebekah, A.; Viswanathan, C.; Ponpandian, N. Evolution of Intrinsic 1-3D WO<sub>3</sub> Nanostructures: Tailoring Their Phase Structure and Morphology for Robust Hydrogen Evolution Reaction. *Chem. Eng. J.* **2022**, *428* (June 2021), 132013. <https://doi.org/10.1016/j.cej.2021.132013>.
- [117] Gong, F.; Yao, C.; Kong, H.; Meng, E.; Gong, L.; Zhang, Y.; Li, F. WO<sub>3</sub>/C Nanoarchitectures Assembled with 1D Nanowires: The Synthesis, Pt Nanoparticles Decoration, and Highly Enhanced Hydrogen Evolution in Neutral Media. *J. Phys. Chem. Solids* **2022**, *163* (November 2021), 110542. <https://doi.org/10.1016/j.jpics.2021.110542>.
- [118] Hu, G.; Li, J.; Liu, P.; Zhu, X.; Li, X.; Ali, R. N.; Xiang, B. Enhanced Electrocatalytic Activity of WO<sub>3</sub>@NPRGO Composite in a Hydrogen Evolution Reaction. *Appl. Surf. Sci.* **2019**, *463* (June 2018), 275–282. <https://doi.org/10.1016/j.apsusc.2018.08.227>.

- [119] Bharagav, U.; Reddy, N. R.; Koteswararao, V. N.; Ravi, P.; K., P.; Sathish, M.; Cheralathan, K. K.; Shankar, M. V.; Kumari, M. M. Heterojunction of CdS Nanocapsules-WO<sub>3</sub>Nanosheets Composite as a Stable and Efficient Photocatalyst for Hydrogen Evolution. *Energy and Fuels* **2020**, *34* (11), 14598–14610. <https://doi.org/10.1021/acs.energyfuels.0c00597>.
- [120] Bekarevich, R.; Pihosh, Y.; Tanaka, Y.; Nishikawa, K.; Matsushita, Y.; Hiroto, T.; Ohata, H.; Ohno, T.; Minegishi, T.; Sugiyama, M.; Kitamori, T.; Mitsuishi, K.; Takada, K. Conversion Reaction in the Binder-Free Anode for Fast-Charging Li-Ion Batteries Based on WO<sub>3</sub>Nanorods. *ACS Appl. Energy Mater.* **2020**, *3* (7), 6700–6708. <https://doi.org/10.1021/acsaem.0c00844>.
- [121] Pugliese, M.; Prontera, C. T.; Polimeno, L.; Lerario, G.; Giannuzzi, R.; Esposito, M.; Carallo, S.; Costa, D.; De Marco, L.; De Giorgi, M.; Gigli, G.; Sanvitto, D.; Maiorano, V. Highly Reflective Periodic Nanostructure Based on Thermal Evaporated Tungsten Oxide and Calcium Fluoride for Advanced Photonic Applications. *ACS Appl. Nano Mater.* **2020**, *3* (11), 10978–10985. <https://doi.org/10.1021/acsanm.0c02206>.
- [122] Chae, S. Y.; Lee, C. S.; Jung, H.; Joo, O. S.; Min, B. K.; Kim, J. H.; Hwang, Y. J. Insight into Charge Separation in WO<sub>3</sub>/BiVO<sub>4</sub> Heterojunction for Solar Water Splitting. *ACS Appl. Mater. Interfaces* **2017**, *9* (23), 19780–19790. <https://doi.org/10.1021/acsami.7b02486>.
- [123] Sharma, L.; Kumar, P.; Halder, A. Phase and Vacancy Modulation in Tungsten Oxide: Electrochemical Hydrogen Evolution. *ChemElectroChem* **2019**, *6* (13), 3420–3428. <https://doi.org/10.1002/celec.201900666>.
- [124] Ooka, H.; Huang, J.; Exner, K. S. The Sabatier Principle in Electrocatalysis: Basics, Limitations, and Extensions. *Front. Energy*

- Res.* **2021**, *9* (May), 1–20.  
<https://doi.org/10.3389/fenrg.2021.654460>.
- [125] Park, J.; Lee, S.; Kim, H. E.; Cho, A.; Kim, S.; Ye, Y.; Han, J. W.; Lee, H.; Jang, J. H.; Lee, J. Investigation of the Support Effect in Atomically Dispersed Pt on WO<sub>3-x</sub> for Utilization of Pt in the Hydrogen Evolution Reaction. *Angew. Chemie - Int. Ed.* **2019**, *58* (45), 16038–16042. <https://doi.org/10.1002/anie.201908122>.
- [126] Xie, C.; Chen, W.; Du, S.; Yan, D.; Zhang, Y.; Chen, J.; Liu, B.; Wang, S. In-Situ Phase Transition of WO<sub>3</sub> Boosting Electron and Hydrogen Transfer for Enhancing Hydrogen Evolution on Pt. *Nano Energy* **2020**, *71* (February), 104653. <https://doi.org/10.1016/j.nanoen.2020.104653>.
- [127] Lv, Y.; Liu, Y.; Liu, Y.; Chen, Z.; Zhang, M. CoSe<sub>2</sub>/WSe<sub>2</sub>/WO<sub>3</sub> Hybrid Nanowires on Carbon Cloth for Efficient Hydrogen Evolution Reaction. *J. Alloys Compd.* **2018**, *768*, 889–895. <https://doi.org/10.1016/j.jallcom.2018.07.285>.
- [128] Van Nguyen, T.; Do, H. H.; Tekalgne, M.; Van Le, Q.; Nguyen, T. P.; Hong, S. H.; Cho, J. H.; Van Dao, D.; Ahn, S. H.; Kim, S. Y. WS<sub>2</sub>-WC-WO<sub>3</sub> Nano-Hollow Spheres as an Efficient and Durable Catalyst for Hydrogen Evolution Reaction. *Nano Converg.* **2021**, *8* (1). <https://doi.org/10.1186/s40580-021-00278-3>.
- [129] Shang, X.; Rao, Y.; Lu, S. S.; Dong, B.; Zhang, L. M.; Liu, X. H.; Li, X.; Liu, Y. R.; Chai, Y. M.; Liu, C. G. Novel WS<sub>2</sub>/WO<sub>3</sub> Heterostructured Nanosheets as Efficient Electrocatalyst for Hydrogen Evolution Reaction. *Mater. Chem. Phys.* **2017**, *197*, 123–128. <https://doi.org/10.1016/j.matchemphys.2017.05.027>.
- [130] Lokhande, V.; Lokhande, A.; Namkoong, G.; Kim, J. H.; Ji, T. Charge Storage in WO<sub>3</sub> Polymorphs and Their Application as

- Supercapacitor Electrode Material. *Results Phys.* **2019**, *12* (December 2018), 2012–2020. <https://doi.org/10.1016/j.rinp.2019.02.012>.
- [131] Kang, M.; Liang, J.; Wang, F.; Chen, X.; Lu, Y.; Zhang, J. Structural Design of Hexagonal/Monoclinic WO<sub>3</sub> Phase Junction for Photocatalytic Degradation. *Mater. Res. Bull.* **2020**, *121* (May 2019), 110614. <https://doi.org/10.1016/j.materresbull.2019.110614>.
- [132] Lu, Y.; Liu, G.; Zhang, J.; Feng, Z.; Li, C.; Li, Z. Fabrication of a Monoclinic/Hexagonal Junction in WO<sub>3</sub> and Its Enhanced Photocatalytic Degradation of Rhodamine B. *Cuihua Xuebao/Chinese J. Catal.* **2016**, *37* (3), 349–358. [https://doi.org/10.1016/S1872-2067\(15\)61023-3](https://doi.org/10.1016/S1872-2067(15)61023-3).
- [133] Mineo, G.; Scuderi, M.; Bruno, E.; Mirabella, S. Engineering Hexagonal / Monoclinic WO<sub>3</sub> Phase Junctions for Improved Electrochemical Hydrogen Evolution Reaction. **2022**. <https://doi.org/10.1021/acsaem.2c01383>.
- [134] Du, Y.; Hao, Q.; Chen, D.; Chen, T.; Hao, S.; Yang, J.; Ding, H.; Yao, W.; Song, J. Facile Fabrication of Heterostructured Bismuth Titanate Nanocomposites: The Effects of Composition and Band Gap Structure on the Photocatalytic Activity Performance. *Catal. Today* **2017**, *297*, 255–263. <https://doi.org/10.1016/j.cattod.2016.12.048>.
- [135] Lo Nigro, R.; Malandrino, G.; Fragalà, I. L.; Bettinelli, M.; Speghini, A. MOCVD of CeF<sub>3</sub> Films on Si(100) Substrates: Synthesis, Characterization and Luminescence Spectroscopy. *J. Mater. Chem.* **2002**, *12* (9), 2816–2819. <https://doi.org/10.1039/b201716b>.
- [136] Yang, M.; Li, J.; Ke, G.; Liu, B.; Dong, F.; Yang, L.; He, H.; Zhou, Y. WO<sub>3</sub> Homo Junction Photoanode: Integrating the Advantages of WO<sub>3</sub> Different Facets for Efficient Water Oxidation.

- J. Energy Chem.* **2021**, *56*, 37–45.  
<https://doi.org/10.1016/j.jechem.2020.07.059>.
- [137] Tian, X.; Zhao, P.; Sheng, W. Hydrogen Evolution and Oxidation: Mechanistic Studies and Material Advances. *Adv. Mater.* **2019**, *31* (31). <https://doi.org/10.1002/adma.201808066>.
- [138] Diao, J.; Yuan, W.; Qiu, Y.; Cheng, L.; Guo, X. A Hierarchical Oxygen Vacancy-Rich WO<sub>3</sub> with “Nanowire-Array-on-Nanosheet-Array” Structure for Highly Efficient Oxygen Evolution Reaction. *J. Mater. Chem. A* **2019**, *7* (12), 6730–6739. <https://doi.org/10.1039/c9ta01044k>.
- [139] Ma, W.; Ma, R.; Wang, C.; Liang, J.; Liu, X.; Zhou, K.; Sasaki, T. A Superlattice of Alternately Stacked Ni-Fe Hydroxide Nanosheets and Graphene for Efficient Splitting of Water. *ACS Nano* **2015**, *9* (2), 1977–1984. <https://doi.org/10.1021/nn5069836>.
- [140] Song, F.; Hu, X. Ultrathin Cobalt – Manganese Layered Double Hydroxide Is An. *J. Am. Chem. Soc.* **2014**, 1–4.
- [141] Fan, K.; Chen, H.; Ji, Y.; Huang, H.; Claesson, P. M.; Daniel, Q.; Philippe, B.; Rensmo, H.; Li, F.; Luo, Y.; Sun, L. Nickel-Vanadium Monolayer Double Hydroxide for Efficient Electrochemical Water Oxidation. *Nat. Commun.* **2016**, *7* (June). <https://doi.org/10.1038/ncomms11981>.
- [142] Krstajić, N.; Popović, M.; Grgur, B.; Vojnović, M.; Šepa, D. On the Kinetics of the Hydrogen Evolution Reaction on Nickel in Alkaline Solution - Part I. The Mechanism. *J. Electroanal. Chem.* **2001**, *512* (1–2), 16–26. [https://doi.org/10.1016/S0022-0728\(01\)00590-3](https://doi.org/10.1016/S0022-0728(01)00590-3).

- [143] Anantharaj, S.; Karthik, P. E.; Noda, S. The Significance of Properly Reporting Turnover Frequency in Electrocatalysis Research. *Angew. Chemie - Int. Ed.* **2021**, *60* (43), 23051–23067. <https://doi.org/10.1002/anie.202110352>.
- [144] Costentin, C.; Passard, G.; Savéant, J. M. Benchmarking of Homogeneous Electrocatalysts: Overpotential, Turnover Frequency, Limiting Turnover Number. *J. Am. Chem. Soc.* **2015**, *137* (16), 5461–5467. <https://doi.org/10.1021/jacs.5b00914>.
- [145] Hu, W. H.; Han, G. Q.; Dong, B.; Liu, C. G. Facile Synthesis of Highly Dispersed WO<sub>3</sub>·H<sub>2</sub>O and WO<sub>3</sub> Nanoplates for Electrocatalytic Hydrogen Evolution. *J. Nanomater.* **2015**, *2015*. <https://doi.org/10.1155/2015/346086>.
- [146] Ma, J.; Ma, Z.; Liu, B.; Wang, S.; Ma, R.; Wang, C. Composition of Ag-WO<sub>3</sub> Core-Shell Nanostructures as Efficient Electrocatalysts for Hydrogen Evolution Reaction. *J. Solid State Chem.* **2019**, *271* (December 2018), 246–252. <https://doi.org/10.1016/j.jssc.2018.12.020>.
- [147] Chen, J.; Yu, D.; Liao, W.; Zheng, M.; Xiao, L.; Zhu, H.; Zhang, M.; Du, M.; Yao, J. WO<sub>3-x</sub> Nanoplates Grown on Carbon Nanofibers for an Efficient Electrocatalytic Hydrogen Evolution Reaction. *ACS Appl. Mater. Interfaces* **2016**, *8* (28), 18132–18139. <https://doi.org/10.1021/acsami.6b05245>.
- [148] Gelderman, K.; Lee, L.; Donne, S. W. Flat-Band Potential of a Semiconductor: Using the Mott-Schottky Equation. *J. Chem. Educ.* **2007**, *84* (4), 685–688. <https://doi.org/10.1021/ed084p685>.
- [149] Hankin, A.; Bedoya-Lora, F. E.; Alexander, J. C.; Regoutz, A.; Kelsall, G. H. Flat Band Potential Determination: Avoiding the Pitfalls. *J. Mater. Chem. A* **2019**, *7* (45), 26162–26176. <https://doi.org/10.1039/c9ta09569a>.

- [150] Bruno, L.; Strano, V.; Scuderi, M.; Franzò, G.; Priolo, F.; Mirabella, S. Localized Energy Band Bending in ZnO Nanorods Decorated with Au Nanoparticles. *Nanomaterials* **2021**, *11* (10). <https://doi.org/10.3390/nano11102718>.
- [151] Zhou, Z.; Wu, Z.; Xu, Q.; Zhao, G. A Solar-Charged Photoelectrochemical Wastewater Fuel Cell for Efficient and Sustainable Hydrogen Production. *J. Mater. Chem. A* **2017**, *5* (48), 25450–25459. <https://doi.org/10.1039/c7ta08112j>.
- [152] Raza, W.; Ali, F.; Raza, N.; Luo, Y.; Kim, K. H.; Yang, J.; Kumar, S.; Mehmood, A.; Kwon, E. E. Recent Advancements in Supercapacitor Technology. *Nano Energy* **2018**, *52* (June), 441–473. <https://doi.org/10.1016/j.nanoen.2018.08.013>.
- [153] Xie, J.; Yang, P.; Wang, Y.; Qi, T.; Lei, Y.; Li, C. M. Puzzles and Confusions in Supercapacitor and Battery: Theory and Solutions. *J. Power Sources* **2018**, *401* (September), 213–223. <https://doi.org/10.1016/j.jpowsour.2018.08.090>.
- [154] Jiang, Y.; Liu, J. Definitions of Pseudocapacitive Materials: A Brief Review. *Energy Environ. Mater.* **2019**, *2* (1), 30–37. <https://doi.org/10.1002/eem2.12028>.
- [155] Xiao, J.; Wan, L.; Yang, S.; Xiao, F.; Wang, S. Design Hierarchical Electrodes with Highly Conductive NiCo 2S4 Nanotube Arrays Grown on Carbon Fiber Paper for High-Performance Pseudocapacitors. *Nano Lett.* **2014**, *14* (2), 831–838. <https://doi.org/10.1021/nl404199v>.
- [156] González, A.; Goikolea, E.; Barrena, J. A.; Mysyk, R. Review on Supercapacitors: Technologies and Materials. *Renew. Sustain.*

- Energy Rev.* **2016**, *58*, 1189–1206.  
<https://doi.org/10.1016/j.rser.2015.12.249>.
- [157] Muller, G. A.; Cook, J. B.; Kim, H. S.; Tolbert, S. H.; Dunn, B. High Performance Pseudocapacitor Based on 2D Layered Metal Chalcogenide Nanocrystals. *Nano Lett.* **2015**, *15* (3), 1911–1917.  
<https://doi.org/10.1021/nl504764m>.
- [158] Wang, J.; Polleux, J.; Lim, J.; Dunn, B. Pseudocapacitive Contributions to Electrochemical Energy Storage in TiO<sub>2</sub> (Anatase) Nanoparticles. *J. Phys. Chem. C* **2007**, *111* (40), 14925–14931.  
<https://doi.org/10.1021/jp074464w>.
- [159] Tian, J.; Lin, B.; Sun, Y.; Zhang, X.; Yang, H. Porous WO<sub>3</sub>@CuO Composites Derived from Polyoxometalates@metal Organic Frameworks for Supercapacitor. *Mater. Lett.* **2017**, *206*, 91–94. <https://doi.org/10.1016/j.matlet.2017.06.116>.
- [160] Jia, J.; Liu, X. D.; Li, X.; Cao, L.; Zhang, M.; Wu, B.; Zhou, X. Effect of Residual Ions of Hydrothermal Precursors on the Thickness and Capacitive Properties of WO<sub>3</sub> Nanoplates. *J. Alloys Compd.* **2020**, *823*, 153715.  
<https://doi.org/10.1016/j.jallcom.2020.153715>.
- [161] Huang, Y.; Li, Y.; Zhang, G.; Liu, W.; Li, D.; Chen, R.; Zheng, F.; Ni, H. Simple Synthesis of 1D, 2D and 3D WO<sub>3</sub> Nanostructures on Stainless Steel Substrate for High-Performance Supercapacitors. *J. Alloys Compd.* **2019**, *778*, 603–611.  
<https://doi.org/10.1016/j.jallcom.2018.11.212>.
- [162] Shinde, P. A.; Lokhande, A. C.; Patil, A. M.; Lokhande, C. D. Facile Synthesis of Self-Assembled WO<sub>3</sub> Nanorods for High-Performance Electrochemical Capacitor. *J. Alloys Compd.* **2019**, *770*, 1130–1137. <https://doi.org/10.1016/j.jallcom.2018.08.194>.



- [163] Chang, K. H.; Hu, C. C.; Huang, C. M.; Liu, Y. L.; Chang, C. I. Microwave-Assisted Hydrothermal Synthesis of Crystalline WO<sub>3</sub>·0.5H<sub>2</sub>O Mixtures for Pseudocapacitors of the Asymmetric Type. *J. Power Sources* **2011**, *196* (4), 2387–2392. <https://doi.org/10.1016/j.jpowsour.2010.09.078>.
- [164] Ji, S. H.; Chodankar, N. R.; Kim, D. H. Aqueous Asymmetric Supercapacitor Based on RuO<sub>2</sub>-WO<sub>3</sub> Electrodes. *Electrochim. Acta* **2019**, *325*, 134879. <https://doi.org/10.1016/j.electacta.2019.134879>.
- [165] Nayak, A. K.; Das, A. K.; Pradhan, D. High Performance Solid-State Asymmetric Supercapacitor Using Green Synthesized Graphene-WO<sub>3</sub> Nanowires Nanocomposite. *ACS Sustain. Chem. Eng.* **2017**, *5* (11), 10128–10138. <https://doi.org/10.1021/acssuschemeng.7b02135>.
- [166] Zhang, S.; Pan, N. Supercapacitors Performance Evaluation. *Adv. Energy Mater.* **2015**, *5* (6), 1–19. <https://doi.org/10.1002/aenm.201401401>.
- [167] Shi, F.; Li, J.; Xiao, J.; Zhao, X.; Li, H.; An, Q.; Zhai, S.; Wang, K.; Wei, L.; Tong, Y. Three-Dimensional Hierarchical Porous Lignin-Derived Carbon/WO<sub>3</sub> for High-Performance Solid-State Planar Micro-Supercapacitor. *Int. J. Biol. Macromol.* **2021**, *190* (August), 11–18. <https://doi.org/10.1016/j.ijbiomac.2021.08.183>.
- [168] Giannuzzi, R.; Scarfiello, R.; Sibillano, T.; Nobile, C.; Grillo, V.; Giannini, C.; Cozzoli, P. D.; Manca, M. From Capacitance-Controlled to Diffusion-Controlled Electrochromism in One-Dimensional Shape-Tailored Tungsten Oxide Nanocrystals. *Nano Energy* **2017**, *41* (July), 634–645. <https://doi.org/10.1016/j.nanoen.2017.09.058>.

- [169] Yu, A., Chabot, V., & Zhang, J. Electrochemical supercapacitors for energy storage and delivery: fundamentals and applications (p. 383). Taylor & Francis. (2013)
- [170] Lollman, D. B. B.; Lemire, C.; Al Mohammad, A.; Gillet, E.; Aguir, K. Reactive R.F. Magnetron Sputtering Deposition of WO<sub>3</sub> Thin Films. *Sensors Actuators, B Chem.* **2002**, *84* (1), 49–54. [https://doi.org/10.1016/S0925-4005\(01\)01073-5](https://doi.org/10.1016/S0925-4005(01)01073-5).
- [171] Hong, K., Xie, M.; Wu, H. Tungsten oxide nanowires synthesized by a catalyst-free method at low temperature. *Nanotechnol.* 2006, *17(19)*, 4830. <https://doi.org/10.1088/0957-4484/17/19/008>
- [172] Djaoued, Y.; Priya, S.; Balaji, S. Low temperature synthesis of nanocrystalline WO<sub>3</sub> films by sol–gel process. *J Non Cryst Solids* 2008, *354(2-9)*, 673-679. <https://doi.org/10.1016/j.jnoncrysol.2007.07.090>
- [173] Deepa, M.; Kar, M.; Agnihotry, S. A.; Electrodeposited tungsten oxide films: annealing effects on structure and electrochromic performance; *Thin solid films* 2004, *468(1-2)*, 32-42. <https://doi.org/10.1016/j.tsf.2004.04.056>
- [174] Kalhori, H.; Ranjbar, M.; Salamati, H.; Coey, J. M. D. Flower-like nanostructures of WO<sub>3</sub>: fabrication and characterization of their in-liquid gasochromic effect; *Sens. Actuators B Chem.* 2016, *225*, 535-543. <https://doi.org/10.1016/j.snb.2015.11.044>
- [175] Poongodi, S.; Kumar, P. S.; Mangalaraj, D.; Ponpandian, N.; Meena, P.; Masuda, Y.; Lee, C. Electrodeposition of WO<sub>3</sub> nanostructured thin films for electrochromic and H<sub>2</sub>S gas sensor applications; *J. Alloys Compd.* 2017, *719*, 71-81. <https://doi.org/10.1016/j.jallcom.2017.05.122>

- [176] Deepa, M.; Srivastava, A. K.; Sood, K. N.; Agnihotry, S. A. Nanostructured mesoporous tungsten oxide films with fast kinetics for electrochromic smart windows; *Nanotechnol* 2006, *17*(10), 2625. <https://doi.org/10.1088/0957-4484/17/10/030>
- [177] More, A. J.; Patil, R. S.; Dalavi, D. S.; Mali, S. S.; Hong, C. K.; Gang, M. G.; Patil, P. S. Electrodeposition of nano-granular tungsten oxide thin films for smart window application; *Mater. Lett.* 2014, *134*, 298-301. <https://doi.org/10.1016/j.matlet.2014.07.059>
- [178] Baeck, S. H.; Jaramillo, T.; Stucky, G. D.; McFarland, E. W. Controlled electrodeposition of nanoparticulate tungsten oxide; *Nano Lett.* 2002, *2*(8), 831-834. <https://doi.org/10.1021/nl025587p>
- [179] Vijayakumar, E.; Yun, Y. H.; Quy, V. H. V.; Lee, Y. H.; Kang, S. H.; Ahn, K. S.; Lee, S. W. Development of Tungsten Trioxide Using Pulse and Continuous Electrodeposition and Its Properties in Electrochromic Devices; *J. Electrochem. Soc.* 2019, *166*(4), D86. <https://doi.org/10.1149/2.0271904jes>
- [180] Kim, Y. O.; Yu, S. H.; Ahn, K. S.; Lee, S. K.; Kang, S. H. Enhancing the photoresponse of electrodeposited WO<sub>3</sub> film: structure and thickness effect. *J. Electroanal. Chem.* 2005, *752*, 25-32. <https://doi.org/10.1016/j.jelechem.2015.05.031>
- [181] Leftheriotis, G.; Yianoulis, P. Development of electrodeposited WO<sub>3</sub> films with modified surface morphology and improved electrochromic properties; *Solid State Ionics* 2008, *179*(38), 2192-2197. <https://doi.org/10.1016/j.ssi.2008.07.018>
- [182] Srivastava, A. K.; Deepa, M.; Singh, S.; Kishore, R.; Agnihotry, S. A. Microstructural and electrochromic characteristics of electrodeposited and annealed WO<sub>3</sub> films; *Solid State Ionics* 2005, *176*(11-12), 1161-1168. <https://doi.org/10.1016/j.ssi.2004.10.006>

- [183] Scharifker, B.; Hills, G. Theoretical and experimental studies of multiple nucleation; *Electrochim. Acta* 1983, 28(7), 879-889. [https://doi.org/10.1016/0013-4686\(83\)85163-9](https://doi.org/10.1016/0013-4686(83)85163-9)
- [184] Genplot, Available online, <http://www.genplot.com/download.htm>
- [185] Kwong, W. L.; Savvides, N.; Sorrel, C. C. Electrodeposited nanostructured WO<sub>3</sub> thin films for photoelectrochemical applications; *Electrochim. Acta* 2012, 75, 371-380
- [186] Meulenkamp, E. A. Mechanism of WO<sub>3</sub> Electrodeposition from Peroxy-Tungstate Solution; *J. Electrochem. Soc.* **1997**, 144(5), 1664. <https://doi.org/10.1149/1.1837657>
- [187] Silambarasan, D.; Surya, V. J.; Vasu, V.; Iyakutti, K. Single Walled Carbon Nanotube-Metal Oxide Nanocomposites for Reversible and Reproducible Storage of Hydrogen. *ACS Appl. Mater. Interfaces* **2013**, 5 (21), 11419–11426. <https://doi.org/10.1021/am403662t>.
- [188] Cheng, H. M.; Yang, Q. H.; Liu, C. Hydrogen Storage in Carbon Nanotubes. *Carbon N. Y.* **2001**, 39 (10), 1447–1454. [https://doi.org/10.1016/S0008-6223\(00\)00306-7](https://doi.org/10.1016/S0008-6223(00)00306-7).
- [189] Duku, M. H.; Gu, S.; Hagan, E. Ben. Biochar Production Potential in Ghana - A Review. *Renew. Sustain. Energy Rev.* **2011**, 15 (8), 3539–3551. <https://doi.org/10.1016/j.rser.2011.05.010>.
- [190] Mazzoldi, P., Nigro, M., & Voci, C. (2006). *Elementi di fisica*. SES.



---

## List of Publications

This thesis is based on the following publications:

- **Mineo, G.**, Moulace, K., Neri, G., Mirabella, S., & Bruno, E. (2021). H<sub>2</sub> detection mechanism in chemoresistive sensor based on low-cost synthesized WO<sub>3</sub> nanorods. *Sensors and Actuators B: Chemical*, 348, 130704.
- **Mineo, G.**, Moulace, K., Neri, G., Mirabella, S., & Bruno, E. (2022). Mechanism of NO fast response in WO<sub>3</sub> nanorods based gas sensor. Submitted to Chemosensor.
- **Mineo, G.**, Scuderi, M., Bruno, E., & Mirabella, S. (2022). Engineering Hexagonal/Monoclinic WO<sub>3</sub> Phase Junctions for Improved Electrochemical Hydrogen Evolution Reaction. *ACS Applied Energy Materials*.
- **Mineo, G.**; Scuderi M.; Pezzotti Escobar G.; Mirabella, S.; Bruno, E. Engineering of nanostructured WO<sub>3</sub> powders for asymmetric supercapacitors, Submitted to Nanomaterials, 2022
- **Mineo, G.**, Ruffino, F., Mirabella, S., & Bruno, E. (2020). Investigation of WO<sub>3</sub> electrodeposition leading to nanostructured thin films. *Nanomaterials*, 10(8), 1493.

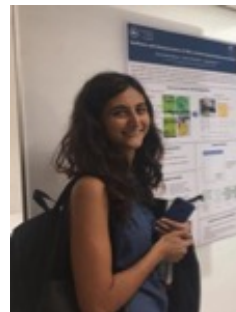
Other Publication:

- Di Mari, G. M., **Mineo, G.**, Franzò, G., Mirabella, S., Bruno, E., & Strano, V. (2022). Low-Cost, High-Yield ZnO Nanostars Synthesis for Pseudocapacitor Applications. *Nanomaterials*, 12(15), 2588.

---

## Curriculum Vitae

Giacometta Mineo was born on 18<sup>th</sup> of March 1994 in Bronte (CT), Italy. She attained her master's degree in Physics with marks 110/110 cum Laude from the University of Catania on 22 October 2019, with a dissertation entitled "*Synthesis and characterization of nanostructured tungsten oxide film*". In November 2019 she started the Ph.D. course in Science of Materials and Nanotechnology at University of Catania. She is currently working under the



supervision of Prof. Elena Bruno and Prof. Salvo Mirabella at the Physics and Astronomy Department of the University of Catania. The main scientific interests are focused on the synthesis of WO<sub>3</sub> nanostructure for H<sub>2</sub> sensing, production, and storage applications. During her Ph.D. course she has been involved in several collaboration with CNR-IMM, Department of Electronic Engineering, Chemistry and Industrial Engineering of University of Messina, Department of Chemistry of Pavia. She presented the results of her research activity giving both oral and poster contributions at the following international conferences: 2019 FISMAT (Catania), 2020 E-MRS fall meeting (online), 2021 E-MRS spring meeting (online), 2021 E-MRS fall meeting (online), 2022 E-MRS spring meeting (online), 2022 E-MRS fall meeting (Warsaw). She was part of the organizing committee of NanoSoli 2022 school (Catania). Giacometta Mineo is author or co-author of several articles, published in international referred scientific journals.

---

## Oral presentation

- **E-MRS spring meeting 2022**  
May 30<sup>th</sup> -June 3<sup>rd</sup>, 2022, online meeting  
Title: *One-step hydrothermal synthesis of WO<sub>3</sub> nanostructures and optimization for energy storage application*  
Presenting Author
- **E-MRS spring meeting 2022**  
May 30<sup>th</sup> -June 3<sup>rd</sup>, 2022, online meeting  
Title: *Influence of annealing process of WO<sub>3</sub> based nanorods for Hydrogen Evolution Reaction*  
Presenting Author
- **E-MRS spring meeting 2022**  
May 30<sup>th</sup> -June 3<sup>rd</sup>, 2022, online meeting  
Title: *Study of the H<sub>2</sub> detection mechanism in chemoresistive sensors using low-cost WO<sub>3</sub> nanorods*  
Presenting Author
- **E-MRS fall meeting 2021**  
September 20<sup>th</sup>-23<sup>rd</sup>, 2021, online meeting  
Title: *One-step hydrothermal synthesis of WO<sub>3</sub> nanorods for hydrogen storage application*  
Presenting Author
- **E-MRS fall meeting 2021**  
September 20<sup>th</sup>-23<sup>rd</sup>, 2021, online meeting  
Title: *Study of the H<sub>2</sub> detection mechanism in chemoresistive sensors using low-cost WO<sub>3</sub> nanorods*  
Presenting Author



- 
- **E-MRS spring meeting 2021**  
May 31<sup>st</sup> -June 4<sup>th</sup>, 2022, online meeting  
Title: *Defect-mediated H<sub>2</sub> sensing mechanism by hydrothermally grown hexagonal WO<sub>3</sub> nanorods*  
Presenting Author

### Poster presentation

- **E-MRS spring meeting 2021**  
May 31<sup>st</sup> -June 4<sup>th</sup>, 2022, online meeting  
Title: *Simple one-step hydrothermal synthesis of WO<sub>3</sub> nanorods for energy storage application*  
Presenting Author
- **FisMat 2019**  
September 30<sup>th</sup>-October 4<sup>th</sup>, 2019, Catania (Italy)  
Title: *Synthesis and characterization of WO<sub>x</sub> nanostructures by low-cost method*  
Presenting Author

### School

- **Nanostructured Solid Liquid Interface School “NanoSoLI 2022”**  
July 11<sup>th</sup>–15<sup>th</sup> 2022, Catania
- **IAEA Training Workshop on Ion Beam Driven Materials Engineering: New Roles for Accelerators for Quantum Technologies**  
May 4<sup>th</sup>–7<sup>th</sup> 2021, online school
- **Aldo Armigliato “SEM School 2020”**  
March 23<sup>rd</sup>-27<sup>th</sup> 2020, online school



## Ringraziamenti

Le parole della scrittrice J. K. Rowling che aprono questa tesi di Dottorato, sono state per me un monito, durante questi anni di studio. Così come Harry sceglie di appartenere ai Grifondoro, piuttosto che ai Serpeverde nonostante le sue abilità, ogni Ricercatore dovrebbe scegliere di lavorare per il bene comune, mettendo a disposizione le proprie competenze e facendo parte di una squadra il cui unico interesse è migliorare la vita umana nel rispetto del pianeta in cui ci troviamo.

Ringrazio i miei tutor, la Prof.ssa Elena Bruno e il Prof. Salvo Mirabella, i quali mi hanno aiutato anche nei momenti più difficili, facendomi credere in me stessa e nelle mie capacità. La loro grande professionalità e il loro grande entusiasmo sono stati per me fonte di ispirazione nell'intraprendere questo bellissimo viaggio che è il percorso di Dottorato, alimentando la passione in comune per i fenomeni fisici e chimici che descrivono il nostro mondo. Loro sono stati per me un modello da seguire sia dal punto di vista scientifico che dal punto di vista umano, condividendo con me la voglia di superare i piccoli fallimenti e la gioia per ogni piccola scoperta.

Ringrazio il Prof. Giovanni Neri e la Prof.ssa Chiara Milanese per aver condiviso con me le loro conoscenze e avermi dato la possibilità di utilizzare i loro laboratori.

Ringrazio il coordinatore del corso di Dottorato in Scienze dei Materiali e Nanotecnologie Prof. Giuseppe Compagnini, la sig.ra Tosto e tutto il personale amministrativo per la grande disponibilità e gentilezza.

Ringrazio il Prof. Terrasi, la Prof.ssa Grimaldi, il Prof. Reitano e il Prof. Ruffino per la loro grande professionalità e disponibilità.

Ringrazio tutti i ricercatori del gruppo CNR-IMM e il personale tecnico e amministrativo tra cui la Dott.ssa Maria Cantarella e Giuseppe Pantè, con cui ho avuto modo di interagire durante il mio percorso di Dottorato, mostrandomi sempre una grande disponibilità al confronto.

Ringrazio il Prof. Simonpietro Agnello e il Prof. Luigi Falciola che in qualità di referee hanno letto la mia tesi fornendomi preziosi suggerimenti.

Ringrazio i ricercatori che lavorano al Dipartimento di Fisica, tra cui Maria Josè, Antonio, Sergio, Nino e Stefano per aver messo sempre a disposizione le loro conoscenze e per avermi aiutato durante questi anni.

Ringrazio la Dott.ssa Vicky Strano, che avrei voluto conoscere molto tempo prima. La sua esperienza e le sue capacità mi hanno aiutato molto nei momenti più difficili di questo percorso.

Ringrazio le mie colleghe di studi Noemi, Marika, Cristina e Melissa con le quali ho condiviso e condivido ancora la passione per la Fisica sin dal primo anno della triennale, e tutti i colleghi conosciuti in questi anni, tra cui Fiorella Tringali, Andrea Lo Mastro, Salvo La Manna e Federico Ursino.

Un sincero grazie va ai colleghi che ho conosciuto grazie al Dottorato e che si sono trasformati in cari amici: Melanie, Luca, Gisella e Valentina, con i quali ho passato molto tempo nella “Stanza DottorandE”, condividendo molte lunghe giornate, accompagnate qualche volta da attimi di sconforto, ma sempre concluse con serenità e con il sorriso.

Un profondo ringraziamento va ai miei genitori Nunzio e Rita per avermi insegnato il valore del sacrificio e della perseveranza, fondamentali in questo percorso, e ai miei fratelli Nina, Salvatore e Anna, per essermi stati accanto e per essere pronti a giocare con me anche adesso che siamo grandi. Ringrazio i miei suoceri Pippo e Alfina, tutti i miei cognati Riccardo, Melania, Alessandra, Antonio (il grande) e Antonio (il piccolo), Irene e il mio nipotino Stefano per essere stati sempre presenti.

Infine, il ringraziamento più grande va a Francesco, che più di ogni altro mi conosce e mi apprezza senza mai farmi sentire in difetto. A lui va tutto il mio amore e la mia gratitudine per la vita passata insieme e per quella che verrà.

